
Electronic Thesis and Dissertation Repository

7-24-2018 2:00 PM

Impact Melt Emplacement on Mercury

Jeffrey Daniels, *The University of Western Ontario*

Supervisor: Neish, Catherine D., *The University of Western Ontario*

A thesis submitted in partial fulfillment of the requirements for the Master of Science degree in
Geology

© Jeffrey Daniels 2018

Follow this and additional works at: <https://ir.lib.uwo.ca/etd>



Part of the [Geology Commons](#), [Physical Processes Commons](#), and the [The Sun and the Solar System Commons](#)

Recommended Citation

Daniels, Jeffrey, "Impact Melt Emplacement on Mercury" (2018). *Electronic Thesis and Dissertation Repository*. 5657.

<https://ir.lib.uwo.ca/etd/5657>

This Dissertation/Thesis is brought to you for free and open access by Scholarship@Western. It has been accepted for inclusion in Electronic Thesis and Dissertation Repository by an authorized administrator of Scholarship@Western. For more information, please contact wlsadmin@uwo.ca.

Abstract

Impact cratering is an abrupt, spectacular process that occurs on any world with a solid surface. On Earth, these craters are easily eroded or destroyed through endogenic processes. The Moon and Mercury, however, lack a significant atmosphere, meaning craters on these worlds remain intact longer, geologically. In this thesis, remote-sensing techniques were used to investigate impact melt emplacement about Mercury's fresh, complex craters. For complex lunar craters, impact melt is preferentially ejected from the lowest rim elevation, implying topographic control. On Venus, impact melt is preferentially ejected downrange from the impact site, implying impactor-direction control. Mercury, despite its heavily-cratered surface, trends more like Venus than like the Moon. However, these results suggest gravity, as well as impactor velocity, is ultimately responsible. Future work should study other rocky bodies in the Solar System, including Mars and Ceres, to better understand impact-melt emplacement on terrestrial planets.

Keywords

Impact cratering, Mercury, MESSENGER, terrestrial planets.

Acknowledgements

First and foremost, I would like graciously to thank Dr. Catherine Neish for her incredible, generous, and at times crucial, aid and guidance as thesis supervisor – and for taking me on as a Masters candidate to begin with. Equally importantly, I am deeply grateful to my mother and father for successfully moving me to London, Ontario in order to undertake my Masters work here at Western University, and all the trials and tribulations that had entailed, being readily available to interact with thereby helping stave off home-sickness on occasion, and overall surviving alongside me through the thick and thin of this two-year scholarly experience.

Other acknowledgements include Mallory Kinczyk, from North Carolina State University, who directed me to work by Carolyn Ernst regarding Hokusai crater which was of importance to this work, Kris Becker, from LPL in Arizona, for providing the RMS error values of the USGS DEM that was vital to this work, Livio Tornabene, Adjunct Professor at Western University, for his extensive knowledge on data management, and Michael Zanetti, Postdoctoral Fellow at Western University, who also provided me with good advice concerning thesis writing and papers to read pertinent to my thesis work.

Finally, a thank you to Margi Kobal for effectively ensuring my stay at Bayfield Hall these past two years has been as hassle-free as possible and even doing so well prior to my moving down to London.

Table of Contents

Abstract	i
Acknowledgements	ii
Table of Contents	iii
List of Tables	v
List of Figures	vi
List of Appendices	x
Chapter 1	1
1 Introduction	1
1.1 The Impact Cratering Process	3
1.2 Impact Melt Generation and Emplacement	6
1.3 Mercury	9
1.4 Impact Melt Emplacement about Mercurian Craters	13
Chapter 2	17
2 Methodology	17
2.1 Data Acquisition	18
2.2 Data Manipulation	19
2.3 Data Analysis	23
Chapter 3	30
3 Results	30
3.1 The Final Crater Catalog	30
3.2 Numerical Calculations and Modeling	35

3.3 Comparison of Results to Prior Work	37
Chapter 4	45
4 Discussion	45
4.1 Where Does Mercury Fit?	45
4.2 Limitations Due to MESSENGER Data	50
4.3 Implications for Other Rocky Bodies in the Solar System	51
Chapter 5	56
5 Conclusions	56
References	60
Curriculum Vitae	97

List of Tables

Table 1: The twenty-four Mercurian craters, and the pertinent data about each crater used in this study	39
Table 2: Latitude and Longitude values used to crop out each crater in this study, plus errors associated with the data	40
Table 3: A qualitative comparison of rim-low vs melt-deposit directions for the lowest (RCL) and second-lowest rim elevations for each crater (see Figure 19 below), as well as other remarks specific to these craters	41

List of Figures

Figure 1: The primary stages of crater formation, based on Osinski et al. (2011), with simple craters on the left and complex craters on the right	5
Figure 2: Left = MDIS-NAC image (CN0213154766M) of Ailey Crater showing exterior melt pond in an adjacent, older crater; contrast enhanced to help bring out melt pond more clearly. Right = same image, with melt pond marked out in purple.....	7
Figure 3: MDIS-NAC image (CN0229495136M) of Waters crater in Mercury’s southern hemisphere, with predominant melt flow highlighted by red line	8
Figure 4: LROC-NAC mosaic of lunar crater Jackson, viewed using the Quickmap program provided by Arizona State University; inset shows an example of melt veneer (slightly darker material overlaying surrounding rocks, highlighted by red lines) on part of the central uplift (see Osinski et al., 2011). While there should also be veneers on Mercurian craters, most of the MDIS-NAC imagery is generally too low in resolution to properly identify such veneers	8
Figure 5: MESSENGER’s orbit about Mercury during its main mission conducted from 2009 through 2011 (see Solomon et al., 2001). The spacecraft’s orbit was very elliptical, with its closest approach occurring over Mercury’s northern hemisphere	10
Figure 6: The melt direction of fresh, complex craters on the Moon and Venus, compared to the direction of the crater’s RCL as determined from Neish et al. (2017). The melt and RCL are either “coinciding” (RCL and melts lie in the same direction from the crater’s center), “within 45°” (melts are within 45° from the RCL), “within 90°” (melts lie between 45° and 90° from the RCL), or “90 or greater” (melts lie on the other side of the crater from the RCL). Over half of lunar complex craters lie within the “coincide” regime, whereas on Venus the distribution is fairly even across all four regimes	15
Figure 7: Illustration of the hypothesis proposed by Neish et al. (2017). They theorize that the greater melt production combined with comparatively shallower crater depths on Venus mean the melt that is ejected is not constrained by the crater topography, but instead likely by impactor direction. In contrast, crater formation on the Moon produces	

comparatively deeper craters as well as notably lesser melt material. As such, the ejection of melt is constrained by this greater average topography and usually only has enough energy to leave the crater, if it does, out its RCL.....16

Figure 8: MDIS mosaic image of Abedin crater, rendered in QGIS with a sinusoidal projection centered on the crater. Re-projecting the image removes the distortions evident in the equirectangular projection.....21

Figure 9: Abedin crater with USGS DEM overlaying the MDIS global mosaic image, and the melts and rim shapefiles over top them. The rim, in blue, was drawn using a line shapefile, while the crater floor, in green, and the ejected melt, in purple, were drawn using polygon shapefiles22

Figure 10: The crater-size determination process, as conducted using the “Measure” tool in QGIS. A traverse from W to E and a traverse from S to N (red lines) are then averaged to give an average diameter value that is used for later calculations23

Figure 11: Abedin crater, with a sixteen-wedge grid overlain on the image. The RCL (red) and melt (purple) directions are highlighted on the grid. The smaller of the two main melt ponds are highlighted in a more transparent purple, while the larger one (used for further analysis) is marked by solid purple25

Figure 12: Topographic profile of Abedin’s crater rim, with the highest rim elevation (RCH) and lowest rim elevation (RCL) marked in blue. Figure 15 relates this rim profile to the crater’s image file.....27

Figure 13: Rayed crater Xiao Zhao (Eminescu crater to the west), exemplifying an asymmetric ray pattern. The forbidden zone for Xiao Zhao is roughly NE of the crater, implying a direction of impact towards the SW (red arrow). Image cropped from the MDIS Low Incidence-Angle mosaic28

Figure 14: Low Incidence-Angle MDIS mosaic image of rayed crater Balanchine, with forbidden zone highlighted on the sixteen-wedge grid in blue and impactor direction marked in solid blue in the middle of the forbidden zone. The impact-melt direction for Balanchine is also marked on the grid, in purple29

Figure 15: Abedin crater. MDIS mosaic with USGS DEM overlay, processed in QGIS. Rim shown in blue, crater floor in green, melts in violet, and contour lines (black) have a 300 m interval. A topographic profile of Abedin’s rim reveals the RCL (highlighted by blue circle) to be north of the crater, towards a nearby crater32

Figure 16: Hokusai crater. MDIS mosaic with USGS DEM overlay, processed in QGIS. Rim shown in blue, crater floor in green, melts in violet, and contour lines (black) have a 300 m interval. A topographic profile of Hokusai’s rim reveals the RCL (highlighted by blue circle) resides to the NE of the crater. Note also the rampart feature characteristic of this crater, enhanced by the highlighted contour lines. As with the melts, these ramparts appear to cluster more on the south and west sides of the crater33

Figure 17: Melt location with respect to RCL location for Mercurian, Venusian, and lunar complex craters. Lunar craters show a notable spike in values at and near the “coincide” regime, that is not present as such on Venus and Mercury. For Venus, there is a slight trend towards the “90 or greater” regime but otherwise is fairly even across the regimes. Qualitatively, Mercury’s craters seem to follow a trend that is more similar to the Venusian trend than the lunar trend. Data for the Moon and Venus from Neish et al. (2017).....42

Figure 18: Comparison of the ratio R for Mercury, the Moon, and Venus shows that Mercury’s craters follow the Venusian trend more closely than the lunar trend. Lunar and Venusian crater data from Neish et al. (2017)43

Figure 19: Rim-low vs melt-location for complex craters of the planet Mercury, comparing RCL vs melt location and the second-lowest rim elevation vs melt location for the catalog of 24 craters studied in this work. Note that the “second-lowest” plot trends as an inversion to the normal lunar trend seen in Neish et al. (2017)44

Figure 20: The two emplacement paradigms suggested by Neish et al. (2017) are sorted according to the results found in this study. Here, the paradigm found on Venus is the high impactor-velocity/surface-gravity end-member while the one found on the Moon is the low impactor-velocity/surface-gravity end-member. Mercury also falls within the high impactor-velocity/surface-gravity paradigm. These paradigms may be part of one,

transitional paradigm, but more rocky worlds with differing surface gravity and impactor velocity values will be needed to test this hypothesis.....49

Figure 21: Top = image of CTX overlay (Stamp B12_014262_1513_XN_28S113W) of Zumba crater on Mars, rendered in JMARS, with its more obvious exterior melt deposit highlighted by the red rectangle (see Tornabene et al., 2012). Bottom = inset shown in red rectangle, also rendered in JMARS, where the CTX image is overlain by a HiRISE image (Stamp ESP_017229_1510_RED); melt ponds highlighted by red arrows53

Figure 22: Ikapati crater (HAMO image FC21A0042388_15249065450F1F; from 2015248_C2_ORBIT068, 20150829_CYCLE2, DWNCHFC2_1A, Dawn Ceres FC2 raw HAMO, sbn.psi.edu/pds/resource/dawn/dwncfcL1.html), on the dwarf planet Ceres. The ejected melt (marked by red arrows) appears to have been emplaced within an adjacent, older-looking crater.....54

Figure 23: One of the exterior melt ponds (red arrows) about Marcia crater (located at bottom of image) on Vesta. Image from abnarchive.psi.edu/pds3/dawn/fc/ (image FC21A0010229_11287083759F1U, from 2011287_C3_ORBIT07, 2011284_CYCLE3, 2011272_HAMO, DWNVFC2_1A).....55

List of Appendices

Appendix A: Individual crater files created for Impact Melt-Bearing Mercurian Complex Craters Catalog.....	71
Appendix B: EDRNAC images used in individual crater files	95

Chapter 1

1 Introduction

Impact cratering is a geologic process resulting from the impact of a projectile from elsewhere striking the surface of a planetary body at high speeds. Impact cratering is one of a select few geologic processes that occur on nearly every celestial body in the Solar System. The high speeds and subsequent energies involved mean impact cratering holds a very rare place among known geologic processes in being initiated and then completed within seconds to minutes. Impact cratering involves several steps of formation, and has a number of notable features associated with it including ejecta material and impact-generated melt.

The presence of impact craters on a planet's surface can be helpful in remotely probing what lies beneath the uppermost layer of the surface of many worlds in the Solar System (see Melosh, 1989 and Osinski and Pierazzo, 2013). Fresh craters provide outcrop-level exposures of the geologic units that lie below the surface, which in turn provides a productive means by which space probes can view the shallow subsurface of other worlds (Osinski and Pierazzo, 2013). The density of impact craters on a planet's surface, as well as the state of decay of these craters, can give insight into the geologic history of the target world: a more heavily-cratered surface implies a surface that is geologically antique as well as one that is subject to very little erosion (Melosh, 1989). For Mercury and the Moon, the state of decay of their craters has been used to formulate a relative geologic timeline.

Even the absence of impact craters on the surface of a rocky or icy world can give valuable geologic information about the world itself. Regions of a planet's surface possessing below-average numbers of impact craters imply that those regions have been resurfaced by some geologic process at some time in the planet's geologic history.

An impact crater is not the only thing left behind by the impact cratering process. This is especially true for the youngest, and therefore freshest-looking, impact craters, where such things as impact-melt deposits and ejecta blankets can be seen about the crater itself. The manner that melt and other ejecta are emplaced about craters can give scientists

insight about the impactor that was responsible for the crater, as well as about the body the impactor struck.

Hawke and Head (1977) outline four means by which to tell whether a melt deposit, in this case on the Moon, is impact- or volcanic-related: 1) a deposit distribution that differs from normal volcanic melt-emplacement schemes, 2) lack of obvious volcanic sources where the deposit is located, 3) morphology of the melt deposit that rules out volcanism, and 4) time of emplacement of the deposit is well outside any known periods of volcanism. Hawke and Head (1977) also note that pre-impact topography and impact direction of the projectile are the most important factors in controlling the first of the above four aspects. Chadwick and Schaber (1993) studied melt deposits about Venusian craters, and found a predominant downrange direction, that is opposite from the crater to where the shadow zone of the ejecta blanket is located, of flow for these melts. Such a non-random distribution is in accordance with what Hawke and Head (1977) have posited. Neish et al. (2014) performed a similar study on lunar craters, and found a very different, yet equally non-random, distribution to the emplacement of impact melt about those craters.

Neish et al. (2017) compared the emplacement schemes of melt-bearing craters on the Moon and Venus, and proposed that one of two factors is likely to control melt emplacement on rocky bodies: 1) the planet's pre-existing surface topography, or 2) the planet's surface gravity strength. If 1) holds more sway, then it means worlds with high topographic variation, such as being heavily cratered like the Moon and Mercury, can be expected to follow the same pattern as was found on the Moon while less variable surfaces should pattern after Venus. If 2) holds more sway, then the emplacement pattern exemplified on the Moon is indicative of low surface gravity while the pattern found on Venus should be indicative of high surface gravity.

Our work is tasked with determining which of these two factors have dominant control over melt emplacement on rocky bodies, or if another factor entirely is at play, and applying our study to the planet Mercury should be quite ideal for doing so. Mercury is heavily cratered like the Moon, yet has a higher surface gravity than the Moon does. How impact melt is emplaced about Mercurian craters should therefore tell which of the

two factors is predominant, and subsequently can allow for the creation of a model that can predict how melt produced by impact events on any given rocky body will predominantly be emplaced. Such a model, more importantly, should also be able to predict either a planet's surface topographic variation or surface gravity strength, depending on which holds greater sway, based on the emplacement paradigm found on that world. Once the model's predictive capability is determined, it will have great potential for worlds like the Earth whose impact craters are usually heavily eroded and hard to find.

1.1 The Impact Cratering Process

Impact craters are a prominent feature of most solid bodies in the Solar System. These craters can provide invaluable information about the host body's subsurface morphology. This is made possible through exposure of the subsurface material in outcrops on crater walls and, for large-enough craters, central uplifts (Osinski and Pierazzo, 2013).

Melosh (1989) contends that impact cratering as a phenomenon must obey physical laws, regardless of the host body in question. That is, factors such as the target's surface gravity should affect the structure of any given crater because it affects the impactor velocity of the projectile in a manner that can be calculated and modeled reliably.

Osinski and Pierazzo (2013) add further that each target body has unique aspects to them that also affect the impact cratering process resulting in craters that can differ between differing celestial bodies. For example, the Moon possesses virtually no atmosphere and as such its craters remain recognizable on its surface for long geologic periods while the atmospheres of Mars and Venus act, to some degree, on the incoming impactor and later modify any resultant crater through exogenic processes.

Gault et al. (1968) distinguished three primary stages of the formation process in most impact cratering events: 1) contact and compression, 2) excavation, and 3) modification (Figure 1). Kieffer and Simonds (1980) also propose a fourth stage: hydrothermal/chemical alteration.

This entire process begins the moment when the impactor strikes the surface of the target. From that instant, the "contact and compression" stage takes place. During this stage, the

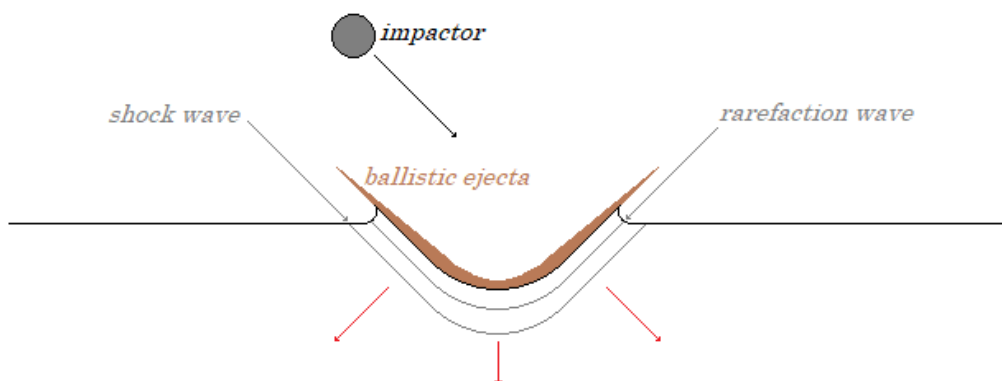
high kinetic energies involved are transferred both into the target and back onto the projectile itself (Melosh, 1989; Ahrens and O'Keefe, 1972) resulting in shock-induced alteration of both bodies. This shock comes in the form of tensional waves that immediately follow the initial compressional shockwaves that were released into the target upon impact; the resultant decompression from the tensional-wave propagation gives way to melting, and even vaporization, of both the projectile and the nearby target material (Gault et al., 1968; Ahrens and O'Keefe, 1972; Grieve et al., 1977; Melosh, 1989).

During the second stage, the crater itself begins to form (Figure 1). A quick succession of interrelated interactions between the various shockwaves and the host body give rise to what has been termed a "transient cavity," (Dence, 1968; Grieve and Cintala, 1982; Melosh, 1989). Depending on the travel directions of the shockwaves at any given area of the transient cavity, either "excavation" of target material from the cavity itself will occur, or "displacement" of the material from its initial location within the cavity occurs. The displaced material remains mixed with melt-rich material on the "floor" of the cavity while the excavated material is ejected to form the "ejecta blanket" about the cavity (Oberbeck, 1975).

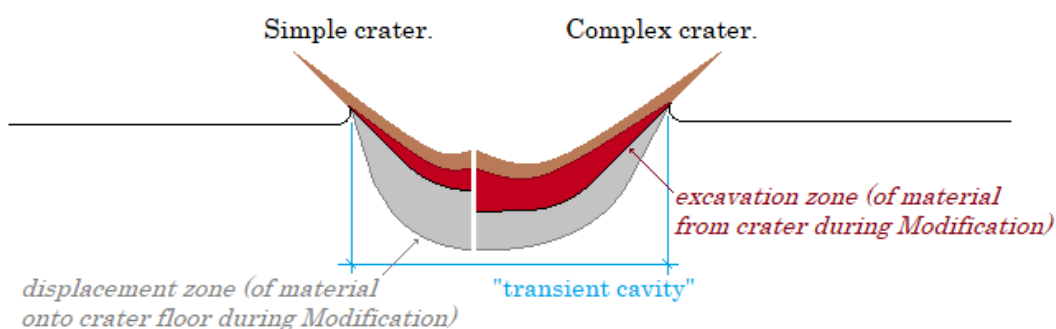
The excavation stage transitions seamlessly into the modification stage of crater formation, where the transient cavity quickly assumes the crater's "final form." The final form of the crater is a function of the host body's surface gravity and the nature of the area on the target body that was struck (Melosh and Ivanov, 1999). The surface gravity plays an important role in distinguishing the threshold below which little transient-cavity modification occurs producing a "simple" crater and above which further, gravity-driven modification of the cavity occurs producing a "complex" crater that possesses a "central uplift" (Dence, 1965; Melosh, 1989). This stage might be marked by a secondary ejecta process that occurs, where the forces responsible for this stage can also impart enough energy in some of the melt-rich material to move that material from the crater floor and onto the rim and even outside the crater itself to form exterior melt deposits (Grieve et al., 1977; Osinski et al., 2011; Osinski and Pierazzo, 2013).

The modification stage has no definite “end”; further modification even long after the crater attains a more permanent form can occur, both by internal faulting and the so-called “hydrothermal/chemical alteration” stage (only pertinent to certain celestial bodies; see Naumov, 2005, Osinski et al., 2005, and Osinski et al., 2012).

Contact/compression stage:



Excavation stage:



Modification stage:

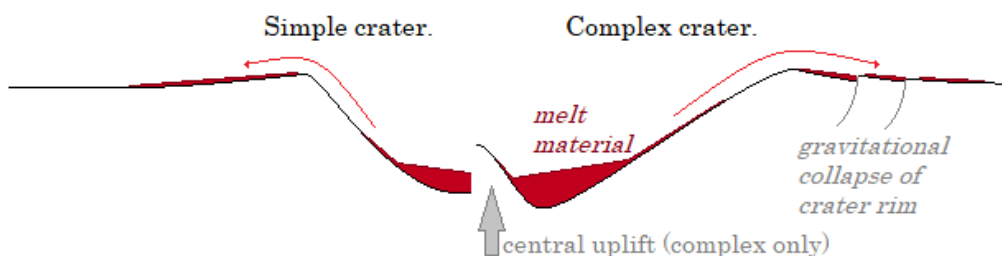


Figure 1: The primary stages of crater formation, based on Osinski et al. (2011), with simple craters on the left and complex craters on the right.

The final crater assumes one of two predominant forms: 1) simple, or 2) complex.

Simple craters are recognized by their bowl-like shape and depth-to-diameter ratios typically between 1:5 and 1:7, while complex craters are defined by their terraced walls, flat(-ish) floors, and central uplifts with depth-to-diameter ratios of 1:10 to 1:20 (Melosh, 1989; Osinski and Pierazzo, 2013). There are other crater forms known to exist, almost exclusively for the largest possible impact events, but these may be considered as a continuum upward from the complex crater form.

1.2 Impact Melt Generation and Emplacement

As described above, melt generation and later emplacement is an important part of the impact cratering process.

Impact-generated melt can morphologically resemble melts produced by other means, such as by volcanism, but the means by which impact-generated melt is created are notably different than most other ways of forming melt. For example, volcanic melts are generally produced via either decompression melting occurring deep within the lithosphere or by eutectic-point lowering from the introduction of volatiles (also deep within the lithosphere). In contrast, impact-generated melts are produced via decompression melting occurring during the passage of the tensional shockwave during an impact cratering event. In particular, impact-generated melts, because they result from adiabatically-released “waste heat,” often start off as superheated material (Grieve et al., 1977).

Impact melts have been observed on Earth (e.g., Marvin and Kring, 1992; Osinski et al., 2011), the Moon (e.g., Hawke and Head, 1977; Cintala and Grieve, 1998), Mars (e.g., Tornabene et al., 2012; Boyce et al., 2012), Venus (e.g., Chadwick and Schaber, 1993; Grieve and Cintala, 1995), Ceres (e.g., Krohn, 2016; Sizemore, 2017), Vesta (e.g., Denevi, 2012), and Mercury (e.g., Susorney et al., 2016; Leight and Ostrach, 2018).

Melt deposits are observed to take on one of three forms, as typified in Hawke and Head (1977)’s study of the Moon: 1) ponds/pools, 2) flows, and 3) veneers. Melt ponds (Figure 2) can be identifiable by their smooth appearance in imagery, with associated cooling cracks and pitted material. Melt flows (Figure 3) often look volcanic in

appearance, possessing lobate features, leveed channels, and flow textures. Flows are not always observed in visible imagery, but with radar imagery they stand out with their high back-scatter at the cm- to dm-scale compared to surrounding terrain on Venus, Mercury, and the Moon (Chadwick and Schaber, 1993; Neish et al., 2013; Neish et al., 2014). Finally, veneers (Figure 4) are thin and they coat the terrain instead of covering (flows) or infilling (ponds) the area; these are most difficult to pick out in satellite imagery, and usually high-resolution imagery is needed to effectively locate such melt deposits (Osinski et al., 2011).

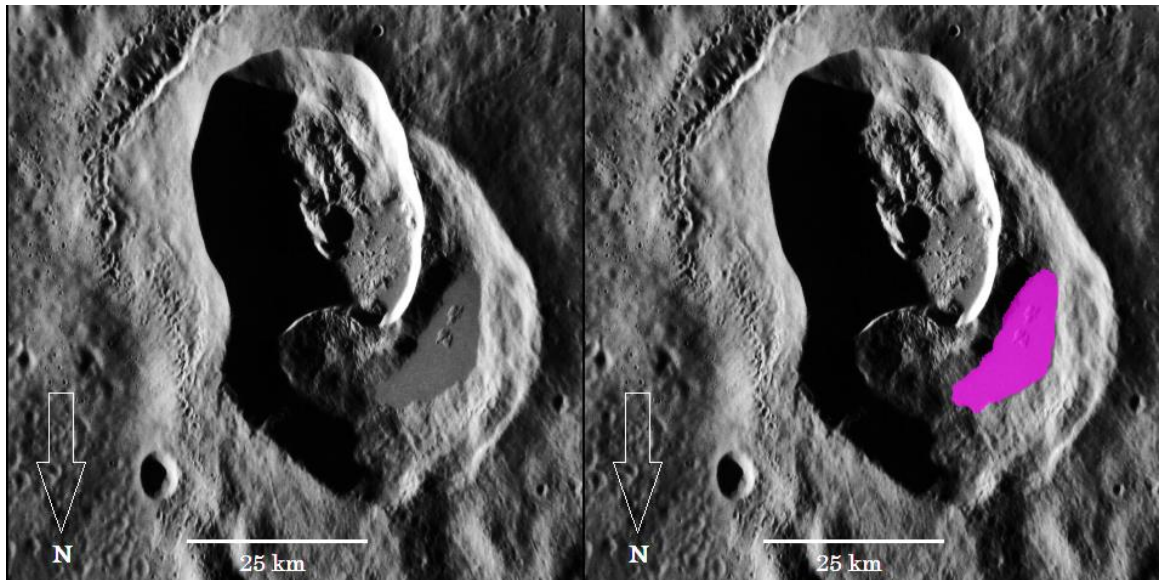


Figure 2: Left = MDIS-NAC image (CN0213154766M) of Ailey Crater showing exterior melt pond in an adjacent, older crater; contrast enhanced to help bring out melt pond more clearly. Right = same image, with melt pond marked out in purple.

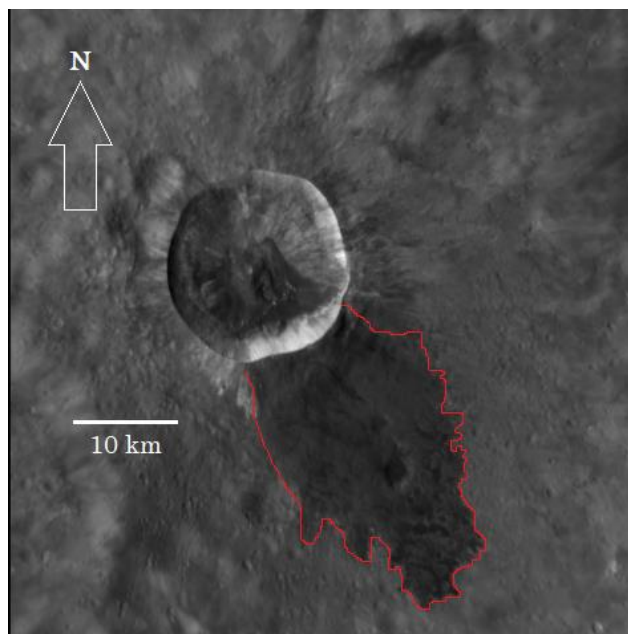


Figure 3: MDIS-NAC image (CN0229495136M) of Waters crater in Mercury's southern hemisphere, with predominant melt flow highlighted by red line.

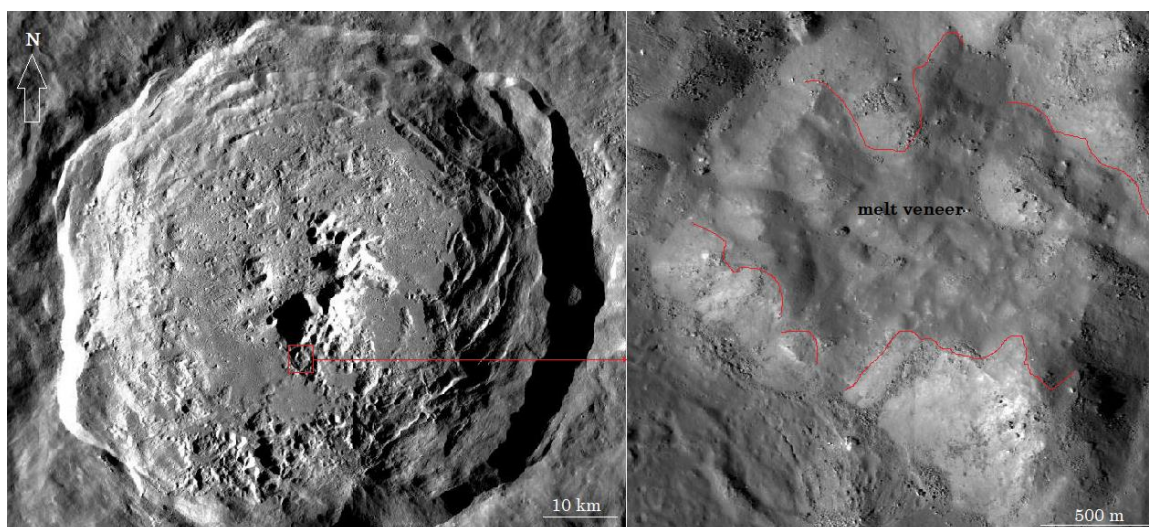


Figure 4: LROC-NAC mosaic of lunar crater Jackson, viewed using the Quickmap program provided by Arizona State University; inset shows an example of melt veneer (slightly darker material overlaying surrounding rocks, highlighted by red lines) on part of the central uplift (see Osinski et al., 2011). While there should also be veneers on Mercurian craters, most of the MDIS-NAC imagery is generally too low in resolution to properly identify such veneers.

It is unclear how these melt deposits were emplaced. One idea is that they were emplaced during the early stages of crater modification, when cavity walls begin to slump downwards to form the crater walls and the central uplift rebounds upwards (Hawke and Head, 1977). These actions impart energy and momentum into the melt material, which can push them up and over the crater rim. Some exterior melt deposits are found downrange of the crater, which implies that the direction of impact plays a role in the emplacement location of those impact melts. In such cases, remnant momentum from the impactor may be imparted into the generated impact melt such that the possible directions the melt would otherwise have been able to leave the crater are restricted to that given direction. This case is more likely when the angle of impact is also very shallow with respect to the planet's surface (Chadwick and Schaber, 1993).

Some of the resulting melt is deposited on the crater rim, but some of it can travel beyond the crater rim, flowing in response to topography (Hawke and Head, 1977, Melosh, 1989).

1.3 Mercury

Mercury is the innermost planet in the Solar System. A heavily-cratered world lacking any permanent atmosphere, much of what has been discovered about Mercury's surface, interior, and overall composition was made possible by the MESSENGER spacecraft. MESSENGER (MErcury Surface, Space ENvironment, GEochemistry, and Ranging) was launched in 2004, entered orbit about Mercury in 2009, and crashed into Mercury's surface in 2015. This space probe was designed to answer the following questions (Solomon et al., 2007): 1) What process resulted in the abnormally high metal-to-silicate ratio on Mercury? 2) What is Mercury's geologic history? 3) What form does Mercury's magnetic field take, and how is it produced? 4) What is the structure of Mercury's large core? 5) What is the identity of the radar-bright material in some of Mercury's polar craters?, and 6) What are the primary volatiles on Mercury, and where might these volatiles have originated?

After two Venus flybys, followed by two Mercury flybys, the spacecraft was inserted into Mercury orbit with the intention of observing the planet for at least two years. The orbit

was highly elliptical, with the closest approach over the north pole of the planet. Figure 5 illustrates the nature of MESSENGER's orbit around Mercury, showing its orbital path during its main mission.

MESSENGER was the first mission to completely map Mercury's surface (the previous Mariner mission was only able to image one hemisphere). To do this, it used its MDIS (Mercury Dual Imaging System) NAC (narrow-angle camera) and WAC (wide-angle camera) systems to produce a global mosaic of Mercury's surface.

Other systems that were on-board MESSENGER include its laser altimeter (the MLA), geophysical sensors (magnetometer, gravity), and instruments designed to analyze Mercury's surface composition (like the Gamma Ray Spectrometer). This thesis makes use of the MDIS and MLA instruments, and the data products obtained from them.

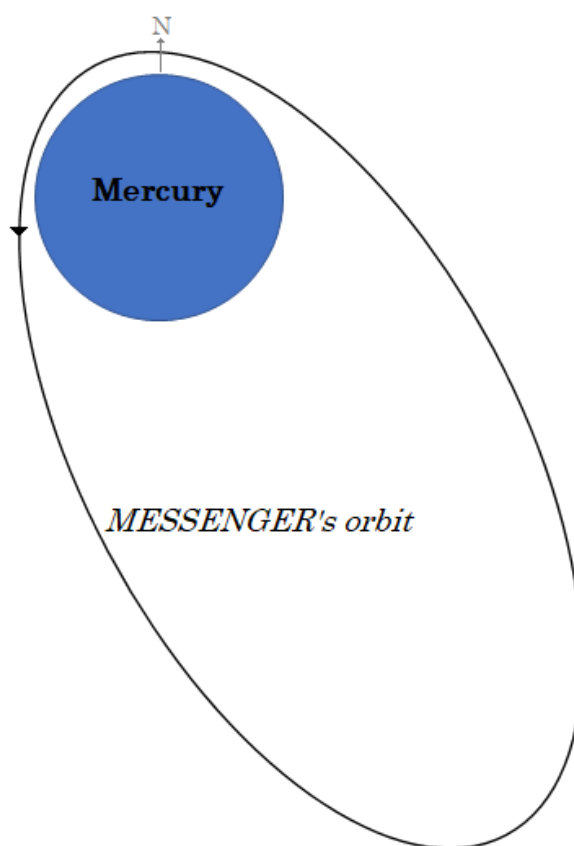


Figure 5: MESSENGER's orbit about Mercury during its main mission conducted from 2009 through 2011 (see Solomon et al., 2001). The spacecraft's orbit was very elliptical, with its closest approach occurring over Mercury's northern hemisphere.

MESSENGER's MDIS instrument was purposed for visually imaging Mercury's surface, and was comprised of two components: the monochrome NAC, and the multispectral WAC (Hawkins, III, et al., 2007). The NAC had a 1.5° field of view (FOV), coaligned with the WAC that, in turn, had a 10.5° FOV. While both cameras were mounted on the same frame, only one camera ever operated at any one time. Between these two cameras, a total of four visual-imagery datasets resulted: 1) a monochrome, global mosaic map, 2) a stereo complement-map of the monochrome map (which is still being constructed), 3) a low incidence-angle mosaic map, and 4) high-resolution imagery of select, target locations across Mercury's surface (Hawkins, III, et al., 2007).

The MLA instrument was a laser altimeter. It operated by measuring the round-trip time of emitted laser pulses that have been reflected back from Mercury's surface in order to gather high-quality topography data of Mercury's surface (Cavanaugh et al., 2007). So long as the altimeter was within 1,200 km of Mercury's surface or the slant range corresponded to within 800 km of Mercury's surface, high-quality topography data at meter-level accuracy could be obtained (Cavanaugh et al., 2007). Unfortunately, due to MESSENGER's highly elliptical orbit and the nature of the altimeter itself this high-quality dataset could only be acquired for Mercury's northern hemisphere and especially north of 45°N . Because of MESSENGER's orbit, the MLA tracks are almost all longitudinal in orientation. This also means the error in the MLA data can easily become quite large outside of that "sweet spot" region of Mercury's northern hemisphere. Because of this, while we used the MLA data to ensure alignment of the USGS DEM data with the MDIS mosaic for each crater we used the USGS DEM for our analyses for its better-known uncertainty values.

Mercury's interior structure has recently been modeled as being more complex than earlier models suggested (Solomon and McNutt, Jr., 2007). Mercury's core has recently been theorized, and has now been determined via the magnetometer and gravity readings from MESSENGER, to be partitioned much like Earth's core. Genova et al. (2018a) modeled a three-part, iron-rich core, with a solid inner core and a liquid outer-core layer bounded by a second solid layer abutting the mantle. Genova et al. (2018b) used geophysical modeling to constrain Mercury's inner core to be roughly 50% the radius of

the liquid outer core. MESSENGER's magnetometer also confirmed that Mercury's magnetic field is global, albeit not as strong as Earth's (Anderson et al., 2011). The structure of Mercury's silicate crust has also been modeled using geophysical data from the MESSENGER mission. Sori (2018) determined that the crust is fairly thin at around 26 km thick on average. King and Robertson (2018) modeled the interior geodynamics of Mercury over 4.5 billion years and determined the most accurate model for the evolution of Mercury's interior produces a silicate-rich "shell," around Mercury's large core, that is roughly 360 km thick.

Mercury's surface is also more complex than previously thought, possessing more than just impact craters. Other notable features include: 1) lobate scarps and rill-like features, which were formed during the prolonged period of global contraction of Mercury's crust fairly early in its geologic history (Watters et al., 2009; Galluzzi et al., 2018), 2) plain-like expanses reminiscent of lunar mare that imply resurfacing in those areas (Head et al., 2011; Galluzzi et al., 2018), 3) craters in polar regions that possess volatiles, like water-ice, within them (Chabot et al., 2012, 2013), and 4) so-called "hollows," which imply a volatile-rich host rock in those places (Blewett et al., 2011; Lucchetti et al., 2018).

There is also the presence of at least two, probably three (see Galluzzi et al., 2018), distinct, comparatively lightly-cratered regions, called "plains," first noted by the Mariner spacecraft (Galluzzi et al., 2018, and sources therein) has age-restricting implications and helps give insight into the resurfacing history of Mercury. Galluzzi et al. (2018) proposes a formation history for the three different plains regions, the Smooth Plains (SP), Intercrater Plains (ICP), and Intermediate Plains (IMP), based on relative lack of craters and relative prevalence of undulating surfaces: the SP, possessing the smallest number of craters and the greatest concentration of undulating surfaces, is therefore the youngest; the IMP, which is more heavily-cratered but still possesses undulating surfaces, is the next oldest feature; the ICP, then, which is most heavily-cratered of the plains regions and possesses no undulating surfaces, is the oldest.

Even Mercury's craters are fairly unique in their structure. Recent work by Herrick (2018) has found that Mercury's complex craters do not nicely transition into peak-ring forms like they do on the Moon, but express five separate classes, "central peak"

(“normal” complex craters), “multiple isolated peaks,” “ringed peak cluster,” “protobasin,” and finally “peak ring” (“normal” peak-ring basins). He notes a fairly non-random distribution for many of these crater classes, which he theorizes may be due to regions of somewhat differing geologic properties present where each class of complex crater is forming. Work by Baker et al. (2018) has also found that basin-like structures, akin to Mare Orientale on the Moon, do not conform to the form seen on the Moon. This is probably due to a filling-in of the structures similar to Mare Orientale-type craters.

Mercury’s plains can generally be distinguished from the rest of Mercury’s surface by a comparative lack of craters. This fact implies these plains are geologically younger than the rest of Mercury’s surface. Peplowski et al. (2011), using radioactive potassium, thorium, and uranium isotope data from MESSENGER’s Gamma Ray Spectrometer, determined that these plains likely started forming from widespread volcanism shortly after the end of the late heavy bombardment roughly 3.8 billion years ago. This is consistent with Head et al. (2011), and their work concluding that these plains formed not long after the formation of the Caloris basin.

There is also the intriguing conundrum of Mercury’s global crustal contraction. Watters et al. (2009) note an average surface strain that resulted in up to 2 km worth of reduction in Mercury’s average radius over the past four billion years. The formation of the lobate scarps and “wrinkle ridges” that accommodated this contraction is thought to have occurred at the tail-end of the plains formation period of Mercury’s geologic history, and then continued for some time after the volcanic activity ceased as Mercury’s interior slowly cooled (Watters et al., 2009).

1.4 Impact Melt Emplacement about Mercurian Craters

The new MESSENGER data allows us to investigate the emplacement of impact melt around craters on Mercury for the first time. However, prior work has examined impact-melt emplacement on other rocky bodies in the solar system. For example, Neish et al. (2014) discovered that exterior melt deposits around lunar complex craters are commonly concentrated near the lowest elevation of the crater’s rim – termed the “rim crest low,” or RCL, in their study. Further work by Neish et al. (2017) determined that this same trend

did not hold for Venusian complex craters, as shown in Figure 6. They hypothesized that since lunar craters are deep with respect to diameter and possess comparatively small amounts of impact melt, the melt that is ejected can only escape out the RCL. On the other hand, Venusian craters are comparatively shallower and possess far more melt than lunar craters (Figure 7). This means that melt emplacement on Venus is far less governed by crater topography than it is on the Moon. Neish et al. (2017) propose the driving factor on Venus is likely impactor direction, producing a predominantly downrange flow for many of these melts (see also Chadwick and Schaber, 1993).

In this thesis, we seek to determine the mechanism by which melt is emplaced around fresh craters on terrestrial planets. On Mercury, as an example, the youngest craters are characterized by pristine floors, steep walls, and high-albedo ejecta and are classed as “Kuiperian” craters; the second-youngest craters maintain the pristine floors and steep walls, but lack the characteristic ray ejecta, and are classed as “Mansurian” craters; the next-oldest craters possess cratered floors and lack any visible ejecta material, and are classed as “Calorian” craters; the oldest craters, then, are those that lack a pristine floor, have eroded walls, and lack any ejecta material (see Barlow and Banks, 2018). This project will focus primarily on melt-bearing Kuiperian craters, since those craters are most likely to have preserved ejecta blankets and melt deposits.

The Moon and Venus represent two end members with regard to gravity. We therefore need to study the fresh impact craters on a world that, in many respects, lies intermediary to the Moon and Venus: Mercury. Mars, at first glance, also fits here, but its atmospheric dynamics, unlike on Venus, serve to quickly cover up and eventually erode away the notable impact features there. Since Neish et al. (2017) studied only complex, fresh craters on the Moon and Venus, this study also only looked at complex fresh craters on Mercury. These larger craters are also easier to study given the limited resolution of the MESSENGER data sets.

This thesis is divided into five main chapters, including this one. Chapter 2 will detail the methodology applied to this study, including identification of suitable craters, and analysis of these craters for pertinent features like melt deposits and RCL. These results, presented in Chapter 3, will then be compared and contrasted to those of Neish et al.

(2017) for the Moon and Venus. In Chapter 4, we propose a theory to explain the observed melt emplacement patterns seen on the Moon, Mercury, and Venus, elaborate on the short-comings encountered in this work and therefore what future work looking into the patterns of melt emplacement on rocky worlds should consider and, ideally, resolve, and investigate the implications for melt emplacement on other worlds like Mars, Ceres, and Vesta. Lastly, Chapter 5 will comprise a concise summary of the important information in this thesis as well as concluding remarks.

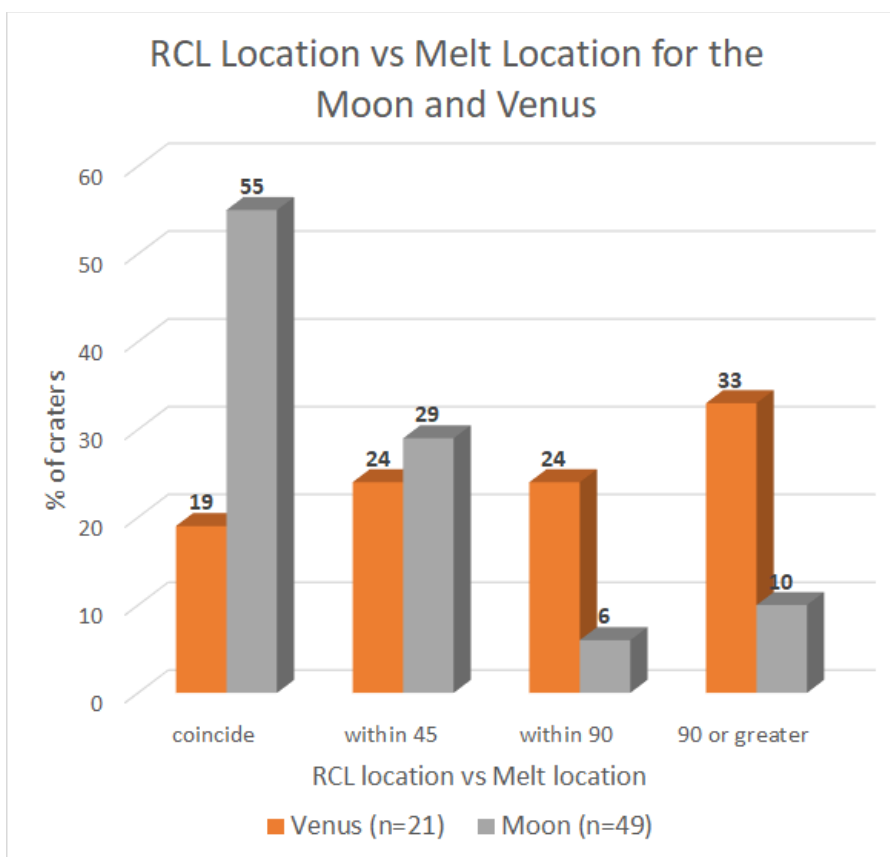


Figure 6: The melt direction of fresh, complex craters on the Moon and Venus, compared to the direction of the crater’s RCL as determined from Neish et al. (2017). The melt and RCL are either “coinciding” (RCL and melts lie in the same direction from the crater’s center), “within 45” (melts are within 45° from the RCL), “within 90” (melts lie between 45° and 90° from the RCL), or “90 or greater” (melts lie on the other side of the crater from the RCL). Over half of lunar complex craters lie within the “coincide” regime, whereas on Venus the distribution is fairly even across all four regimes.

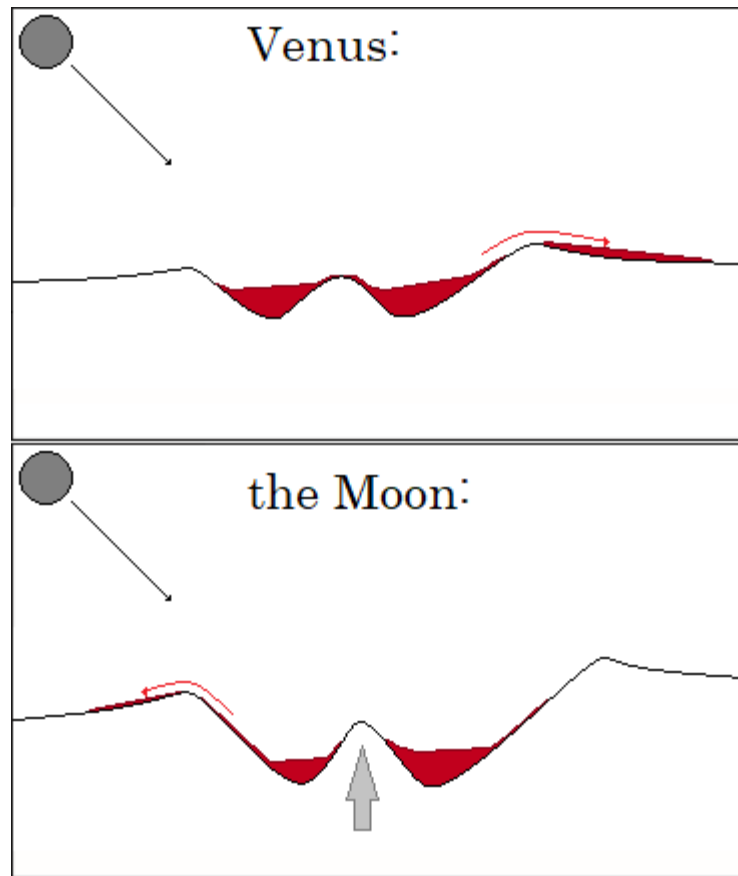


Figure 7: Illustration of the hypothesis proposed by Neish et al. (2017). They theorize that the greater melt production combined with comparatively shallower crater depths on Venus mean the melt that is ejected is not constrained by the crater topography, but instead likely by impactor direction. In contrast, crater formation on the Moon produces comparatively deeper craters as well as notably lesser melt material. As such, the ejection of melt is constrained by this greater average topography and usually only has enough energy to leave the crater, if it does, out its RCL.

Chapter 2

2 Methodology

This section details the methods that were used to complete this work, including the datasets utilized and the programs and software used to acquire and analyze the data.

The first objective was to search for suitable complex, fresh craters that bore exterior melt deposits on Mercury. This task was accomplished by searching through the Kuiperian crater dataset compiled by Braden and Robinson (2013) and the rayed craters dataset compiled by Banks et al. (2017). These two datasets were used as a starting point because Kuiperian craters are listed, and as these craters are the freshest on Mercury they are most likely to possess recognizable impact-melt deposits. Also, the latitude and longitude of these craters were already given and pieces of pertinent information, particularly whether ejecta rays existed for the craters or not, were also already available without the need for us to acquire these data. Other melt-bearing craters were also discovered by analyzing MDIS global mosaic data available through the Mercury QuickMap website.

Next, the most promising craters were processed using ISIS3 (a data manipulation software that was developed by the USGS to process datasets from NASA's publicly accessible Planetary Data System) and crater files were created in QGIS (a free-to-use GIS software, similar to ArcGIS, that allows for the visualization of data manipulated by ISIS3 as well as further manipulation such as creating shapefiles and measuring distances).

The resolution of the MDIS global mosaic was generally too low to accurately resolve the emplaced melt deposits, so MDIS-NAC swatches were also acquired, from the Mercury Orbital Data Explorer (MODE). In rare cases, these swatches were necessary to accurately resolve the crater itself. These swatches were then added to the QGIS file, and shapefiles for the melts and rim were drawn.

Finally, statistical analyses were conducted on the craters selected to be part of the final catalog for this work. RCL and melt locations were determined, as well as average rim

height and crater depth. These data were then compiled in an Excel spreadsheet, serving as our catalog for this work. A low incidence-angle variant of the MDIS global mosaic was then used to analyze rayed craters possessing an asymmetric ray pattern to determine impactor direction. Results here were added to the spreadsheet and incorporated into the final analyses. The final results were then compared to work by Neish et al. (2014) and Neish et al. (2017), and conclusions drawn from them.

2.1 Data Acquisition

This work aims to determine what factors influence impact-melt deposition about craters on Mercury, so identifying melt-bearing craters was a necessary first step. Because impact-melt deposits and ejecta blankets weather away rather easily, over geologic time, the craters that we study here are relatively young in age (Kinczyk et al., 2018a). On Mercury, the youngest craters (those aged less than one billion years) are classified as “Kuiperian”; these craters are most easily identified by the high-albedo ejecta rays that radiate out from them (Barlow and Banks, 2018).

Once the craters were identified, QGIS files were made for each of the craters with MDIS, MLA and USGS DEM, and shapefile data overlain on one another to highlight the locations of the melts, the crater rim, and the crater floor. The MDIS, MLA, and USGS DEM maps are all publicly available from the Planetary Data System. The Low Incidence-Angle MDIS map, used to look at the crater rays, is also freely available from the same source. The MLA mosaic map, though higher in resolution (500 m/pixel), was reliable only for Mercury’s northern hemisphere with full coverage available only for latitudes north of $\sim 45^\circ\text{N}$ (see Cavanaugh et al., 2007). Becker et al. (2017), among other sources, note that the uncertainty in the MLA for this limited area of coverage (corresponding to an altitude of 1,300 km or less above Mercury’s surface) is less than 30 m though no exact values are given. As a result, we used the USGS DEM map for all our elevation and topographic-variation analyses (using the MLA only to ensure the USGS DEM for each crater was aligned with each crater’s MDIS image); from Becker et al. (2016) and Becker et al. (2017), the 665m/pixel USGS DEM map was created in ISIS3, using the *jigsaw* module. The resulting mosaic was made from several “control points” comprising the MDIS data that were accepted by the *jigsaw* module. This procedure

produced the MDIS-based DEM mosaic with a latitudinal root-mean-square (RMS) error of ~127 m, a longitudinal RMS error of ~134 m, and a radial RMS error of ~296 m (Becker, personal communication). This study required the use of vertical error values for the DEM, which means the radial error given above was used in the analysis.

2.2 Data Manipulation

For each crater, we extracted visual and topographic data and imported it into QGIS. To initially extract the data, we use ISIS3. This study required the use of MESSENGER-specific commands, as well as a number of basic data-processing commands. These commands are italicized in the text below.

First and foremost, each crater was cropped from both the MDIS mosaic and the USGS DEM (using MLA for alignment of the USGS DEM) maps. To accomplish this, the mosaic was rendered in *qview* to determine the minimum and maximum latitude and longitude coordinates to use for each crater.

Next, the *maptrim* function in ISIS3 was used to crop out each crater from the mosaic. The files were then rendered in QGIS, using the *pds2isis* function to convert each crop into a .cub (“cube”) file that QGIS can work with. However, the default map projection – equirectangular – is not ideal for the most northerly-lying craters in the catalog because in order to fit a 3D globe into the form of a 3D rectangle the north-most and south-most regions must be stretched horizontally and compressed vertically. To remedy this, we used the sinusoidal projection (Figure 8), centered over the crater itself, as this produces nearly-rectangular image files while leaving the crater itself undistorted. In addition, the MLA mosaic uses a different longitudinal coordinate system, 0° to 360° positive-east, than the MDIS and USGS DEM mosaics, -180° to +180° positive-east, so they cannot be overlain in QGIS. To remedy these issues, the *map2map* function was used to project all images to a sinusoidal projection centered on the middle of the cropped crater. Once imported into QGIS, the topography data was used to render contour lines using the “Contour” tool.

Next, shapefiles were created that outlined each crater’s rim, floor, and exterior melt deposits. The crater-floor and melt-deposit shapefiles are drawn as polygons, while the

rim shapefile was drawn as a line shapefile. An example of such shapefiles is given in Figure 9. The rim was drawn using the MDIS imagery and the crater's topography, essentially "connecting the dots" of high-points and ridge-lines evident from the contour lines that lie as near as possible to the MDIS visual of the crater's rim. For the crater floor, we outlined only that part of the interior of the crater that lies within the crater walls and is covered by melt-rich material; other interior features such as the central uplift or any material that has collapsed onto the floor are excluded. We then traced out all exterior melt ponds (or, melt flows in extremely rare cases) according to their smooth-looking, pond-like appearance in MDIS imagery compared to surrounding terrain. A suite of distinguishing features between the melt comprising the crater floor deposit and those exterior to the crater are given in Leight and Ostrach (2018), but for this study we focused on the abundance of clastic material, large in size, embedded within the floor melt. This is rarely present in the exterior deposits. Other features of impact melt, such as cooling cracks, are often only visible in the MDIS-NAC imagery due to its higher (~12 to ~120 m/pixel) resolution compared to the MDIS mosaic.

Finally, the "Measure" tool is used to measure the average diameter of each crater in meters. This is illustrated for Ailey crater in Figure 10. Two profiles were made across each crater, and these profiles were then averaged to give a crater diameter used in this study. The errors associated with these profiles are given in Table 1.

We then processed the MDIS Low Incidence-Angle map for each crater, to add them to the crater files as the final overlay for these files. Again, we used *maptrim* to crop the images and then *map2map* to re-project the data into sinusoidal form.

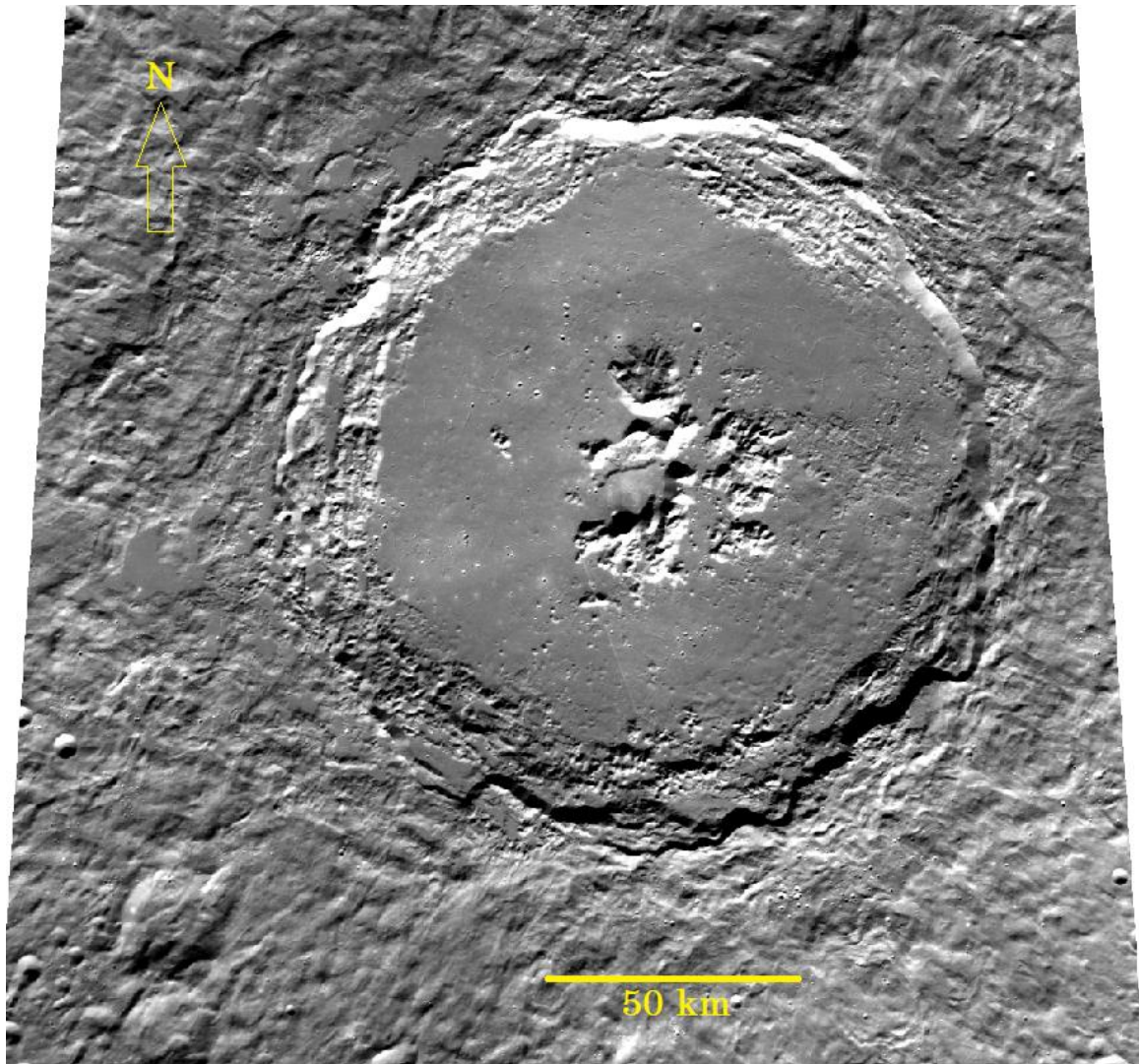


Figure 8: MDIS mosaic image of Abedin crater, rendered in QGIS with a sinusoidal projection centered on the crater. Re-projecting the image removes the distortions evident in the equirectangular projection.

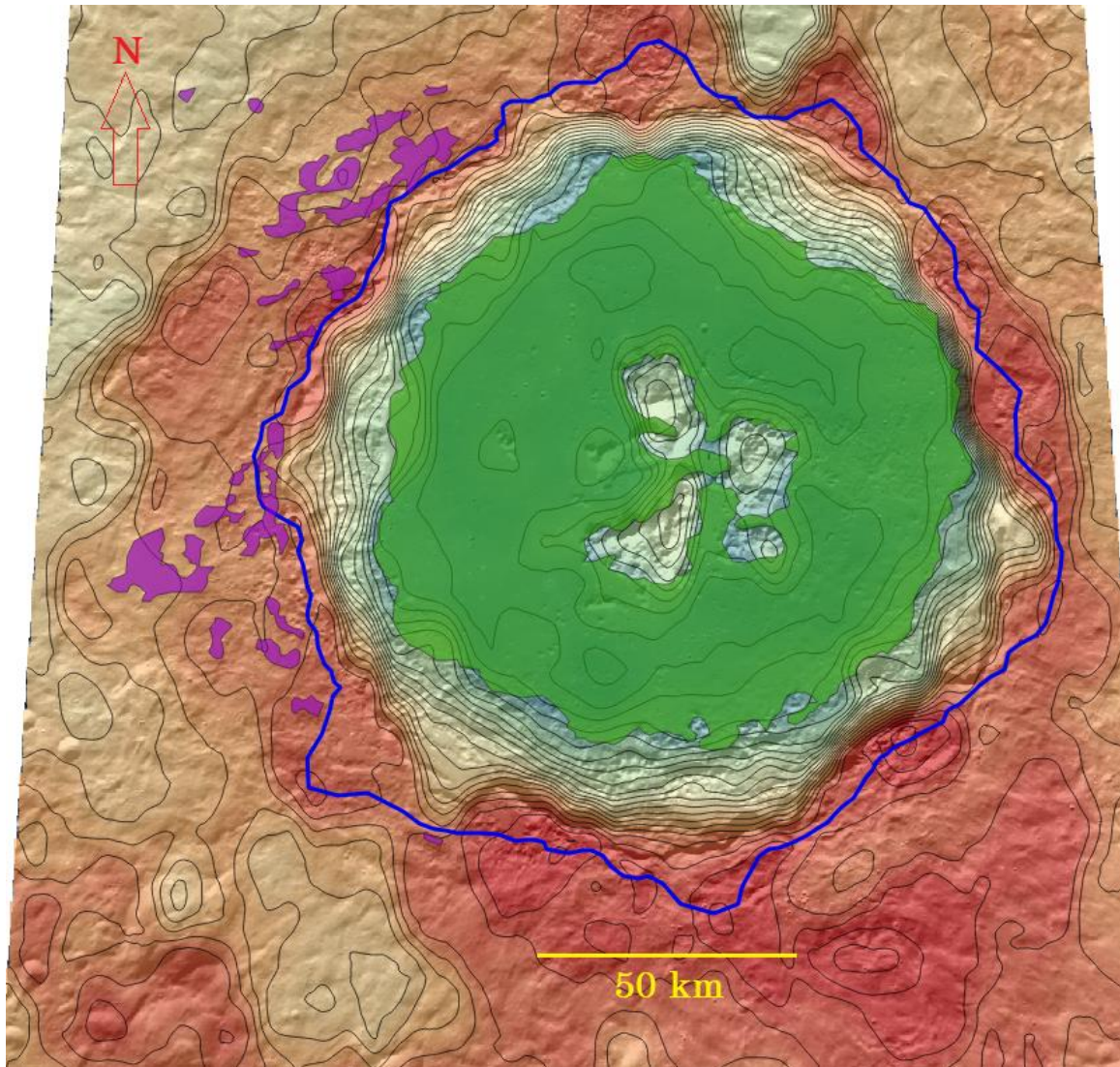


Figure 9: Abedin crater with USGS DEM overlaying the MDIS global mosaic image, and the melts and rim shapefiles over top them. The rim, in blue, was drawn using a line shapefile, while the crater floor, in green, and the ejected melt, in purple, were drawn using polygon shapefiles.

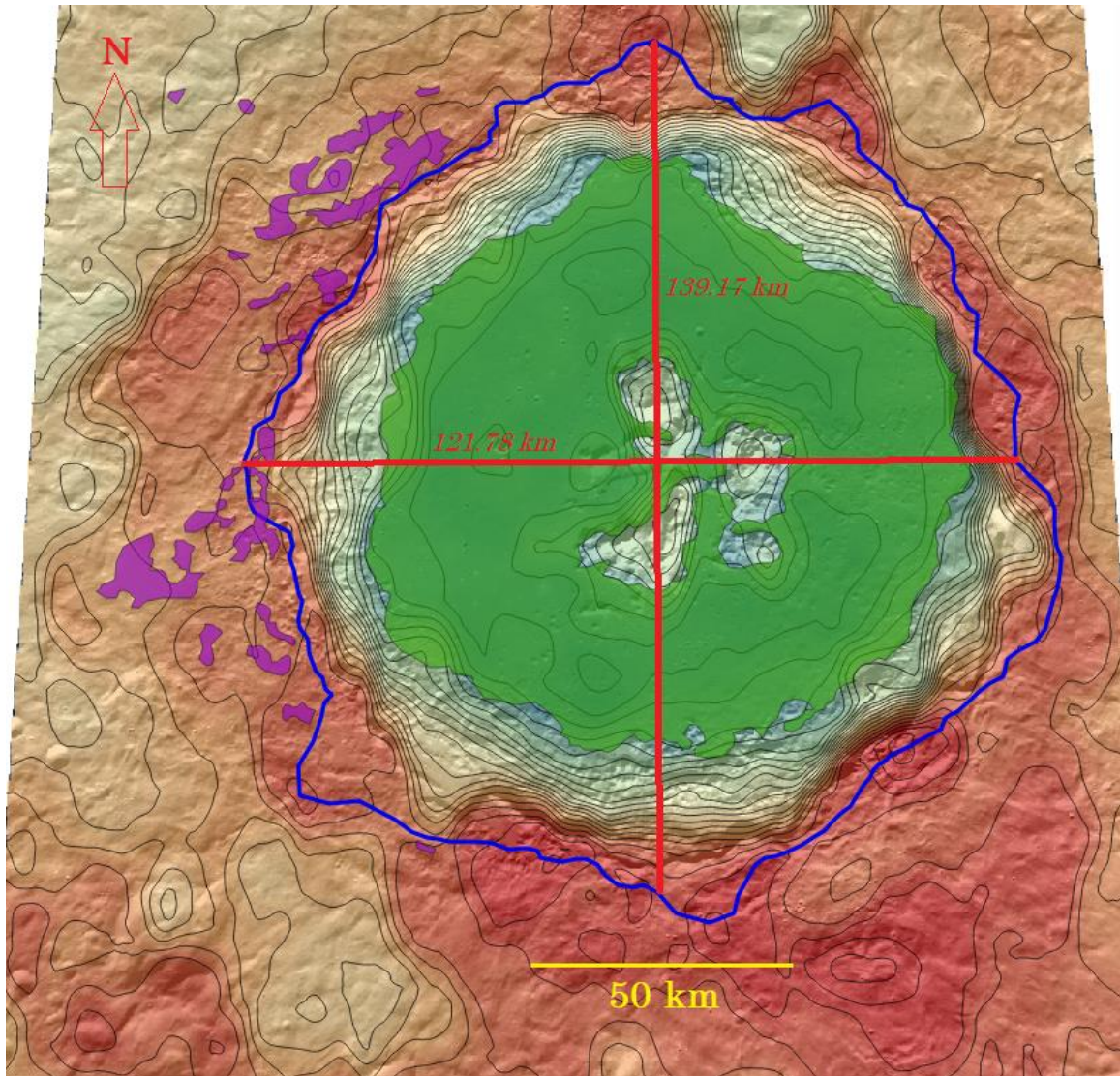


Figure 10: The crater-size determination process, as conducted using the “Measure” tool in QGIS. A traverse from W to E and a traverse from S to N (red lines) are then averaged to give an average diameter value that is used for later calculations.

2.3 Data Analysis

After the crater catalog was finalized and data for each crater was imported into QGIS, we analyzed the resultant data set to determine several key parameters. These included determining the depth of the crater, determining the variation in rim crest topography,

determining the direction of the RCL, and determining the primary location of the exterior melt deposits.

To determine the direction of the RCL and the primary location of the exterior melt deposits, the crater files were overlain on a sixteen-wedge, pie-shaped grid. Each wedge corresponds to one of sixteen compass directions, N, NNE, NE, ENE, E, ESE, SE, SSE, S, SSW, SW, WSW, W, WNW, NW, and NNW. The crater file is placed as the background layer, and the grid is placed on a separate layer over top the background. Lavender was used to highlight the wedge corresponding to the melt deposit location, and red was used to highlight the same but for the RCL. This is visualized in Figure 11, for Ailey crater as before.

The RCL, by definition, is the lowest elevation in the crater rim. As seen in Figure 12, this generally appears as a gap that opens up in the contour lines through the crater's rim. However, the rare exception existed where, as with Hokusai, the RCL was not obvious from the contour lines; here, the lowest elevation obtained from viewing the crater rim profile in QGIS was taken to be the location of the RCL. Another notable exception here occurred with a couple craters giving two separate instances where the contour lines opened up; again, here the lowest elevation obtained from viewing the crater rim profile in QGIS was taken to be the location of the RCL.

Similarly, exceptional cases existed in the determination of the melt deposit location. Generally, we assigned this direction based on the largest pooling of melt material outside the crater that was clearly derived from the crater itself. However, in some cases more than one distinct collection of melt material in which case the largest of them was used (all instances were recorded for completion).

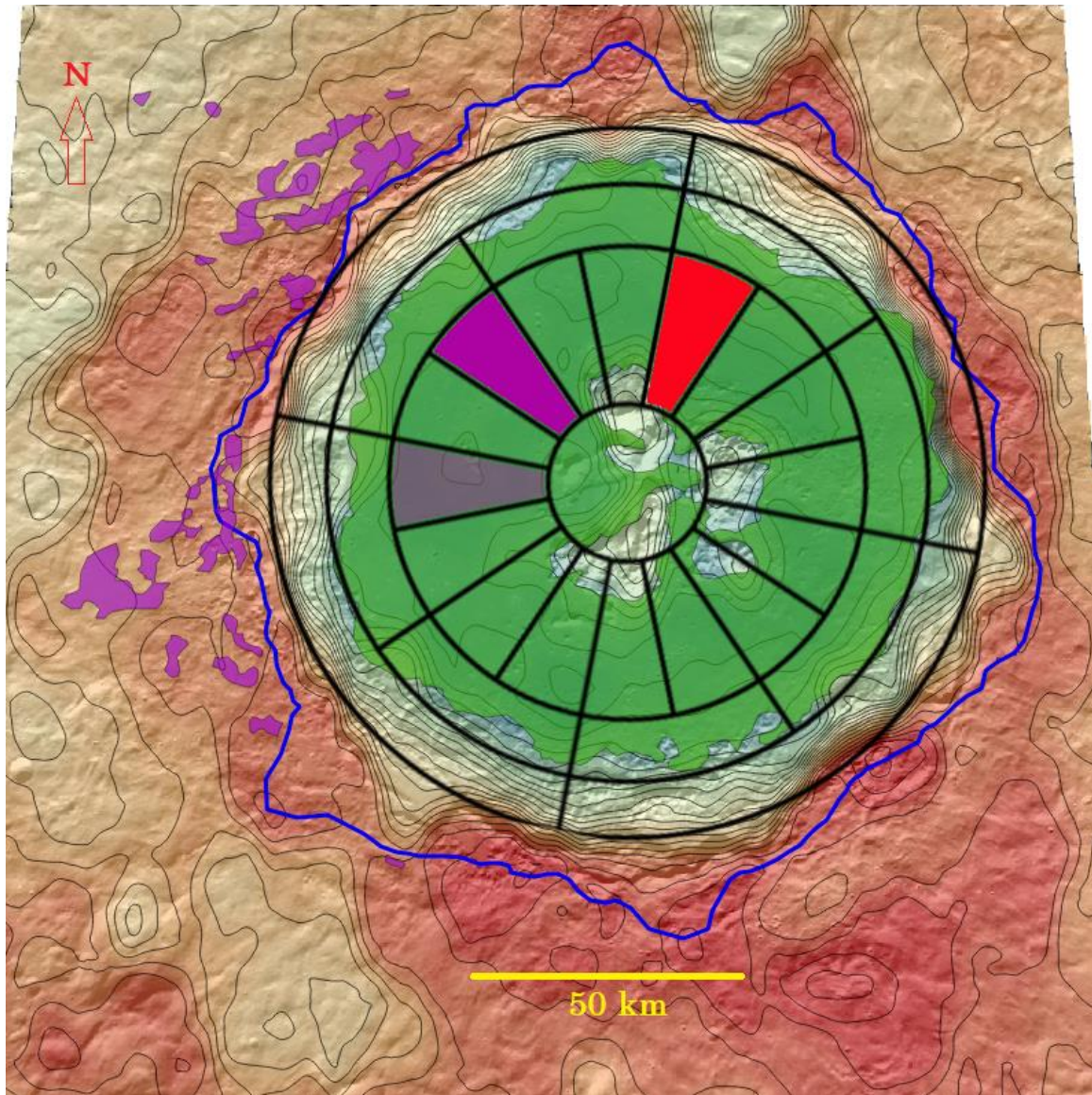


Figure 11: Abedin crater, with a sixteen-wedge grid overlain on the image. The RCL (red) and melt (purple) directions are highlighted on the grid. The smaller of the two main melt ponds are highlighted in a more transparent purple, while the larger one (used for further analysis) is marked by solid purple.

To determine the variation in the rim crest topography (see Figure 12), we performed a statistical analysis on the crater-rim shapefile paying particular attention to the maximum value (“RCH” = rim crest high), minimum value (“RCL” = rim crest low), average value (“avg.rim”), as well as the standard deviation. The first pair of values are useful in calculating the ratio R , which mathematically describes the topographic variation about

the crater rim (Equation 1a). The equation for calculating the error in R is given in Equation 1b (where “ err ” is the error in the USGS DEM data, and “ $d(err)$ ” is the error in crater depth given in Equation 2b).

The average value aids in calculating the depth, d , of the crater. To determine d , we performed zonal statistics on the crater-floor shapefile to extract the average elevation value (“ $avg.floor$ ”) and its standard deviation. Subtracting this value from the average rim elevation gives the depth (Equation 2a). The equation for calculating the error in d is given in Equation 2b (where “ $std.rim$ ” is the standard deviation of the crater rim, and “ $std.floor$ ” is the standard deviation of the crater floor).

$$R = (RCH - RCL)/d \quad \text{Equation 1a}$$

$$R(err) = R \cdot \sqrt{\left(\frac{(\sqrt{2(err)^2})}{(RCH-RCL)}\right)^2 + \left(\frac{d(err)}{d}\right)^2} \quad \text{Equation 1b}$$

$$d = (avg.rim) - (avg.floor) \quad \text{Equation 2a}$$

$$d(err) = \sqrt{((std.rim)^2 + (std.floor)^2)} \quad \text{Equation 2b}$$

These values will be given in Tables 1 to 3, and their products illustrated in Figures 17 and 18, in Chapter 3 along with the implications for these values and figures.

Rayed craters are useful in determining the direction at which the projectile struck the surface; the “forbidden zone” (Figure 13) is an area where ejecta rays are lacking, and this implies the projectile came in from that direction. However, asymmetric ejecta rays only occur for impact angles less than 45°; impactor angles greater than 45° will produce fairly symmetric ray patterns and impact direction cannot be determined. Angles near 20° can produce a unique pattern called a “butterfly.” For butterfly rays, two forbidden zones are created which also hinders impact direction determination; two possible directions are implied, instead of just one (Melosh, 1989).

To determine the direction of impact, we focused on the craters bearing clear, asymmetric ejecta rays and used the same sixteen-wedge grid to highlight the forbidden zone with a blue gradient in GIMP. We used a solid blue to mark the midway direction in the

forbidden zone, taking that to be the direction of impact (Figure 14). We compared the impact-direction grid to the melt and RCL locations grid for these craters in GIMP, determining whether the melt deposits lie more opposite to the forbidden zone (we defined this as “downrange”) or more on the same side of the forbidden zone (we defined this as “uprange”).

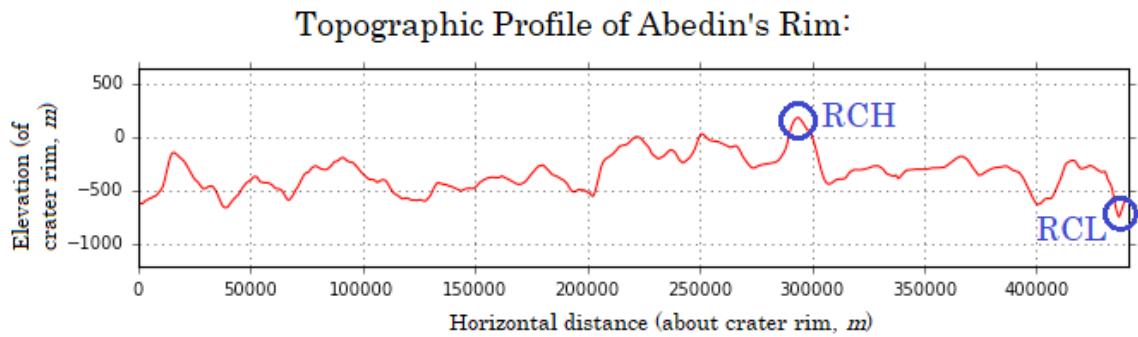


Figure 12: Topographic profile of Abedin’s crater rim, with the highest rim elevation (RCH) and lowest rim elevation (RCL) marked in blue. Figure 15 relates this rim profile to the crater’s image file.

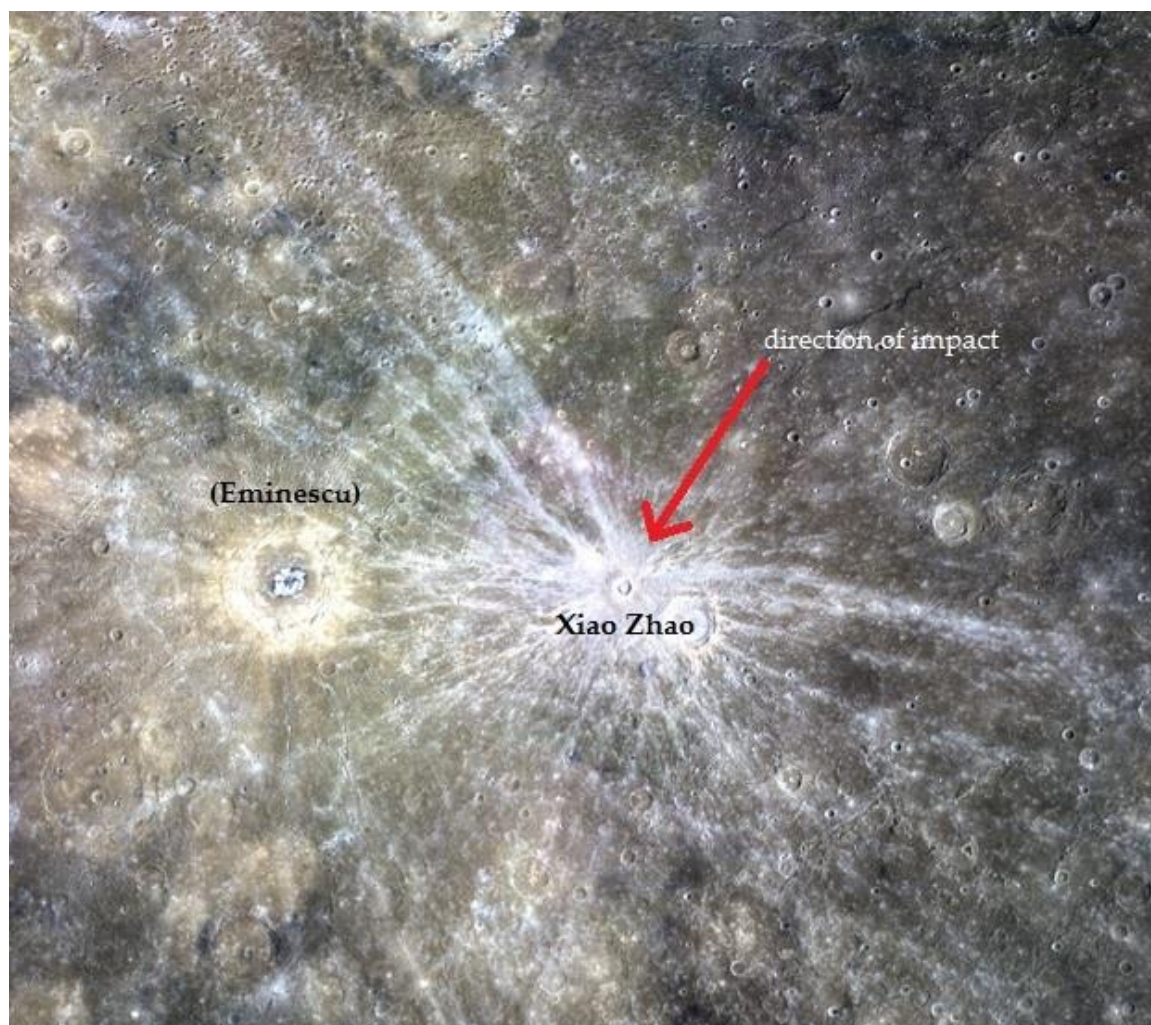


Figure 13: Rayed crater Xiao Zhao (Eminescu crater to the west), exemplifying an asymmetric ray pattern. The forbidden zone for Xiao Zhao is roughly NE of the crater, implying a direction of impact towards the SW (red arrow). Image cropped from the MDIS Low Incidence-Angle mosaic.

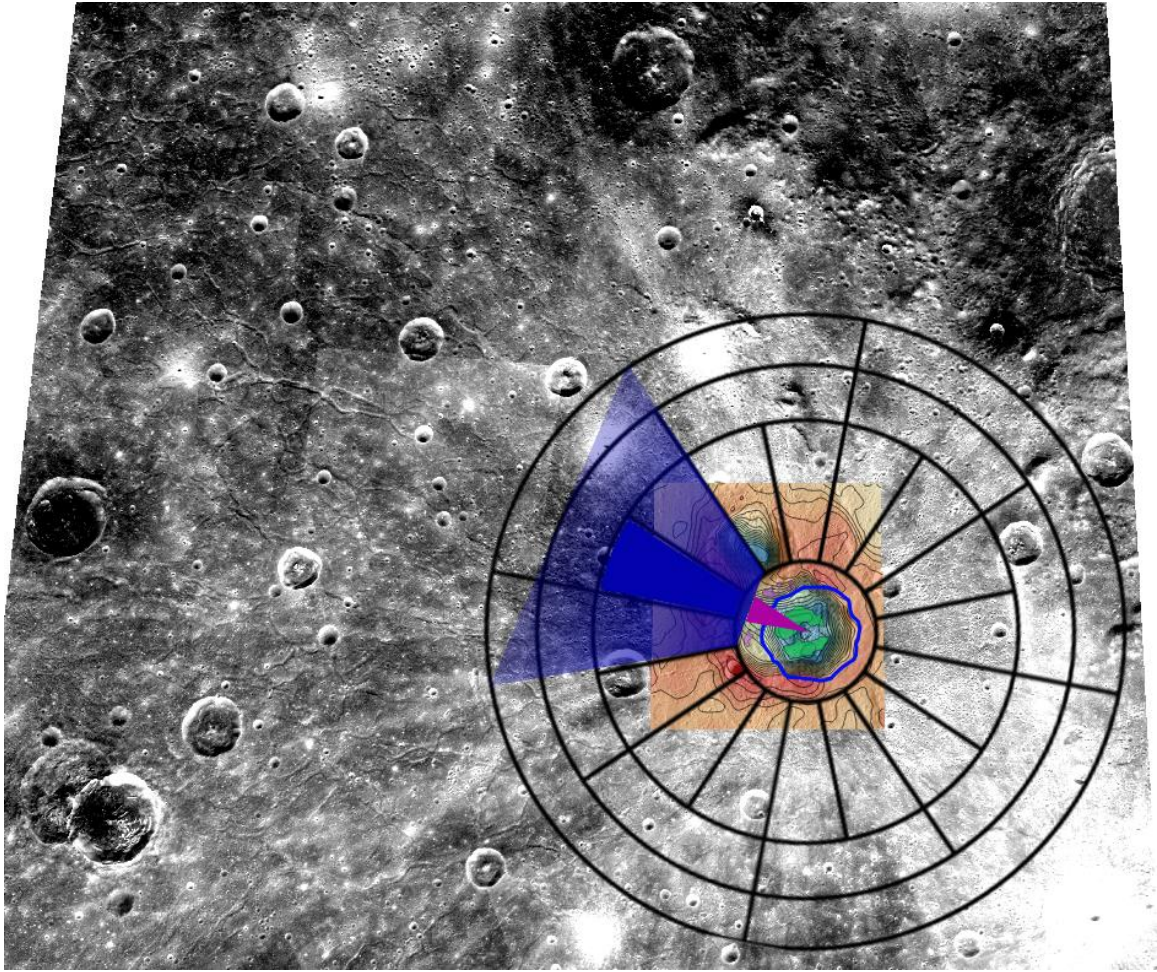


Figure 14: Low Incidence-Angle MDIS mosaic image of rayed crater Balanchine, underlying its MDIS mosaic and USGS DEM imagery, with forbidden zone highlighted on the sixteen-wedge grid in blue and impactor direction marked in solid blue in the middle of the forbidden zone. The impact-melt direction for Balanchine is also marked on the grid, in purple.

Chapter 3

3 Results

Twenty-four complex craters on Mercury with exterior deposits of impact melt were identified in this work. These craters lie primarily between 25° and 65°N latitude and have diameters primarily between 25 and 75 km, with a handful of notable exceptions. Around half of the 24 craters are rayed craters. The smallest crater in the catalog is Ailey crater with an average diameter of 23.7 km, while the largest is Eminescu with an average diameter of 152 km.

Applying the complex-crater classification scheme from Herrick (2018), to the catalog, the majority of the craters (19 out of 24) can be classed “normal” complex craters possessing just a central peak, while the remaining five (Abedin, Eminescu, Hokusai, Seuss, and Stieglitz) exhibit what is termed a “ringed peak cluster” by Herrick (2018). These five craters are among the largest in the catalog, all about 100 km in diameter, and probably represent craters that should be peak-ring basins but, likely due to anomalous impactor size, velocity, or both, are not quite so.

Eight of the 24 craters are situated partially atop a notably older crater, and of these six are found to have notable exterior melt deposits within these adjacent craters. The catalog’s oldest crater is probably Stieglitz, whose lightly-cratered floor and exterior melt deposit, as well as no visible ejecta blanket of any kind, imply it to be Calorian in age (1.7-3.7 Ga) (Barlow and Banks, 2018). Seven craters lacking ray ejecta still maintain the steep walls and fresh-looking crater floors. These are likely to be Mansurian in age (0.28-1.7 Ga) (Barlow and Banks, 2018). The remaining craters are likely Kuiperian in age (<0.28 Ga).

3.1 The Final Crater Catalog

A final catalog of Mercurian complex craters bearing exterior melt deposits was created using an Excel spreadsheet. In this spreadsheet, crater name, diameter, latitude and longitude, crater rim elevation, crater depth, implied impactor direction (for those craters

possessing asymmetric ejecta blankets), RCL location, and direction of maximum melt deposition were obtained as described in Chapter 2.

Table 1, below, lists these results for each crater in our catalog. The craters filling the bottom-most slots are as-yet unnamed. We gave these craters provisional names, given in Tables 1 to 3 in quotations. From these data, we calculate the remaining values, namely the ratio R , the separation between RCL and melts, and the diameters and depths of these craters. We describe these calculations in detail in Section 3.2.

Briefly, we shall describe several of the outlier values present in our data set.

Firstly, a handful of craters in this catalog lie below the MLA threshold latitude of 25°N where data is relatively sparse due to MESSENGER's elliptical orbit. These craters are kept nevertheless because their location on Mercury was such that MLA data was still present, albeit fairly scant, in those areas. Most of the craters lying below this threshold also happen to have diameters larger than 50 km, which helped ensure more than one traverse line of MLA data existed for these craters. It also allowed for the use of the lower resolution USGS DEM map in determining crater depth and rim elevation.

Secondly, we wish to compare the craters Abedin (Figure 15) and Hokusai (Figure 16). They both appear to possess a fairly uniform rim, with little rim crest variation, and both possess more than one melt-pond location though the largest of them is used in our analyses in each case. Kinczyk et al. (2018b) compared and contrasted these two craters, and found that both craters may have been formed from large, slow impactors. The lack of melt ponds at Hokusai compared to those at Abedin can be explained by much of Hokusai's ejected melt being incorporated into the ejecta blanket and, in places, creating the observed rampart-like structures there.

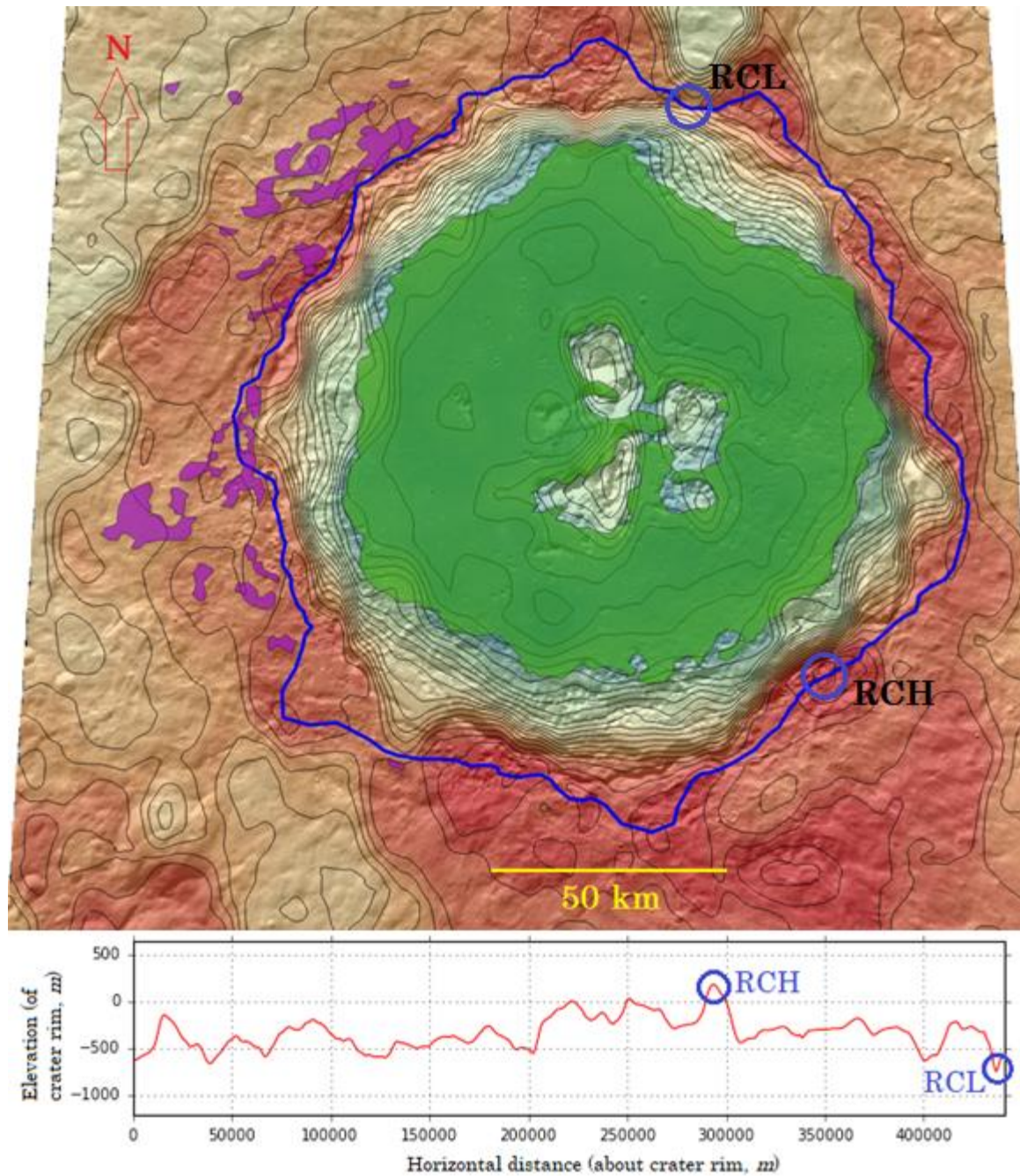


Figure 15: Abedin crater. MDIS mosaic with USGS DEM overlay, processed in QGIS. Rim shown in blue, crater floor in green, melts in violet, and contour lines (black) have a 300 m interval. A topographic profile of Abedin's rim reveals the RCL (highlighted by blue circle) to be north of the crater, towards a nearby crater.

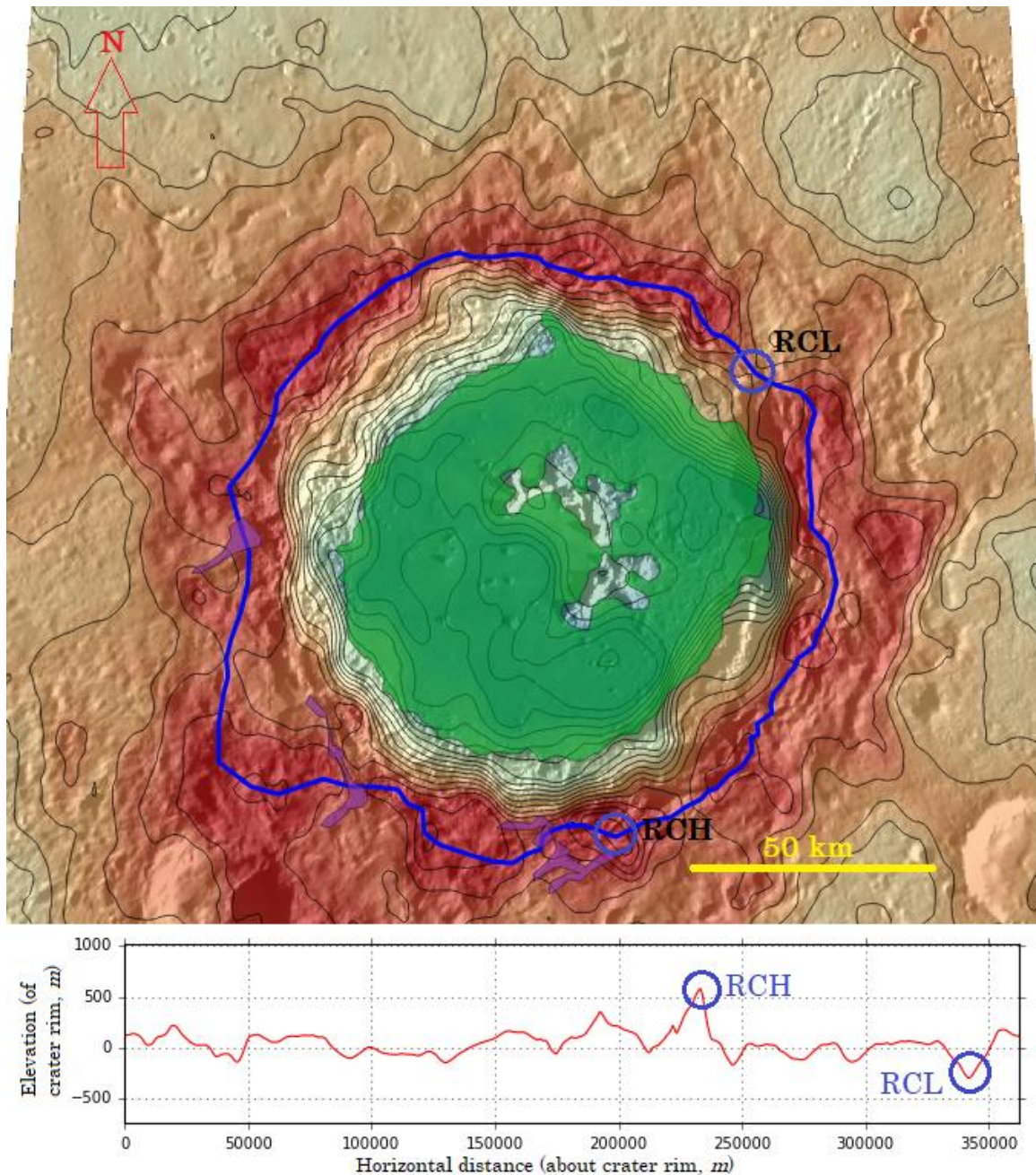


Figure 16: Hokusai crater. MDIS mosaic with USGS DEM overlay, processed in QGIS. Rim shown in blue, crater floor in green, melts in violet, and contour lines (black) have a 300 m interval. A topographic profile of Hokusai's rim reveals the RCL (highlighted by blue circle) resides to the NE of the crater. Note also the rampart feature characteristic of this crater, enhanced by the highlighted contour lines. As with the melts, these ramparts appear to cluster more on the south and west sides of the crater.

Crater diameter, as detailed in Chapter 2, has resulted in notably larger diameter values for the two dozen craters in our catalog than has commonly been cited in other studies of Mercurian craters. For example, our values for the craters in our catalog tend to be around 10% larger than the diameter values given in the Banks et al. (2017) catalog. Primarily, this is due to the way by which we drew the rim shapefiles with respect to the topography data as well as the MDIS mosaic and NAC imagery. Because the topography data implied crater rims slightly beyond the physical rim visible in the MDIS mosaic and NAC imagery, consequently our crater-diameter values are slightly larger. Applying the two-profile technique to just the visible crater rim in the MDIS mosaic and NAC imagery, the diameter values found in Banks et al. (2017) are replicated.

Our analysis of rayed craters showed only five craters with an obvious asymmetry in their ejecta distribution, and of these craters only Ailey crater appears to show a downrange trend in melt emplacement while Degas alone displays a $\sim 90^\circ$ separation between its forbidden zone and its melt deposit. However, Ailey's melt pond is located inside an adjacent, older crater, so the direction may be related to pre-impact topography, and its ejecta distribution may be of the "butterfly" type, so our interpretation of impactor direction may be incorrect. The other three craters, Balanchine, Bek, and Fonteyn, show the opposite trend, with the melt deposits located within the forbidden zone of the ejecta blanket. As shown in Table 1, these three craters do not fall under the same RCL-vs-melt regime ("coincide" for Balanchine, "within 90" for Bek, and "90 or greater" for Fonteyn) which in turn suggests pre-impact topography does not play a role here. Eminescu's ejecta blanket was present, but difficult to make out due to the abnormally high-albedo ejecta blanket of nearby crater Xiao Zhao.

As for the two craters whose impact direction was gleaned from other studies, both of them, Hokusai (from Ernst et al., 2016) and Stieglitz (from Hood et al., 2018), show a trend congruent with the one shown by Ailey. Because only three of the seven craters show the downrange trend that would imply impactor direction is a controlling factor, we therefore rule out impactor direction as a controlling factor for melt emplacement about Mercurian craters in general. Indeed, the three craters that show an uprange trend are equally intriguing as no known mechanism for this trend has yet been proposed. Crater

Degas is the only crater of the seven whose implied impact direction lies $\sim 90^\circ$ to its melt deposits.

Lastly, five of the seven craters in this catalog whose RCL and Melts directions are the same are those that are found adjacent to an older impact crater (e.g., Balanchine crater; see Figure 14 in Chapter 2). We are confident the melt ponds in these adjacent craters originated from the fresher crater in question and are not melt on the floor of the older crater because these melt ponds are smoother, with far less clastic material in them, compared to the melt deposits comprising the floors of these craters (Leight and Ostrach, 2018). The older craters also lack ejecta blankets, and their walls are more degraded in appearance (Kinczyk et al., 2018a) compared to the fresher craters adjacent to them that possess more clean-cut, steep-faced walls (Kinczyk et al., 2018a).

3.2 Numerical Calculations

We then calculated the depth and rim crest variation for each crater. This is reported in Table 1, utilizing the equations given in Chapter 2.

Another important aspect being considered here is the degree of separation between the RCL and the melt-deposit directions. This relation is displayed as a plot of the percentage of complex impact craters falling under each of the following four “regimes”: “coincide” (RCL and melts have the same direction), “within 45” (Melts are within 45° of the RCL), “within 90” (Melts are found somewhere between 45° and 90° from the RCL), and “90 or greater” (Melts are located $\geq 90^\circ$ away from the RCL). There is no chirality to this regime, aside from which direction out from the RCL gives the smaller angle. For example, Kulthum has melt ponds of equal size both north and south of it but since its RCL is roughly halfway between them Kulthum will fall under “within 90” regardless. As another example, Abedin possesses melt ponds W and NW of it, while its RCL is NNE, so the smallest angles are $\sim 90^\circ$ for the NW deposit and $\sim >90^\circ$ for the W deposit; because the NW melt deposit is larger in size (Figure 15), Abedin crater will fall under the “within 90” regime.

Of the 24 craters comprising the final catalog, seven of them show the “coincide” regime, six show the “within 45” regime, five show the “within 90” regime, and the remaining six

show the “90 or greater” regime. This trend is illustrated in the next section, comparing our results for Mercury to the results obtained by Neish et al. (2017).

With the exception of Ailey, all Downrange craters have their RCLs situated on the other side of the crater to where their Melts are located. There is no discernable pattern to the uprange craters. There is also no obvious correlation between a crater’s R and its size, nor is there any obvious correlation between a crater’s R and the regime it falls under; “coincide” craters tend to possess higher R values, but “Dorion” and “Hemon” are notable exceptions to this and some of the highest- R craters, especially “Thomson,” do not fall under the “coincide” regime. The “within 45” regime of RCL vs melt is lacking in craters compared to the other three regimes, but otherwise the distribution here also has no notable correlations to it.

As an exercise, we also studied how comparing the second-lowest rim elevation of the cataloged craters to their primary melt deposits might alter our results (see Table 3 and Figure 19). If the second-lowest rim elevations are statistically indistinguishable from the lowest rim elevations, our results may be unfairly biased.

In our work, the second-lowest rim elevations for Mercury’s craters are comparable to the lowest rim elevations within the RMS error values in the USGS DEM. The average difference in elevation between the RCL and the second-lowest rim elevation is ~ 300 m, which is approximately the same as the vertical RMS error of ~ 296 m. With that in mind, we found that the second-lowest elevation point of the rims of these Mercurian craters, with respect to their primary melt deposits, gave a trend that appears to follow an inversion of the lunar trend shown in Neish et al. (2017). Thus, in both cases (RCL and second-lowest rim elevation) the Mercurian trend is seen to be distinct from the lunar trend. As we discuss in Chapter 4, this is suggestive of different emplacement mechanisms on the two worlds.

In a handful of cases, though, for example “Thomson” crater, the second-lowest rim elevation was likely the original RCL of the crater until a later event gave the target crater a newer RCL. In the case of “Thomson,” an impact crater formed adjacent to “Thomson” itself sometime after it had fully formed.

Performing the same exercise for the Venusian and lunar craters in Neish et al. (2017), and comparing the results to those of this study, may prove to be quite helpful in determining the most likely mechanism responsible for melt emplacement on those worlds.

A similar exercise using the third-lowest rim elevation values for the cataloged Mercurian craters was attempted but ultimately discarded as too many craters lacked obvious third-lowest rim elevation values to make such an analysis statistically worthwhile.

3.3 Comparison of Results to Prior Work

Figure 17 is a visualization of RCL vs melt emplacement for Mercury compared to the Moon and Venus. The data for the Moon and Venus comes from Neish et al. (2017), and data for Mercury comes from this work. Qualitatively, Figure 17 suggests that Mercury's population follows more closely the trend for Venusian craters than for lunar craters.

Might topographic variation play a role in this pattern shown by Mercury's craters?

Figure 18, below, is a plot of R , which models topographic variation for the craters in question, against the RCL-vs-melt trend shown above. As before, the data for the Moon and Venus comes from Neish et al. (2017). The original data from Neish et al. (2017) contains a greater spread of RCL-vs-melt angles for this given type of plot, but here, to keep consistent with the regimes used for the RCL vs Melts plot, only those four distinct regimes are used.

To investigate the hypothesis that the Mercury craters follow the same distribution as either the Venus or lunar craters, we applied the Anderson-Darling goodness-of-fit technique. This technique (Equation 3) evaluates the statistic A^2 , which quantifies the difference between the cumulative probability function for the observed Mercury ratios, $F_n(R)$, and the cumulative probability function for either the lunar or Venusian ratios, $F(R)$:

$$A^2 = n \int [(F_n(R) - F(R))^2 / (F(R)(1 - F(R)))] dR \quad \text{Equation 3}$$

The greater the difference between the data and model probability distribution, the larger A^2 becomes, increasing the probability of observing a given A^2 value by chance. In the

case where the model $F(R)$ has no free parameters to adjust, the probability, $p = 1 - P(A^2 < z)$, of observing a particular A^2 value can be obtained from standard tables (Lewis, 1961). A high p value indicates that the observed result is likely if the null hypothesis being tested is true, whereas a low p value indicates a significant contradiction to the null hypothesis. We used this technique to determine whether the ratios of the Mercury craters were drawn at random from the distribution function for the Venusian or lunar ratios (the null hypothesis). If we consider the multivariate situation, taking into account both the separation angle and the ratio R , the p values are $p = 0.41$ for Venus and $p = 0.00046$ for the Moon. Thus, the hypothesis that the Mercury ratios were drawn at random from the lunar ratios can be rejected with confidence. However, we cannot reject the hypothesis that the Mercury ratios were drawn at random from the Venusian ratios. Mercury and Venus therefore appear to represent a different population from the data from the Moon, possibly produced through two separate processes.

In comparison to the Moon and Venus, the uncertainty values for those two worlds are comparable to the errors obtained for the Mercurian craters (Figure 18). Although the USGS DEM data has lower resolution than the MLA data, especially for Mercury's northern hemisphere, the USGS DEM dataset was still able to give uncertainties that were small enough for comparison of Mercury's catalog to those of the Moon and Venus (see Section 4.2).

In Chapter 4, we will discuss, at length, the various ramifications of all these findings for Mercury as they relate to what has already been theorized in prior work done for the Moon and Venus. We then hypothesize what is to be expected for other rocky bodies, should they be studied in the future.

Table 1: The twenty-four Mercurian craters, and the pertinent data about each crater used in this study.

Name	D (km)	D-err. (km) ^c	Lat.	Long.	RCL loc. ^a	Melt loc. ^a	Rays ^a	RCL vs melt ^b	Melt vs rays ^b	RCH (m) ^a	RCL (m) ^a	err. (m) ^c
Abedin	131	17.4	61.6°N	349.5°E	NNE	NW; W	no (?)	90	---	185	-744	296
Ailey	23.7	0.62	45.9°N	178.1°E	NW	NW	SE (?)	0	downrange	398	-947	296
Apolodorus	49	8.93	30.5°N	165.2°E	N	SSE	sym.	180	---	141	-459	296
Balanchine	41.1	0.39	38.8°N	175.5°E	WNW	WNW	NW	0	uprange	1770	-351	296
Bek	33	2.05	21.2°N	309.3°E	ENE	N	N	90	uprange	312	-441	296
Cunningham	36.8	1.53	30.4°N	157.1°E	W	NW	sym.	45	---	42.3	-913	296
Degas	62.1	5.81	36.8°N	233.0°E	SSW	S	WNW	180	perpendicular	1300	190	296
Eminescu	152	0.39	11.3°N	113.1°E	WNW	S	sym. (?)	180	---	1620	45.8	296
Erte	62.5	9.15	27.8°N	243.3°E	NNE	NNE	faded	0	---	1430	301	296
Fonteyn	31	4.85	32.7°N	95.6°E	SW	N	NW	180	uprange	-135	-726	296
Hokusai	99.2	0.85	57.8°N	17.1°E	NE	S; SW; W	ENE*	180	downrange	581	-296	296
Kulthum	41.2	6.27	50.8°N	94.1°E	SSW	S	faded	45	---	-623	-1160	296
Kyosai	47.4	3.49	25.4°N	5.2°E	NE	NE	no	0	---	2290	627	296
Plath	42.7	1.94	37.6°N	321.1°E	SSW	S	faded	45	---	602	-292	296
Seuss	76.9	0.96	7.6°N	33.8°E	S	SSE	faded	45	---	358	-336	296
Stieglitz	97.9	5.91	72.3°N	68.3°E	ESE	N	SSE**	90	downrange	107	-804	296
Tyagaraja	108	3.16	4.4°N	212.6°E	S	ESE	no	90	---	2640	270	296
"Thomson"	37.2	0.26	64.6°N	255.2°E	NNE	E	faded	180	---	2240	-410	296
"Carr"	24.3	1.04	64.9°N	254.7°E	WNW	ESE	no	180	---	1030	304	296
"Lightfoot"	41.8	0.93	49.2°N	252.4°E	NE	NNE	faded	45	---	-124	-2100	296
"Dorion"	46.9	2.29	48.9°N	259.1°E	N	N	no	0	---	-478	-1620	296
"Phidias"	37.3	1.83	34.7°N	7.2°E	WNW	N	no	90	---	122	-789	296
"Hemon"	43.9	3.2	36.9°N	301.6°E	SW	SW	no	0	---	195	-454	296
"Bennington"	66.3	4.79	5.5°N	242.5°E	SE	SE	no	0	---	1130	7.96	296

*Impactor direction implied from Ernst et al. (2016) data.

**Impactor direction implied from Hood et al. (2018) data.

^aRCH and RCL are defined in Section 2.3; "RCL loc." is the cardinal direction of the RCL; "Melt loc." is the cardinal direction largest melt deposit (smaller deposits separated by ";").

^b"RCL vs melt" relates RCL direction to melt-deposit location, where "0" = "coincide," "45" = "within 45°," "90" = "within 90°," and "180" = "90° or greater"; "Melt vs rays" relates implied impact direction to melt-deposit location, where "downrange" = impact direction opposite to melt location, "uprange" = melt location coincident with impact direction, and "perpendicular" = melt located ~90° to impact direction.

^cUncertainties associated with crater diameter ("D-err.") and RCH/RCL ("err." – from Becker, personal communication).

Table 2: Latitude and Longitude values used to crop out each crater in this study, plus errors associated with the data.

Name	rim-diff.^a	rim-err.^c	avg.rim^b	std.rim^b	avg.floor^b	std.floor^b	Depth (d)^a	d-err.^c	R^b	R-err.^c
Abedin	928	419	-331	169	-5240	361	4910	398	0.19	0.09
Ailey	1350	419	-133	417	-2540	401	2410	578	0.56	0.22
Apollodorus	600	419	-151	160	-3750	423	3600	452	0.17	0.12
Balanchine	2120	419	860	625	-1450	133	2310	638	0.92	0.31
Bek	753	419	-185	209	-2200	384	2010	437	0.37	0.22
Cunningham	955	419	-440	290	-2670	214	2230	361	0.43	0.2
Degas	1110	419	655	332	-2010	433	2660	546	0.42	0.18
Eminescu	1580	419	1050	431	-922	1010	1970	1100	0.8	0.49
Erte	1130	419	881	300	-681	331	1560	447	0.72	0.34
Fonteyn	591	419	-380	142	-3670	339	3290	367	0.18	0.13
Hokusai	877	419	41.7	124	-3350	529	3390	544	0.26	0.13
Kulthum	541	419	-904	136	-4430	375	3530	399	0.15	0.12
Kyosai	1660	419	1600	567	-582	263	2180	625	0.76	0.29
Plath	894	419	137	254	-1900	272	2040	372	0.44	0.22
Seuss	694	419	-30.2	161	-4150	252	4120	299	0.17	0.1
Stieglitz	911	419	-284	219	-4730	268	4440	346	0.21	0.1
Tyagaraja	2370	419	961	654	-2600	280	3560	711	0.67	0.18
"Thomson"	2650	419	703	791	-1270	282	1970	840	1.35	0.61
"Carr"	722	419	723	222	-711	346	1430	411	0.5	0.33
"Lightfoot"	1980	419	-736	565	-4070	608	3340	830	0.59	0.19
"Dorion"	1140	419	-1020	396	-4330	608	3310	725	0.35	0.15
"Phidias"	911	419	-490	197	-3810	174	3320	263	0.27	0.13
"Hemon"	649	419	-165	161	-3080	247	2910	295	0.22	0.15
"Bennington"	1130	419	706	262	-1090	613	1800	666	0.63	0.33

^a"rim-diff." = RCH – RCL is the maximum variation in rim topography of the crater in meters; all crater depth values in meters.

^bThese values (in meters) are noted and described in Section 2.3, and are used according to Equations 1a-2b.

^cUncertainties associated with "rim-diff." ("rim-err." = $\sqrt{2(\text{"err"})^2}$], in meters), "d-err." (described by Equation 2b, in meters), and "R-err." (described by Equation 1b).

Table 3: A qualitative comparison of rim-low vs melt-deposit directions for the lowest (RCL) and second-lowest rim elevations for each crater (see Figure 19 below), as well as other remarks specific to these craters.

Name	RCL-1 ^a	RCL1 vs melt ^a	RCL-2 ^b	RCL2 vs melt ^b	remarks...
Abedin	NNE	90	NE	90	Little variation in rim topography; crater large enough not to need MDIS-NAC imagery
Ailey	NW	0	SSW	180	Melt in adjacent crater; may possess butterfly rays
Apollodorus	N	180	E	90	Associated with radially-fractured terrain that is fairly symmetric about the crater
Balanchine	WNW	0	N?	90	Melt in adjacent crater
Bek	ENE	90	NW	45	Forbidden zone just visible N of crater
Cunningham	W	45	S	180	Very small, but clustered, melt deposits; neighbours Apollodorus
Degas	SSW	45	WNW	180	Sliver-like forbidden zone N of crater
Eminescu	WNW	180	NNE	180	Rays are overshadowed by nearby crater Xiao Zhao; crater large enough not to need MDIS-NAC imagery
Erte	NNE	0	S	180	Melt in adjacent crater
Fonteyn	SW	180	W	90	Very small, but clustered, melt deposits
Hokusai	NE	180	WSW	90	Little variation in rim topography; three small melt ponds (one larger than the others)
Kulthum	SSW	45	N	180	Rays appear faded, cannot tell if asymmetric
Kyosai	NE	0	SSE	180	Melt in adjacent crater
Plath	SSW	45	N	180	Rays appear faded, cannot tell if asymmetric
Seuss	S	45	N	180	MDIS-NAC imagery available but does not render properly in QGIS
Stieglitz	ESE	90	NW	45	Oldest melt-bearing crater in catalog
Tyagaraja	S	90	ESE	0	No high-resolution MDIS-NAC imagery available for this crater; crater large enough not to need MDIS-NAC imagery
"Thomson"	NNE	180	NE	45	Abnormally large melt volumes, mostly found inside an adjacent basin
"Carr"	WNW	180	NE	90	Smallest crater in catalog; neighbours "Tom Thomson"; MDIS-NAC imagery available but does not render properly in QGIS
"Lightfoot"	NE	45	SSE	180	Rays appear faded, cannot tell if asymmetric
"Dorion"	N	0	ESE	180	Melt in adjacent crater; no MDIS-NAC of melt ponds but are still relatively notable
"Phidias"	WNW	90	N	0	Too few MDIS-NAC imagery available for this crater to make out all its melt deposits
"Hemon"	SW	0	S	45	No MDIS-NAC imagery available for this crater
"Bennington"	SE	0	NE	90	Melt in adjacent crater

^a"RCL-1" = "RCL loc." from Table 1, and "RCL1 vs melt" = "RCL vs melt" from Table 1.

^b"RCL-2" = cardinal direction of the second-lowest elevation point on the crater rim, and "RCL2 vs melt" = RCL-2 direction compared to melt direction.

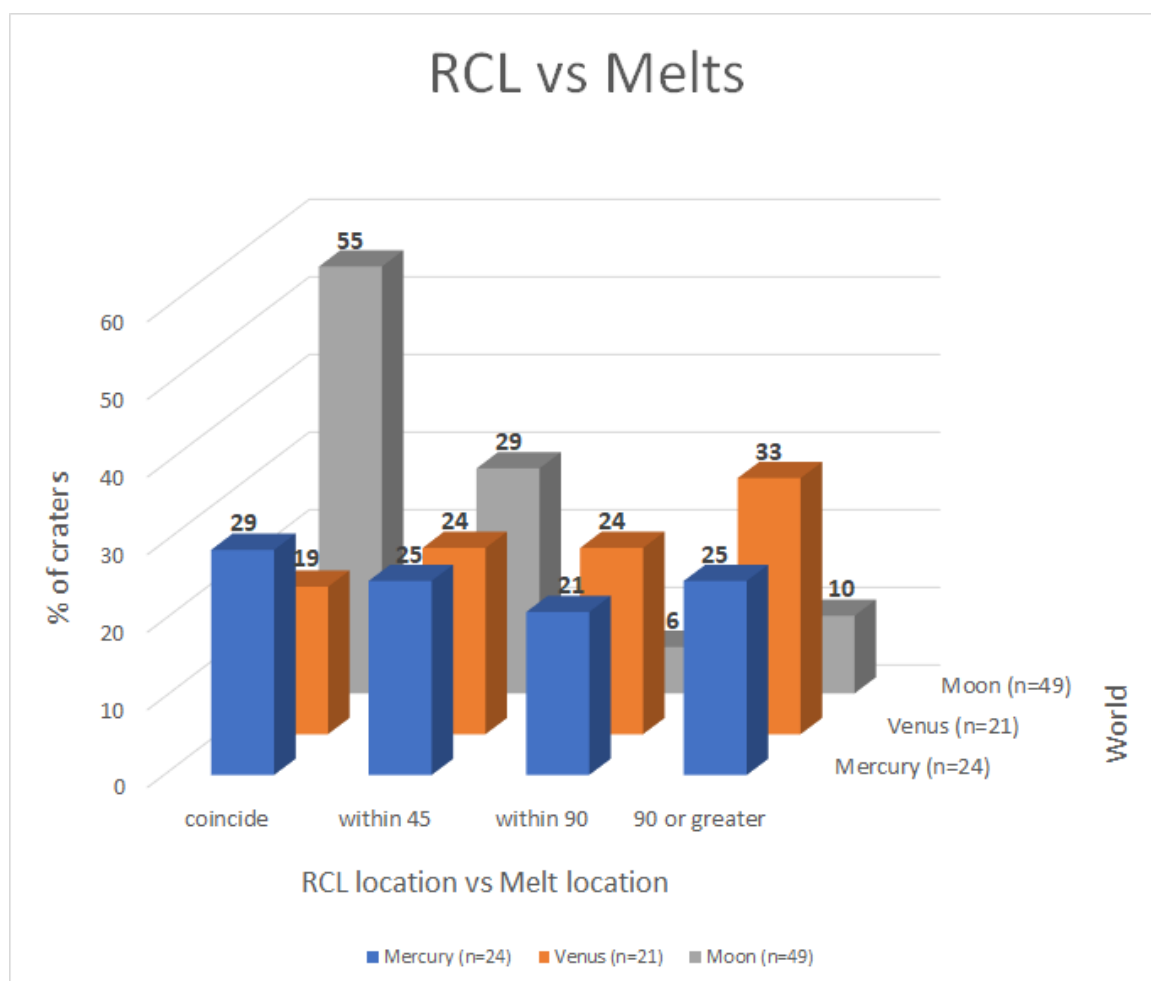


Figure 17: Melt location with respect to RCL location for Mercurian, Venusian, and lunar complex craters. Lunar craters show a notable spike in values at and near the “coincide” regime, that is not present as such on Venus and Mercury. For Venus, there is a slight trend towards the “90 or greater” regime but otherwise is fairly even across the regimes. Qualitatively, Mercury’s craters seem to follow a trend that is more similar to the Venusian trend than the lunar trend. Data for the Moon and Venus from Neish et al. (2017).

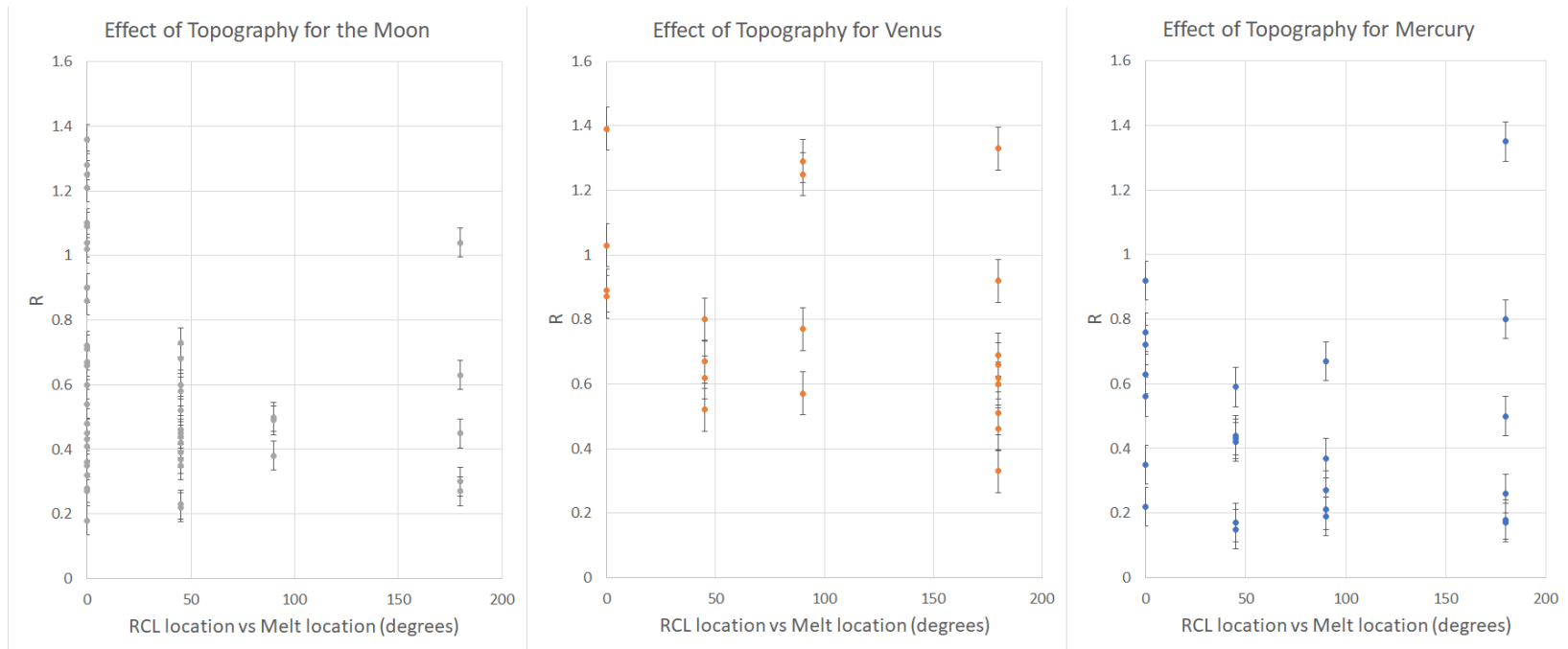


Figure 18: Comparison of the ratio R for Mercury, the Moon, and Venus shows that Mercury's craters follow the Venusian trend more closely than the lunar trend. Lunar and Venusian crater data from Neish et al. (2017).

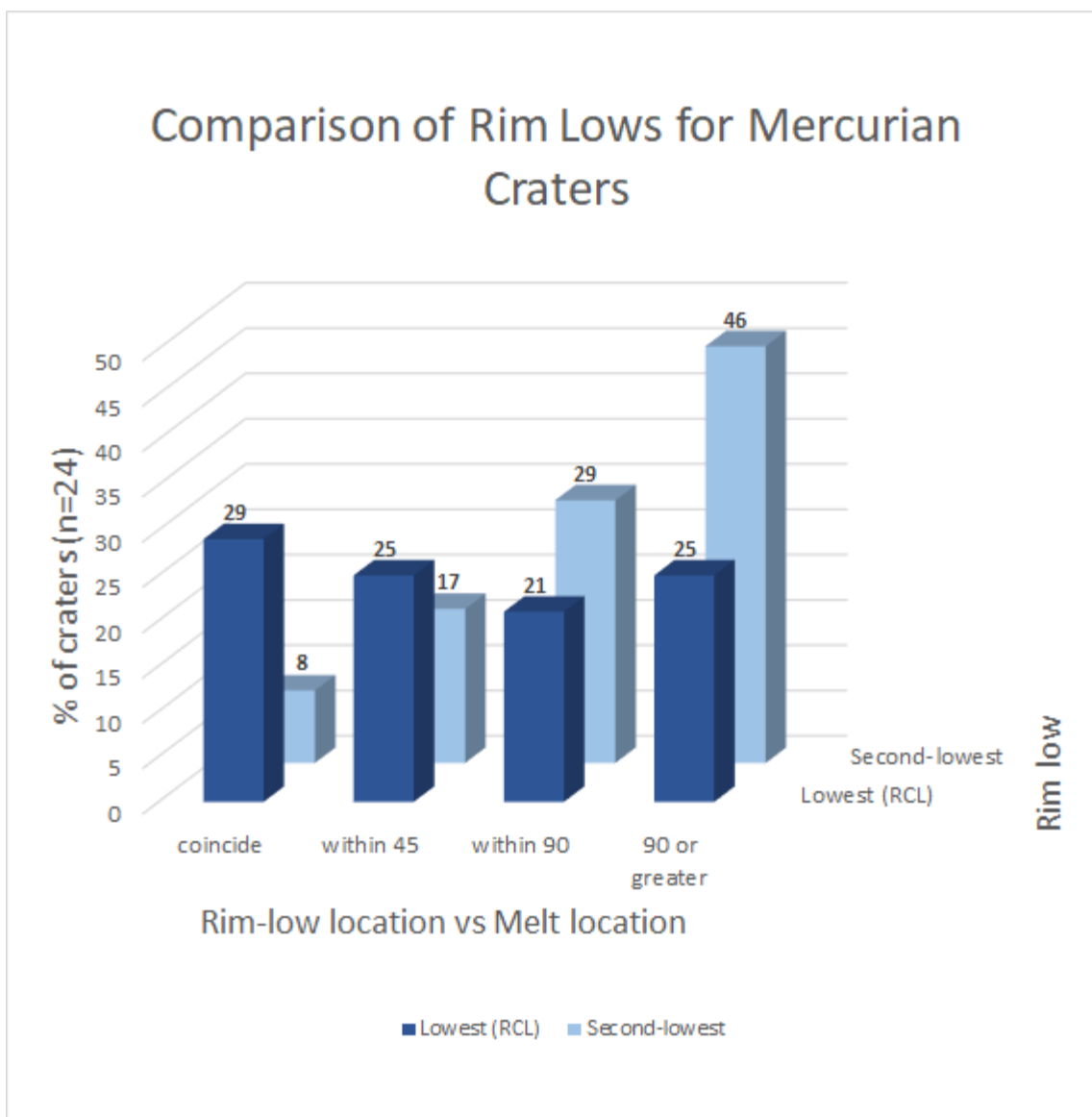


Figure 19: Rim-low vs melt-location for complex craters of the planet Mercury, comparing RCL vs melt location and the second-lowest rim elevation vs melt location for the catalog of 24 craters studied in this work. Note that the “second-lowest” plot trends as an inversion to the normal lunar trend seen in Neish et al. (2017).

Chapter 4

4 Discussion

The implications for the results of this work go beyond our understanding of the planet Mercury. Future work for the other rocky bodies in the Solar System is needed to substantiate these results. We suggest several avenues for future work here.

In addition, our results were not without limitations inherent to the MESSENGER mission and the data it collected (namely, the lack of altimetry data for Mercury's southern hemisphere due to MESSENGER's orbit around the planet). Here, we will place these limitations in the context of what amendments, likely via the BepiColombo mission, would help improve upon our results in any future work.

4.1 Where Does Mercury Fit?

Our results show that Mercury appears to lie more closely to the emplacement pattern found on Venus than the emplacement pattern observed on the Moon. This suggests that planetary surface gravity and/or impactor velocity is an important factor in determining the pattern of impact-melt emplacement about complex craters on any given rocky body.

The Moon is a notable example of the emplacement paradigm expected of sufficiently low-gravity worlds, as seen in Figures 17 and 18. While surface gravity and magnitude of the impact event are the primary controls on melt volume, impactor velocity also plays a role in impact-melt production irrespective of surface gravity (Melosh, 1989; Grieve et al., 1977; Osinski and Pierazzo, 2013). On the Moon, slower impactor velocities mean lesser crater modification during crater formation and therefore deeper craters with smaller melt volumes, relative to the size of the crater, compared to higher-gravity worlds and/or higher impactor velocities (Grieve and Cintala, 1997; Osinski and Pierazzo, 2013; Neish et al., 2017). Therefore, what melt is created during lunar impact-cratering events requires more momentum imparted into the melt to be thrust over the crater's rim (Hawke and Head, 1977; Osinski et al., 2011; Neish et al., 2017); this means that, normally, there is only enough momentum imparted into the melt during excavation to eject the melt completely over the crater's RCL.

Lunar impact events that occur on the Highland regions are observed to produce more melt material than craters forming on the Mare regions of the Moon (Neish et al., 2014; Stopar et al., 2014), which means there should be a better chance of finding lunar craters showing a non-coinciding trend of melt emplacement in the Highlands than the Mare. This difference in melt volume could be the result of differences in the rocks comprising the Highlands versus the Mare, namely the enhanced porosity of Highlands terrain (Wünnemann et al., 2008).

Thus, differences in melt volumes seen at the various craters in our catalog may be due to the compositional and physical differences between the host rock upon which each crater formed. Future work looking into the terrain in which each of our Mercurian craters formed may be of value in confirming or denying that hypothesis.

Venus, on the other hand, is a notable example of the emplacement pattern expected of sufficiently high-gravity, high impactor-velocity worlds, again as seen in Figures 17 and 18. Venus' higher surface gravity and proximity to the Sun promote higher impactor velocities, leading to increased melt production. The higher gravity also promotes the formation of craters subject to greater extents of crater rim and floor modification and collapse resulting in comparatively shallower craters. Venus' high surface and atmospheric temperatures also aid in the production of larger volumes of melt by making it easier for more melt to be produced during impact events (Chadwick and Schaber, 1993; Grieve and Cintala, 1997), which allows for more melt to be ejected from Venusian crater rims.

Mercury, meanwhile, shows an emplacement pattern most similar to Venus, suggesting higher gravity and/or impactor velocity produces sufficient melt to be easily pushed up and over the comparatively lower crater rims during excavation. Statistically comparing the Mercury-vs-Moon $p = 0.00046$ from this study to the Venus-vs-Moon $p = 0.08$ from Neish et al. (2017), it could even be argued that Mercury is a better example of high surface-gravity, or impactor velocity, influence than Venus. This is especially intriguing given that Mercury's surface gravity lies in between those of the Moon and Venus. This result might be an artifact produced by the Sun, as discussed below.

For Mercury, crater diameter and depth did not correlate with whether each crater was more affected by impact direction or by surface topography. There was no clear correlation between the uprange and downrange direction of the melt and whether the crater fell under the “coincide” or the “90 or greater” regime, especially when the one “perpendicular” instance is taken into account. There also appears to be no notable geographic correlation for this Venus-like relation on Mercury. However, there simply were not enough craters in our catalog to allow for any conclusions to be made with any certainty.

Impactor velocity is one likely mechanism that influences melt emplacement on terrestrial planets, based on how our results trend so similarly to the planet Venus. Venus has average impactor velocities of ~ 25 km/s (Tauber and Kirk, 1976) compared to Mercury’s average impactor velocities of ~ 40 km/s (Marchi et al., 2009); these are both higher than those for the Moon, at ~ 15 km/s (Marchi et al., 2009). However, surface gravity may also play a role in impact-melt emplacement due to its influence on crater depth.

Because impactor velocities are known to be abnormally high for Mercury, due primarily to the Sun’s gravitational influence on the impactors that strike Mercury’s surface (Schultz, 1988; Silber et al., 2017), a comparison of our results with a future study for Mars is therefore necessary. Although it has the same gravity as Mercury, the projectiles that impact Mars’ surface (Lefeuvre and Wieczorek, 2008; Silber et al., 2017) have mean impactor velocities of 9.6 km/s (Ivanov, 2001), roughly four times smaller than mean impactor velocities for Mercury, ~ 40 km/s (Marchi et al., 2009). Therefore, studying Mars’ fresh, melt-bearing, complex craters may help pin-point the surface-gravity and/or impactor-velocity threshold that should exist between the paradigm exemplified by the Moon and the paradigm exemplified by Mercury and Venus. Figure 20 illustrates our current working explanation, as a “tweak” upon that which was offered in Neish et al. (2017).

A look into how great an effect the Sun wields over impactor velocities on the various rocky bodies in the Solar System is pertinent to this study. Adushkin and Nemchinov (2008) note that impactor velocities for long-period comets striking the Earth are

generally noticeably higher (roughly 20-50 km/s) than the velocities exhibited by most asteroids (roughly 15-20 km/s) that also strike the Earth. This discrepancy is likely due to the fact that the comets are traveling to Earth from further away from the Sun than the asteroids are. A longer time spent being accelerated by the Sun's gravity well should then mean higher average velocities obtained by the time the comet crosses Earth's orbit. However, the gravity of the impacted body also plays a role in accelerating the impactor and thus impactor velocities are a function of both distance from the Sun and surface gravity.

We summarize the impactor velocities for the terrestrial planets below. Marchi et al. (2009) compares the impactor velocities for the Moon and for Mercury, illustrating their findings in Figure 11 of their paper. From that figure, average impactor velocities for the Moon are ~15 km/s whereas for Mercury average impactor velocities are ~40 km/s. By comparison, work by Ivanov (2001) has found a mean impactor velocity value for Mars of 9.6 km/s (with an average of 16.1 km/s for the Moon, which is in line with the Marchi et al. (2009) findings). Finally, Venus' mean impactor velocities are comparable to, though still greater than, the Earth's at ~25 km/s (Tauber and Kirk, 1976). From this, it can be seen that impactor velocities seen by Inner Solar System planets decreases with distance from the Sun itself. This likely implies that the Sun's gravity affects impactor velocities seen by the terrestrial planets diminishes the further away the planet is from the Sun itself. The Sun's gravity affects impactor velocities on Mercury the most, while it appears the Sun's gravity has the smallest effect on impactor velocities on Mars.

However, this study, and prior work on the Moon and Venus, show that despite the Moon's impactor velocities approaching those for Venus, the Moon's crater-melt trend still appears to be of the lower-gravity/impactor-velocity variety while the Venusian trend is of the higher-gravity/impactor-velocity variety. This could be evidence that the planet's own surface gravity still plays an important role alongside impactor velocity, in that surface gravity controls the extent of crater modification which in turn controls how impact melt is emplaced. However, the Sun still exerts some degree of gravitational influence on impactors striking the terrestrial planets that is dependent on proximity to

the Sun itself. Mercury experiences the greatest solar influence, while Mars experiences the least.

In summary, if impactor velocities are the controlling factor in melt emplacement then we might expect Mars to trend more similarly to the Moon despite Mars' larger surface gravity compared to the Moon. If gravity (and its effect on crater depth) plays a larger role, the trends should be similar for both Mars and Mercury.

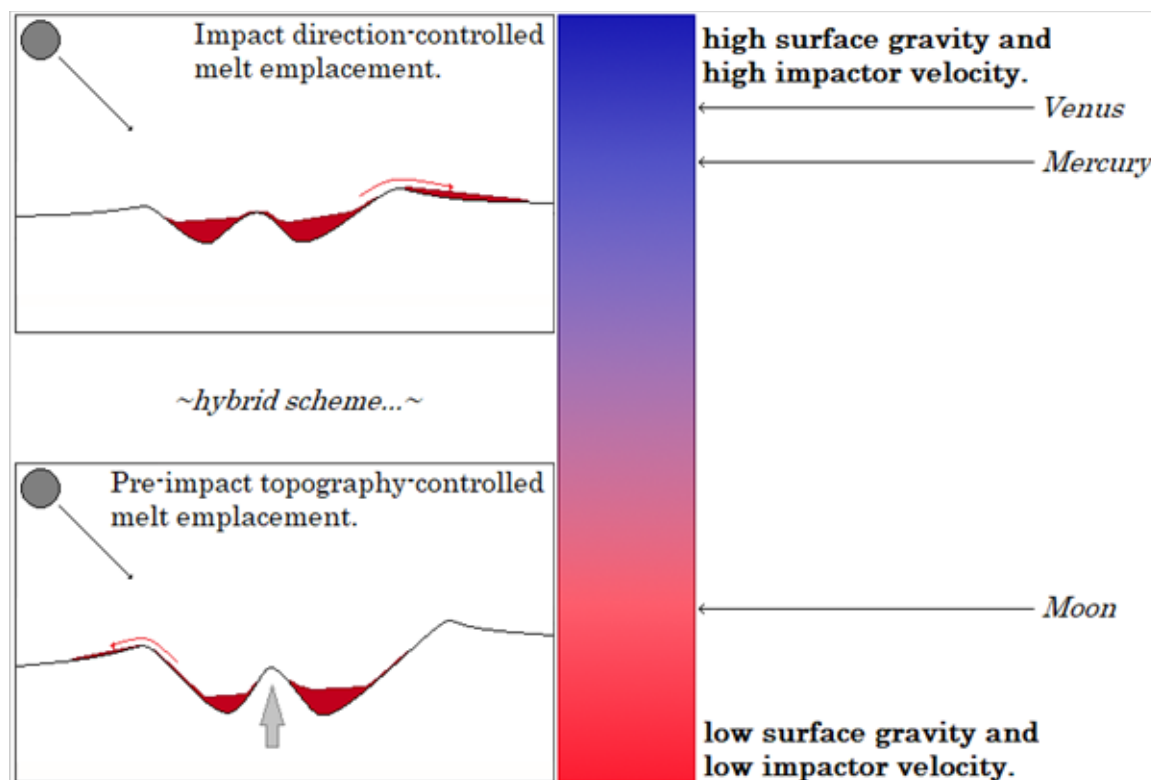


Figure 20: The two emplacement paradigms suggested by Neish et al. (2017) are sorted according to the results found in this study. Here, the paradigm found on Venus is the high impactor-velocity/surface-gravity end-member while the one found on the Moon is the low impactor-velocity/surface-gravity end-member. Mercury also falls within the high impactor-velocity/surface-gravity paradigm. These paradigms may be part of one, transitional paradigm, but more rocky worlds with differing surface gravity and impactor velocity values will be needed to test this hypothesis.

4.2 Limitations Due to MESSENGER Data

There are a couple very notable limitations inherent to the data used in this work, that have shaped, to some degree, the nature of this study.

First and foremost, the MESSENGER MLA data is confined only to Mercury's northern hemisphere and north of 45° in particular. This restricted the catalog of craters to the northern hemisphere alone. While there are craters in the southern hemisphere known to possess exterior melt deposits, notably Waters crater (Neish et al., 2013), because no topography data of high-enough precision exists for the southern hemisphere none of those craters could be used. There are examples of global topography available for Mercury, like the USGS DEM map used in this study in tandem with the MLA data. Another example is the recent work by Preusker et al. (2011, 2017a, 2017b, 2018) which have produced stereo topography maps of higher resolution, but these are, as yet, not freely available to the public. These two data sets were created using a similar procedure, using MDIS-WAC and -NAC imagery that overlap as a means to calculate elevation via trigonometry, though the maps created by Preusker and his team appear to have better resolution, at 222 m/pixel (Preusker et al., 2018), than the USGS DEM map, at 665 m/pixel. Once imagery from the BepiColombo mission is acquired, which should cover the southern as well as the northern hemisphere, and be of higher quality than was possible with MESSENGER, a re-analysis of the data collected in this study would be quite beneficial.

A number of DEMs were available to us, whose resolutions and associated accuracies are given by Zharkova et al. (2016) including the USGS and MLA DEMs used in our work and a number of Mariner 10 DEMs. They noted that the USGS DEM varied in elevation values by as much as 1 km due to the inherent noise in the instrumentation and in the data processing, while the MLA was as accurate as ~ 10 m for the same points of data. The notably more accurate MLA data was shown, and made useful, in this study via the more detailed contour lines the MLA data gave in QGIS compared to the USGS DEM as well as never being misaligned with respect to the MDIS imagery whereas the USGS DEM was often misaligned for the smaller craters lying close to Mercury's equator. Ideally, in

the future, a DEM of Mercury will exist that has high resolution, has global coverage, and has very small RMS errors and average elevation difference values.

Secondly, the MDIS imagery had its own limitation. The NAC imagery of sufficiently-high resolution to pick out the impact-generated melt deposits about the craters in our catalog was unreliably inconsistent. For the largest named craters in the catalog, high-resolution coverage was relatively complete. For the rest of the cataloged craters, it was common to have either low-resolution NAC imagery or very few images available leaving areas of the crater uncovered at high resolution. The MDIS mosaic has a resolution of 665 mpp, which is oftentimes too low a resolution to determine the location and shape of the melt deposits with any real confidence; therefore, these high-resolution NAC swatches were critical to identifying the melt deposits.

The BepiColombo mission should provide a far more comprehensive, high-resolution imagery dataset, covering the southern as well as the northern hemisphere of Mercury with high-resolution data. Mercury could certainly benefit from high-resolution imagery similar to what is available for Mars and the Moon.

4.3 Implications for Other Rocky Bodies in the Solar System

If surface gravity and impactor velocity do indeed control how impact melt is deposited about impact craters on rocky bodies, then the emplacement pattern given by the Moon, Mercury, and Venus should also hold for the other rocky worlds in the Solar System. Mercury and Mars have very similar surface gravities (but very different impactor velocities), so we wish to test if the emplacement pattern found on Mercury is also observed on Mars. Equally, Venus and the Earth have fairly similar surface gravities which implies the paradigm found on Venus may also hold for the Earth. Finally, the low-gravity Moon, with lower impactor velocities, should serve as a type-example for large rocky asteroids.

Because Earth and Mars, as well as Ceres and Vesta, also possess melt-bearing impact craters, future work studying those worlds in the manner applied here should prove very important in either confirming or denying what we have hypothesized based on the current, available evidence. However, despite the ease of access to Earth's craters for

researchers, the weathering and erosion that takes place on Earth can make it very difficult to determine the directions of the melt deposits and the RCL for those craters.

Mars suffers from a similar issue, though the rate of erosion on Mars is less than for the Earth. Figure 21, below, shows a good example of a fresh, complex, Martian crater with melt deposited just outside its rim.

As for Ceres and Vesta, while they are airless bodies, like the Moon they may not produce much impact melt due to their relatively small size and low impactor velocities. Figure 22 shows an example of melt-bearing Ikapati crater on Ceres, which appears to be an exception to the above by possessing an exterior melt deposit that appears to be quite large. The reason for this has yet to be determined. Figure 23 gives an example of melt-bearing Marcia crater on Vesta, possessing the expected, small-sized melt deposits about it. The primary set-back expected in studying Ceres and Vesta is that each of these two bodies may not possess enough melt-bearing craters to be statistically viable.

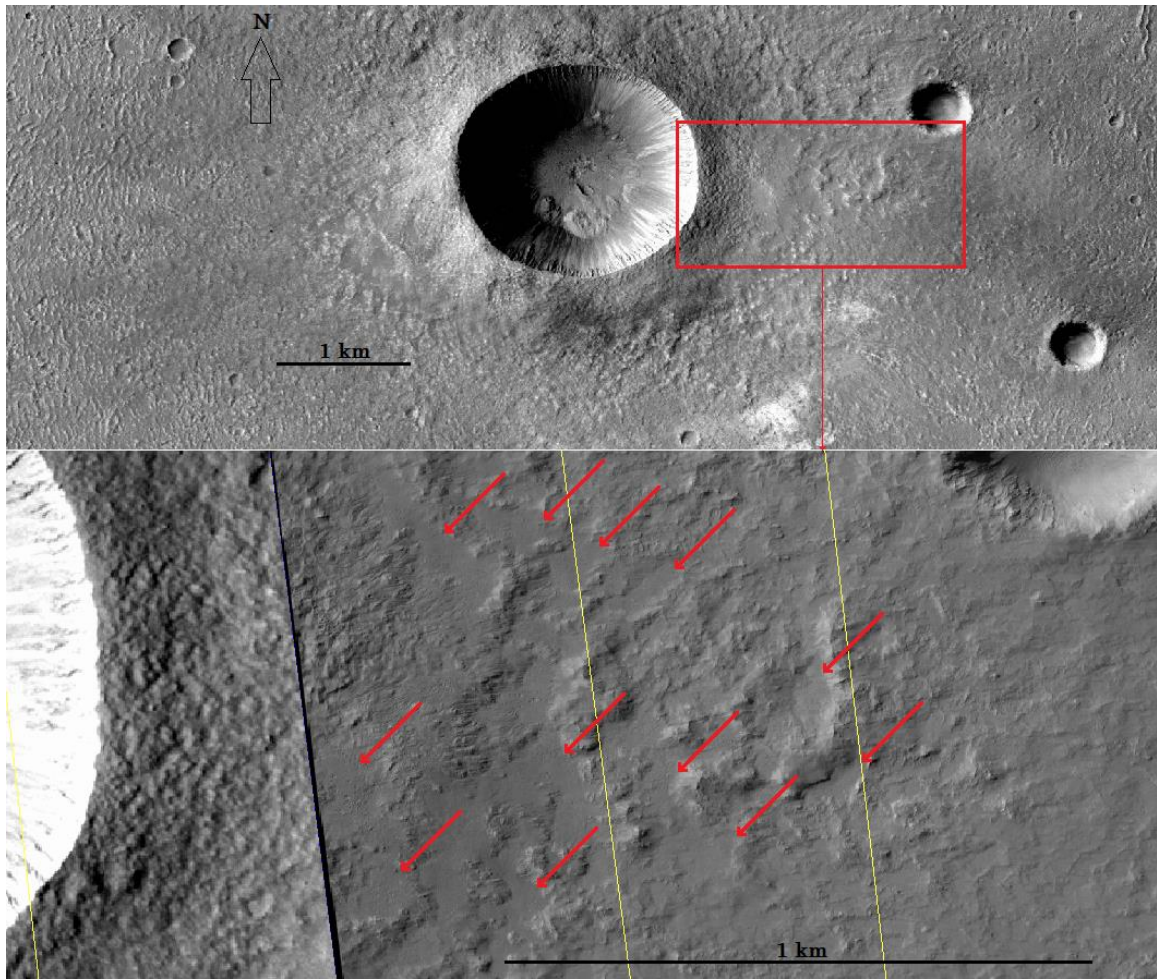


Figure 21: Top = image of CTX overlay (Stamp B12_014262_1513_XN_28S113W) of Zumba crater on Mars, rendered in JMARS, with its more obvious exterior melt deposit highlighted by the red rectangle (see Tornabene et al., 2012). Bottom = inset shown in red rectangle, also rendered in JMARS, where the CTX image is overlain by a HiRISE image (Stamp ESP_017229_1510_RED); melt ponds highlighted by red arrows.

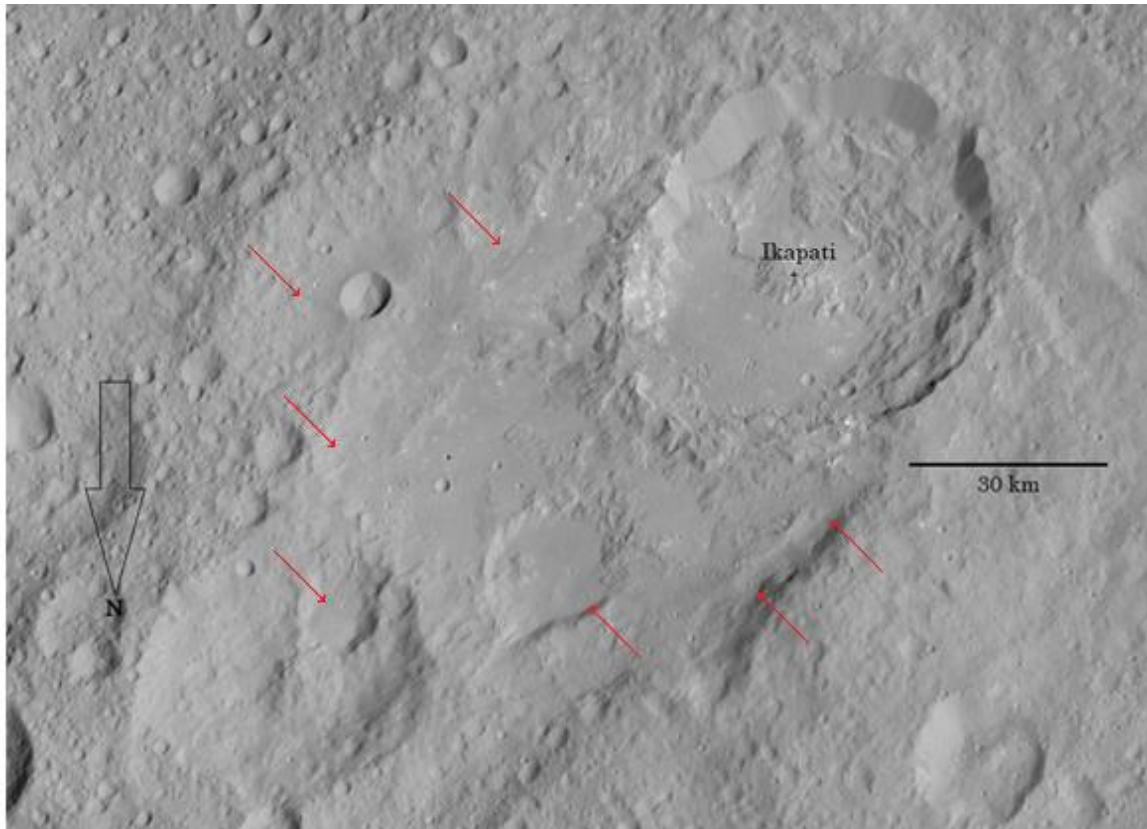


Figure 22: Ikapati crater (HAMO image FC21A0042388_15249065450F1F; from 2015248_C2_ORBIT068, 20150829_CYCLE2, DWNCHFC2_1A, Dawn Ceres FC2 raw HAMO, sbn.psi.edu/pds/resource/dawn/dwncfcL1.html), on the dwarf planet Ceres. The ejected melt (marked by red arrows) appears to have been emplaced within an adjacent, older-looking crater.

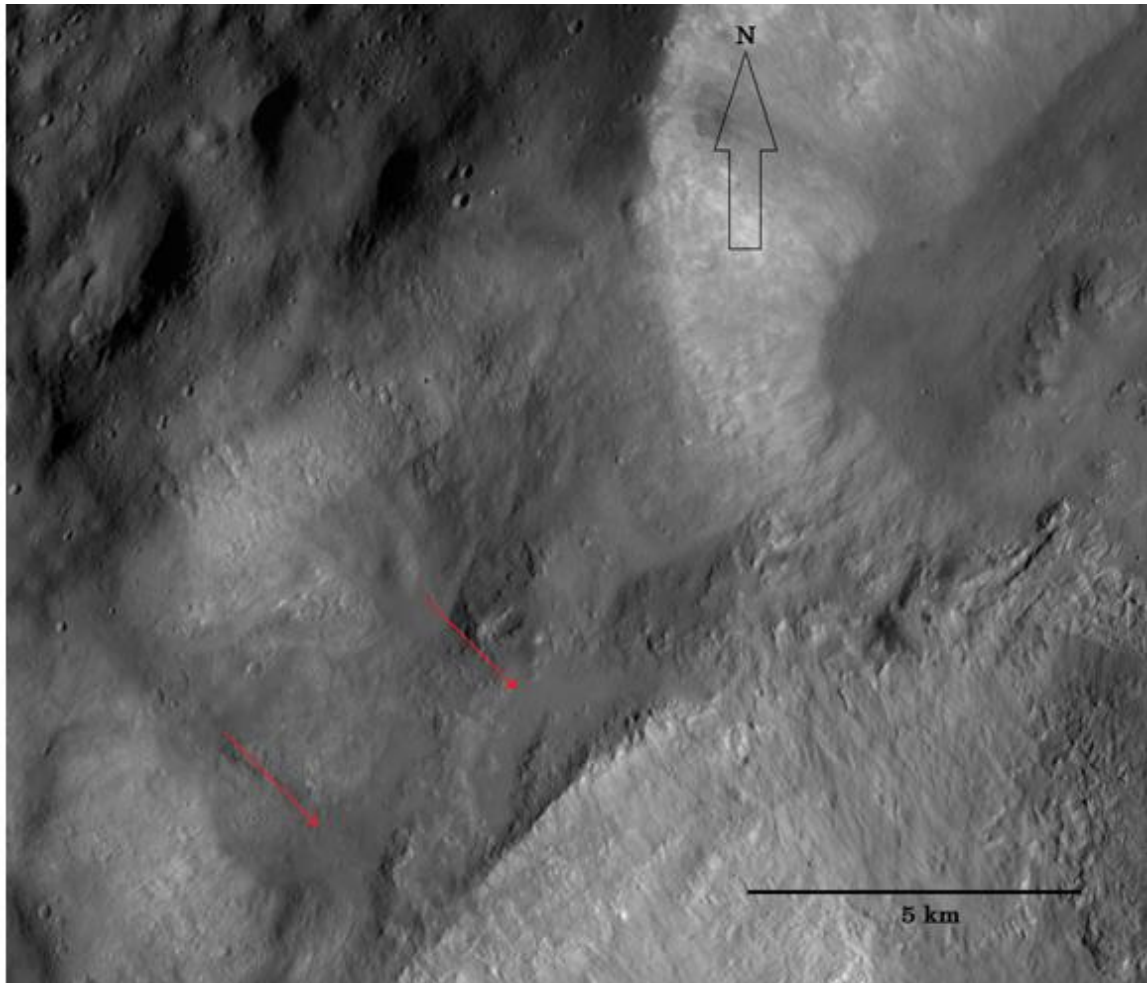


Figure 23: One of the exterior melt ponds (red arrows) about Marcia crater (located at bottom of image) on Vesta. Image from abnarchive.psi.edu/pds3/dawn/fc/ (image FC21A0010229_11287083759F1U, from 2011287_C3_ORBIT07, 2011284_CYCLE3, 2011272_HAMO, DWNVFC2_1A).

Chapter 5

5 Conclusions

This study aimed to determine how impact-generated melt was emplaced about complex craters on Mercury's surface, how that emplacement pattern compared to the known patterns found on the Moon and Venus, and what that means for other rocky bodies in the Solar System such as Mars and large asteroids.

What was found by this study was that impact-melt emplacement about craters on Mercury, the Moon, and Venus appear to be controlled by surface gravity as well as impactor velocity (which itself is influenced by gravity and location in the Solar System). Low-velocity impacts on low-gravity worlds favour ejection of melt out the crater's RCL (as on the Moon), and high-velocity impacts on high-gravity worlds favour a downrange ejection of melt (as on Venus). The results of this study on Mercury show that melt emplacement there tends to mimic the pattern observed on Venus, despite Mercury's surface gravity being less than Venus' (and its craters therefore deeper). The higher impactor velocities on Mercury produce sufficient melt to eject the material over the rims of these craters despite their depth.

The velocities of impactors striking Mercury are increased, above what Mercury's surface gravity alone could manage, due to proximity to the Sun's gravity well (Schultz, 1988; Silber et al., 2017). Thus, a study of impact-melt emplacement about complex craters on Mars may prove to be crucial. Mars possesses a surface gravity very similar to Mercury, and its southern hemisphere is similarly heavily-cratered. However, impactor velocities for Mars are lower than for Mercury (see below) so whatever trend is found on Mars may help constrain the controlling mechanism for melt emplacement as well as help constrain the surface-gravity and/or impactor-velocity threshold where the lunar end-member transitions into the Venusian end-member. If Martian craters trend similarly to Mercury's craters, despite the lower impactor velocities, then it would confirm that, in fact, surface gravity is the controlling factor. On the other hand, if Martian craters trend more closely to lunar craters than Mercurian craters, then it would confirm that impactor velocity is the controlling factor.

A potentially troubling factor about Mercury's complex craters is that, despite trending similarly to Venusian complex craters, these craters do not also follow the same downrange preference that Venusian craters do. However, the sample size used in this work ($N = 7$) is too small to make any broad conclusions. More Mercurian complex craters bearing asymmetric rays as well as exterior melt deposits are necessary in order to confirm what process is responsible for this pattern. Because two of the Mercurian craters bearing impact melts within their forbidden zones have those melt deposits situated inside adjacent, older craters, this means those craters show that trend likely as the result of pre-impact topography rather than impactor direction. In this case, melt that would otherwise have been ejected downrange is instead emplaced into the adjacent crater, regardless of impactor direction, due to that being the most energy-efficient direction of emplacement from the newly-formed crater.

It was not feasible for this study to account for all potentially melt-bearing complex craters on Mercury's surface due to limitations of the data collected by MESSENGER, as noted in prior chapters here, so future work should aim to work around these limitations by using the BepiColombo data or by using supplementary data sets from the MESSENGER mission such as the new global topography datasets currently being produced (i.e., Preusker et al., 2011, 2017a, 2017b, 2018).

Future work should also focus on studying melt emplacement about craters on additional worlds, namely Mars, but also Ceres, and Vesta. These three bodies are known to possess melt-bearing impact craters, but studying melt emplacement on these three bodies may face sample-size limitations as Martian craters are subject to endogenic processes while Ceres and Vesta may be too small to harbour a statistically significant number of fresh, melt-bearing, complex craters. Ideally, Ceres and Vesta will help confirm the lunar end-member of melt emplacement while Mars will help confirm the determining factor in melt emplacement as well as constrain what surface-gravity or impactor-velocity value serves as the threshold between the lunar and Venusian end-members.

Once the nature of the melt-emplacement paradigm is tested on multiple worlds, it should then be possible to make predictions on whether worlds like the Earth, whose impact craters are often heavily eroded, should fall on the melt-emplacement paradigm based on

what we know of that world's surface gravity and/or impactor velocities. Because melt volumes scale with impactor velocity and crater depths in turn scale with surface gravity, knowing that world's gravity and impactor velocity should be enough to predict that world's location on this paradigm.

In addition, our study did not look into melt emplacement about simple craters nor multi-ring basins. Neish et al. (2014) studied lunar simple as well as complex craters, and found that roughly 60% of simple lunar craters bore melt deposits that were situated at or very near the RCL of these craters while 80% of complex lunar craters bore the same trend. However, the lack of simple craters on Venus meant that, for consistency's sake, our work for Mercury could only be applied to complex craters. Future work should also, then, look into simple craters, as well as multi-ring basins, on multiple worlds including Mars and Mercury.

Our exercise with second-lowest (and even third-lowest) rim elevations versus melt-deposit location(s) may be worth undertaking on other worlds, like the Moon and Venus as well as applying it to bodies like Mars. It could be that conducting such an exercise on the craters of these worlds, comparing to this study's results for Mercury, can shed light on the extent of late-stage or even post-formation modifications to some of those craters. Future work might even be able to tell, for at least some of the craters, how those craters might have trended had those later modifications never occurred.

Finally, future work should aim to determine exactly how the gravitational influences of the target bodies and the Sun affect impactor velocities for those bodies and how this in turn affects melt emplacement. Is the controlling factor the increased impactor velocity with proximity to the Sun, shallower craters due to higher surface gravity, or some combination of the two? Neish et al. (2017) shows a lunar-crater trend that does not follow closely to Venus' craters despite the fact that lunar impactor velocities are similar to those experienced by Venus. Comparisons between Mercury and Mars, which have similar surface gravities but impactor velocities that vary by a factor of four, would be useful in clarifying the role of these two variables in melt emplacement.

A means of parsing solar gravitational influence on impactor velocities from planetary influences, for the rocky bodies in the Solar System, can prove useful in determining

exactly what factor is ultimately in control of how impact melt is emplaced about impact craters formed on those same bodies.

While this thesis has uncovered several important and, at times, illuminating pieces of information on the topic of impact-melt emplacement on rocky bodies, this work has also brought to light so many more unknowns that beg to be understood. It is hoped this study of Mercury will inspire a large number of future studies, that subsequently will piece together yet more pieces of the grand puzzle that is impact cratering in its entirety.

References

- Adushkin, V.V. and Nemchinov, I.V. 2008. Catastrophic Events Caused by Cosmic Objects. Institute for Dynamics of Geospheres, Russian Academy of Sciences, Moscow 119334.
- Ahrens, T.I., and O'Keefe, J.D. 1972. Shock melting and vaporization of Lunar rocks and minerals. *Moon*, **4**: 214-249.
- Anderson, B.J., Johnson, C.L., Korth, H., Purucker, M.E., Winslow, R.M., Slavin, J.A., Solomon, S.C., McNutt, Jr., R.L., Raines, J.M., Zurbuchen, T.H. 2011. *Science*, **333**: 1859-1862.
- Baker, D.M.H., Head, J.W., and Fassett, C.I. 2018. Impact-Basin Formation on Mercury: Current Observations and Outstanding Questions. *In Mercury: Current and Future Science Conference*, 2018. Universities Space Research Association, Columbia, Maryland. Abstract #6085. Available from <https://www.hou.usra.edu/meetings/mercury2018/pdf/6085.pdf>.
- Banks, M.E., Xiao, Z., Braden, S.E., Barlow, N.G., Chapman, C.R., Fassett, C.I., and Marchi, S.S. 2017. Revised constraints on absolute age limits for Mercury's Kuiperian and Mansurian stratigraphic systems. *In AGU Publications. Journal of Geophysical Research*, **122** (5): 1010-1020. Available from <https://doi.org/10.1002/2016je005254>.
- Barlow, N.G., and Banks, M.E. 2018. Constraints on the Timing of Tectonic Activity on Mercury's Large-Scale Lobate-Scarp Thrust Faults. *In Mercury: Current and Future Science Conference*, 2018. Universities Space Research Association, Columbia, Maryland. Abstract #6126. Available from <https://www.hou.usra.edu/meetings/mercury2018/pdf/6126.pdf>.
- Becker, K.J., Robinson, M.S., Becker, T.L., Weller, L.A., Edmundson, K.L., Neumann, G.A., Perry, M.E., and Solomon, S.C. 2016. First Global Digital Elevation Model of Mercury. *In 47th Lunar and Planetary Science Conference*. Lunar and

- Planetary Institute, Houston. Abstract #2959. Available from <https://www.hou.usra.edu/meetings/lpsc2016/pdf/2959.pdf>.
- Becker, K.J., Edmundson, K., Weller, L., Isbell, C., Bowman-Cisneros, E., Speyerer, E., Henriksen, M., Preusker, F., Ensor, S., Reid, M., and Korth, H. 2017. MESSENGER Digital Elevation Model Software Interface Specification, version 1.6. pp. 69.
- Blewett, D.T., Chabot, N.L., Denevi, B.W., Ernst, C.M., Head, J.W., Izenberg, N.R., Murchie, S.L., Solomon, S.C., Nittler, L.R., McCoy, T.J., Xiao, Z., Baker, D.M.H., Fassett, C.I., Braden, S.E., Oberst, J., Scholten, F., Preusker, F., and Hurwitz, D.M. 2011. Hollows on Mercury: MESSENGER Evidence for Geologically Recent Volatile-Related Activity. *Science*, **333**: 1856-1859.
- Boyce, J.M., Wilson, L., Mouginis-Mark, P.J., Hamilton, C.W., and Tornabene, L.L. 2012. Origin of small pits in martian impact craters. *Icarus*, **221**: 262-275. Available from <http://dx.doi.org/10.1016/j.icarus.2012.07.027>.
- Braden, S.E., and Robinson, M.S. 2013. Relative rates of optical maturation of regolith on Mercury and the Moon. *Journal of Geophysical Research*, **118** (9): 1903-1914.
- Cavanaugh, J.F., Smith, J.C., Sun, X., Bartels, A.E., Ramos-Izquierdo, L., Krebs, D.J., McGarry, J.F., Trunzo, R., Novo-Gradac, A.M., Britt, J.L., Karsh, J., Katz, R.B., Lukemire, A.T., Szymkiewicz, R., Berry, D.L., Swinski, J.P., Neumann, G.A., Zuber, M.T., and Smith, D.E. 2007. *Space Science Reviews*. doi:10.1007/s11214-007-9273-4.
- Chabot, N.L., Ernst, C.M., Denevi, B.W., Harmon, J.K., Murchie, S.L., Blewett, D.T., Solomon, S.C., and Zhong, E.D. 2012. Areas of permanent shadow in Mercury's south polar region ascertained by MESSENGER orbital imaging. *In AGU Publications. Geophysical Research Letters*. p. 6.
- Chabot, N.L., Ernst, C.M., Harmon, J.K., Murchie, S.L., Solomon, S.C., Blewett, D.T., and Denevi, B.W. 2013. Craters hosting radar-bright deposits in Mercury's north polar region: Areas of persistent shadow determined from MESSENGER images.

- Journal of Geophysical Research: Planets, **118**: 26-36.
doi:10.1029/2012je004172.
- Chadwick, D.J., and Schaber, G.G. 1993. Impact Crater Outflows on Venus: Morphology and Emplacement Mechanisms. *Journal of Geophysical Research*, **98** (E11): 20,891-20,902.
- Cintala, M.J., and Grieve, R.A.F. 1998. Scaling impact melting and crater dimensions: Implications for the lunar cratering record. *Meteoritics and Planetary Science*, **33**: 889-912.
- Dence, M.R. 1965. The extraterrestrial origin of Canadian craters. *Annals of the New York Academy of Science*, **123**: 941-969.
- Dence, M.R. 1968. Shock zoning at Canadian craters: petrography and structural implications. *In Shock Metamorphism of Natural Materials. Edited by French, B.M., and Short, N.M.* Mono Book Corp., Baltimore, Maryland. pp. 169-184.
- Denevi, B.W., Blewett, D.T., Buczkowski, D.L., Capaccioni, F., Capria, M.T., De Sanctis, M.C., Garry, W.B., Gaskell, R.W., Le Corre, L., Li, J.-Y., Marchi, S., McCoy, T.J., Nathues, A., O'Brien, D.P., Petro, N.E., Pieters, C.M., Preusker, F., Raymond, C.A., Reddy, V., Russell, C.T., Schenk, P., Scully, J.E.C., Sunshine, J.M., Tosi, F., Williams, D.A., and Wyrick, D. 2012. Pitted Terrain on Vesta and Implications for the Presence of Volatiles. *Science*, **338**: 246-249.
- Ernst, C.M., Chabot, N.L., and Barnouin, O.S. 2016. Examining the Potential Contribution of the Hokusai Impact to Water Ice on Mercury. *In 47th Lunar and Planetary Science Conference.* Lunar and Planetary Institute, Houston. Abstract #1374. Available from <https://www.hou.usra.edu/meetings/lpsc2016/pdf/1374.pdf>.
- Galluzzi, V., Rothery, D.A., Massironi, M., Ferranti, L., and the Mercury Mapping Team. 2018. Towards the Redefinition of the Global Stratigraphy of Mercury: The Case of the Intermediate Plains. *In Mercury: Current and Future Science Conference, 2018.* Universities Space Research Association, Columbia, Maryland. Abstract

#6041. Available from

<https://www.hou.usra.edu/meetings/mercury2018/pdf/6041.pdf>.

- Gault, D.E., Quaide, W.L., and Oberbeck, V.R. 1968. Impact cratering mechanics and structures. In *Shock Metamorphism of Natural Materials*. Edited by B.M.French, and N.M Short. Mono Book Corp., Baltimore, Maryland. pp. 87-99.
- Genova, A., Goossens, S., Mazarico, E., Lemoine, F.G., Neumann, G.A., Kuang, W., Sabaka, T.J., Smith, D.E., and Zuber, M.T. 2018 (a). A Large Solid Inner Core at Mercury. In *Mercury: Current and Future Science Conference*, 2018. Universities Space Research Association, Columbia, Maryland. Abstract #6036. Available from <https://www.hou.usra.edu/meetings/mercury2018/pdf/6036.pdf>.
- Genova, A., Goossens, S., Mazarico, E., Lemoine, F.G., Neumann, G.A., Kuang, W., Sabaka, T.J., Smith, D.E., and Zuber, M.T. 2018 (b). In 49th Lunar and Planetary Science Conference. Lunar and Planetary Institute, Houston. Abstract #1659. Available from <https://www.hou.usra.edu/meetings/lpsc2018/pdf/1659.pdf>.
- Grieve, R.A.F., Dence, M.R., and Robertson, P.B. 1977. Cratering processes: as interpreted from the occurrences of impact melts. In *Impact and Explosion Cratering*. Edited by Roddy, D.J., Pepin, R.O., and Merrill, R.B. Pergamon Press, New York. pp. 791-814.
- Grieve, R.A.F., and Cintala, M.J. 1982. A method for estimating the initial impact conditions of terrestrial cratering events, exemplified by its application to Brent crater, Ontario. *Proceedings of the Lunar and Planetary Science Conference*, 12B: 1607-1621.
- Grieve, R.A.F., and Cintala, M.J. 1995. Impact melting on Venus: some considerations for the nature of the cratering record. *Icarus*, **114**: 68-79.
- Grieve, R.A.F., and Cintala, M.J. 1997. Planetary differences in impact melting. *Advances in Space Research*, **10** (8): 1551-1560.
- Hawke, B.R., and Head, J.W. 1977. Impact melt on lunar crater rims. Edited by Roddy, J.W., Pepin, R.O., and Merrill, R.B. Pergamon Press, New York. pp. 815-841.

- Hawkins III, S.E., Boldt, J.D., Darlington, E.H., Espiritu, R., Gold, R.E., Gotwols, B., Grey, M.P., Hash, C.D., Hayes, J.R., Jaskulek, S.E., Kardian, Jr., C.J., Keller, M.R., Malaret, E.R., Murchie, S.L., Murphy, P.K., Peacock, K., Prockter, L.M., Reiter, R.A., Robinson, M.S., Schaefer, E.D., Shelton, R.G., Sterner II, R.E., Taylor, H.W., Watters, T.R., and Williams, B.D. 2007. The Mercury Dual Imaging System on the MESSENGER Spacecraft. *Space Science Reviews*, **131**: 247-338.
- Head, J.W., Chapman, C.R., Strom, R.G., Fassett, C.I., Denevi, B.W., Blewett, D.T., Ernst, C.M., Watters, T.R., Solomon, S.C., Murchie, S.L., Prockter, L.M., Chabot, N.L., Gillis-Davis, J.J., Whitten, J.L., Goudge, T.A., Baker, D.M.H., Hurwitz, D.M., Ostrach, L.R., Xiao, Z., Merline, W.J., Kerber, L., Dickson, J.L., Oberst, J., Byrne, P.K., Klimczak, C., and Nittler, L.R. 2011. Flood Volcanism in the Northern High Latitudes of Mercury Revealed by MESSENGER. *Science*, **333**: 1853-1856.
- Herrick, R.R. 2018. The Nonrandom Distribution of Interior Landforms for ~100-km Diameter Craters on Mercury Suggests Regional Variations in Near-Surface Mechanical Properties. *In Mercury: Current and Future Science Conference*, 2018. Universities Space Research Association, Columbia, Maryland. Abstract #6109. Available from <https://www.hou.usra.edu/meetings/mercury2018/pdf/6109.pdf>.
- Hood, L.L., Oliveira, J.S., Spudis, P.D., and Galluzzi, V. 2018. Investigating Sources of Mercury's Crustal Magnetic Field: Further Mapping of MESSENGER Magnetometer Data. *In 49th Lunar and Planetary Science Conference*. Lunar and Planetary Institute, Houston. Abstract #2109. Available from <https://www.hou.usra.edu/meetings/lpsc2018/pdf/2109.pdf>.
- Ivanov, B.A. 2001. Mars/Moon Cratering Rate Ratio Estimates. *Chronology and Evolution of Mars*, **96**: 87-104.
- Kinczyk, M.J., Byrne, P.K., Prockter, L.M., Susorney, H.C.M., and Barnouin, O.S. 2018 (a). Crater Degradation on Mercury: A Global Perspective. *In Mercury: Current*

- and Future Science Conference, 2018. Universities Space Research Association, Columbia, Maryland. Abstract #6116. Available from <https://www.hou.usra.edu/meetings/mercury2018/pdf/6116.pdf>.
- Kinczyk, M.J., Barnouin, O.S., Ernst, C.M., and Byrne, P.K. 2018 (b). A Tale of Two Craters: Using Geological Mapping to Assess the Role of Impact Melt in the Formation of Hokusai Crater, Mercury. *In* 49th Lunar and Planetary Science Conference. Lunar and Planetary Institute, Houston. Abstract #2916. Available from <https://www.hou.usra.edu/meetings/lpsc2018/pdf/2916.pdf>.
- King, S.D., and Robertson, S. 2018. Geodynamics in a Thin Spherical Shell. *In* 49th Lunar and Planetary Science Conference. Lunar and Planetary Institute, Houston. Abstract #6033. Available from <https://www.hou.usra.edu/meetings/lpsc2018/pdf/6033.pdf>.
- Krohn, K., Jaumann, R., Stephan, K., Otto, K.A., Schmedemann, N., Wagner, R.J., Matz, K.-D., Tosi, F., Zambon, F., von der Gathen, I., Schulzeck, F., Schröder, S.E., Buczkowski, D.L., Hiesinger, H., McSween, H.Y., Pieters, C.M., Preusker, F., Roatsch, T., Raymond, C.A., Russell, C.T., and Williams, D.A. 2016. Cryogenic flow features on Ceres: Implications for crater-related cryovolcanism. *In* AGU Publications. Geophysical Research Letters. p. 10.
- Lefevre, M., and Wieczorek, M. 2008. Nonuniform cratering of the terrestrial planets. *Icarus*, **197** (1): 291-306. doi:10.1016/j.icarus.2008.04.011.
- Leight, C., and Ostrach, L.R. 2018. Characterizing Impact Melt on Mercury. *In* 49th Lunar and Planetary Science Conference. Lunar and Planetary Institute, Houston. Abstract #2553. Available from <https://www.hou.usra.edu/meetings/lpsc2018/pdf/2553.pdf>.
- Lewis, P.A.W. 1961. Distribution of the Anderson-Darling Statistic. *The Annals of Mathematical Statistics*. 1118-1124.
- Lucchetti, A., Pajola, M., Galluzzi, V., Giacomini, L., Carli, C., Cremonese, G., Marzo, G.A., Massironi, M., and Roush, T. 2018. Spectral Clustering and

- Geomorphological Analysis on Mercury Hollows. *In Mercury: Current and Future Science Conference*, 2018. Universities Space Research Association, Columbia, Maryland. Abstract #6028. Available from <https://www.hou.usra.edu/meetings/mercury2018/pdf/6028.pdf>.
- Marchi, S., Mottola, S., Cremonese, G., Massironi, M., and Martellato, E. 2009. A new chronology for the Moon and Mercury. Available from arXiv:0903.5137v1.
- Marvin, U.B., and Kring, D.A. 1992. Authentication controversies and impactite petrography of the New Quebec crater. *Meteoritics*, **27**: 585-595.
- Melosh, H.J. 1989. Impact Cratering: A Geologic Process. *In Oxford Monographs on Geology and Geophysics* no. 11. p. 258.
- Melosh, H.J., and Ivanov, B.A. 1999. Impact crater collapse. *Annual Review of Earth and Planetary Science*, **27**: 385-415.
- Naumov, M.V. 2005. Principal features of impact-generated hydrothermal circulation systems: mineralogical and geochemical evidence. *Geofluids*, **5**: 165-184.
- Neish, C.D., Blewett, D.T., Harmon, J.K., Coman, E.I., Cahill, J.T.S., and Ernst, C.M. 2013. A comparison of rayed craters on the Moon and Mercury. *Journal of Geophysical Research*, **118**. doi:10.1002/jgre.20166.
- Neish, C.D., Madden, J., Carter, L.M., Hawke, B.R., Giguere, T., Bray, V.J., Osinski, G.R., and Cahill, J.T.S. 2014. Global distribution of lunar impact melt flows. *Icarus*, **239**: 105-117. Available from <http://dx.doi.org/10.1016/j.icarus.2014.05.049>.
- Neish, C.D., Herrick, R.R., Zanetti, M., and Smith, D. 2017. The role of pre-impact topography in impact melt emplacement on terrestrial planets. *Icarus*, **297**: 240-251. Available from <http://dx.doi.org/10.1016/j.icarus.2017.07.004>.
- Oberbeck, V.R. 1975. The role of ballistic erosion and sedimentation in lunar stratigraphy. *Reviews of Geophysics and Space Physics*, **13**: 337-362.

- Osinski, G.R., Lee, P., and Parnell, J., Spray, J.G., and Baron, M. 2005. A case study of impact-induced hydrothermal activity: the Haughton impact structure, Devon Island, Canadian High Arctic. *Meteoritics and Planetary Science*, **40**: 1859-1878.
- Osinski, G.R., Tornabene, L.L., and Grieve, R.A.F. 2011. Impact ejecta emplacement on terrestrial planets. *Earth and Planetary Science Letters*, **310**: 167-181. doi:10.1016/j.epsl.2011.08.012.
- Osinski, G.R., Tornabene, L.L., and Banerjee, N.R., Cockell, C.S., Flemming, R., Izawa, M.R.M., McCutcheon, J., Parnell, J., Preston, L.J., Pickersgill, A.E., Pontefract, A., Sapers, H.M., and Southam, G. 2012. Impact-generated hydrothermal systems on Earth and Mars. *Icarus*, **224** (2): 347-363. Available from <http://dx.doi.org/10.1016/j.icarus.2012.08.030>.
- Osinski, G.R., and Pierazzo, E. 2013. *Impact Cratering: Processes and Products*, 1st edition. Wiley-Blackwell Press.
- Peplowski, P.N., Evans, L.G., Hauck II, S.A., McCoy, T.J., Boynton, W.V., Gillis-Davis, J.J., Ebel, D.S., Goldsten, J.O., Hamara, D.K., Lawrence, D.J., McNutt, Jr., R.L., Nittler, L.R., Solomon, S.C., Rhodes, E.A., Sprague, A.L., Starr, R.D., and Stockstill-Cahill, K.R. 2011. Radioactive Elements on Mercury's Surface from MESSENGER: Implications for the Planet's Formation and Evolution. *Science*, **333**: 1850-1852.
- Preusker, F., Oberst, J., Head, J.W., Watters, T.R., Robinson, M.S., Zuber, M.T., and Solomon, S.C. 2011. Stereo topographic models of Mercury after three MESSENGER flybys. *Planetary and Space Science*, **59**: 1910-1917. doi:10.1016/j.pss.2011.07.005.
- Preusker, F., Stark, A., Oberst, J., Matz, K.-D., Gwinner, K., Roatsch, T., and Watters, T.R. 2017 (a). Toward high-resolution global topography of Mercury from MESSENGER orbital stereo imaging: A prototype model for the H6 (Kuiper) quadrangle. *Planetary and Space Science*, **142**: 26-37. Available from <http://dx.doi.org/10.1016/j.pss.2017.04.012>.

- Preusker, F., Oberst, J., Stark, A., Matz, K.-D., Gwinner, K., and Roatsch, T. 2017 (b). High-resolution topography from MESSENGER orbital stereo imaging – the H3 quadrangle “Shakespeare.” *In* 48th Lunar and Planetary Science Conference. Lunar and Planetary Institute, Houston. Abstract #1441.
- Preusker, F., Stark, A., Oberst, J., Matz, K.-D., Roatsch, T., Burmeister, S., and Gwinner, K. 2018. High-resolution Topography from MESSENGER Orbital Stereo Imaging – the Southern Hemisphere. *In* Mercury: Current and Future Science Conference, 2018. Universities Space Research Association, Columbia, Maryland. Abstract #6031. Available from <https://www.hou.usra.edu/meetings/mercury2018/pdf/6031.pdf>.
- Schultz, P.H. 1988. Cratering on Mercury: a relook. *In* Mercury. Edited by Vilas, F., Chapman, C.R., and Matthews, M.H. University of Arizona Press, Tucson, Arizona. pp. 274-335.
- Silber, E.A., Osinski, G.R., Johnson, B.C., and Grieve, R.A.F. 2017. Effect of impact velocity and acoustic fluidization on the simple-to-complex transition of lunar craters. *In* JGR-Planets. p. 39.
- Sizemore, H.G., Platz, T., Schorghofer, N., Prettyman, T.H., De Sanctis, M.C., Crown, D.A., Schmedemann, N., Neesemann, A., Kniessl, T., Marchi, S., Schenk, P.M., Bland, M.T., Schmidt, B.E., Hughson, K.H.G., Tosi, F., Zambon, F., Mest, S.C., Yingst, R.A., Williams, D.A., Russell, C.T., and Raymond, C.A. 2017. Pitted terrains on (1) Ceres and implications for shallow subsurface volatile distribution. *In* AGU Publications. Geophysical Research Letters. pp. 6570-6578.
- Solomon, S.C., McNutt, Jr., R.L., Gold, R.E., Acuña, M.H., Baker, D.N., Boynton, W.V., Chapman, C.R., Cheng, A.F., Gloeckler, G., Head III, J.W., Krimigis, S.M., McClintock, W.E., Murchie, S.L., Peale, S.J., Phillips, R.J., Robinson, M.S., Slavin, J.A., Smith, D.E., Strom, R.G., Trombka, J.I., and Zuber, M.T. 2001. The MESSENGER mission to Mercury: scientific objectives and implementation. *Planetary and Space Science*, **49**: 1445-1465.

- Solomon, S.C., McNutt, Jr., R.L., Gold, R.E., and Dominigue, D.L. 2007. MESSENGER Mission Overview. *Space Science Reviews*, **131**: 3-39. doi:10.1007/s11214-007-9247-6.
- Sori, M.M. 2018. Mercury's Thin Crust. *In* 49th Lunar and Planetary Science Conference. Lunar and Planetary Institute, Houston. Abstract #1048. Available from <https://www.hou.usra.edu/meetings/lpsc2018/pdf/1048.pdf>.
- Stopar, J.D., Hawke, B.R., Robinson, M.S., Denevi, B.W., Giguere, T.A., and Koeber, S.D. 2014. Occurrence and mechanisms of impact melt emplacement at small lunar craters. *Icarus*, **243**: 337-357.
- Susorney, H.C.M., Barnouin, O.S., Ernst, C.M., and Johnson, C.L. 2016. Morphometry of impact craters on Mercury from MESSENGER altimetry and imaging. *Icarus*, **271**: 180-193. Available from <http://dx.doi.org/10.1016/j.icarus.2016.01.022>.
- Tauber, M.E., and Kirk, D.B. 1976. Impact Craters on Venus. *Icarus*, **28**: 351-357.
- Tornabene, L.L., Osinski, G.R., McEwen, A.S., Boyce, J.M., Bray, V.J., Caudill, C.M., Grant, J.A., Hamilton, C.W., Mattson, S., and Mouginis-Mark, P.J. 2012. Widespread crater-related pitted materials on Mars: Further evidence for the role of target volatiles during the impact process. *Icarus*, **220**: 348-368.
- Watters, T.R., Solomon, S.C., Robinson, M.S., Head, J.W., André, S.L., Hauck II, S.A., and Murchie, S.L. 2009. The tectonics of Mercury: The view after MESSENGER's first flyby. *Earth and Planetary Science Letters*, **285**: 283-296. doi:10.1016/j.epsl.2009.01.025.
- Wünnemann, K., Collins, G.S., and Osinski, G.R. 2008. Numerical modelling of impact melt production in porous rocks.
- Zharkova, A.Y., Karachevtseva, I.P., Zubarev, A.E., Brusnikin, E.S., Kokhanov, A.A., Kreslavsky, M.A. 2016. The study of Mercury's surface by cartography methods based on the newest topographic data derived from MESSENGER image processing. *Current Problems of Remote Sensing of the Earth from Space*, **13** (5):

265-274. Available from <https://doi.org/10.21046/2070-7401-2016-13-5-265-274>.

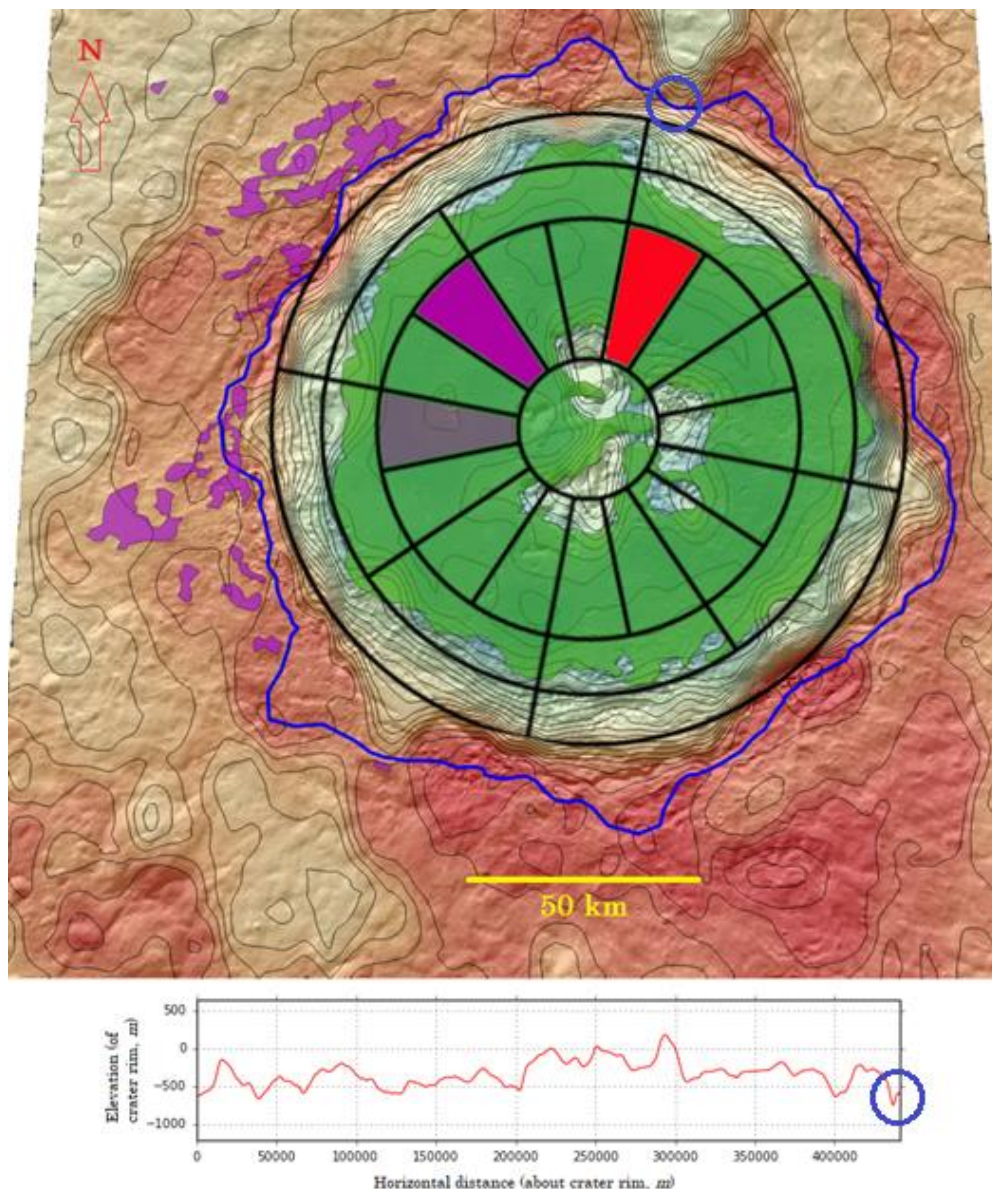
Appendices

Appendix A holds screen captures of the twenty-four crater files used in this thesis.

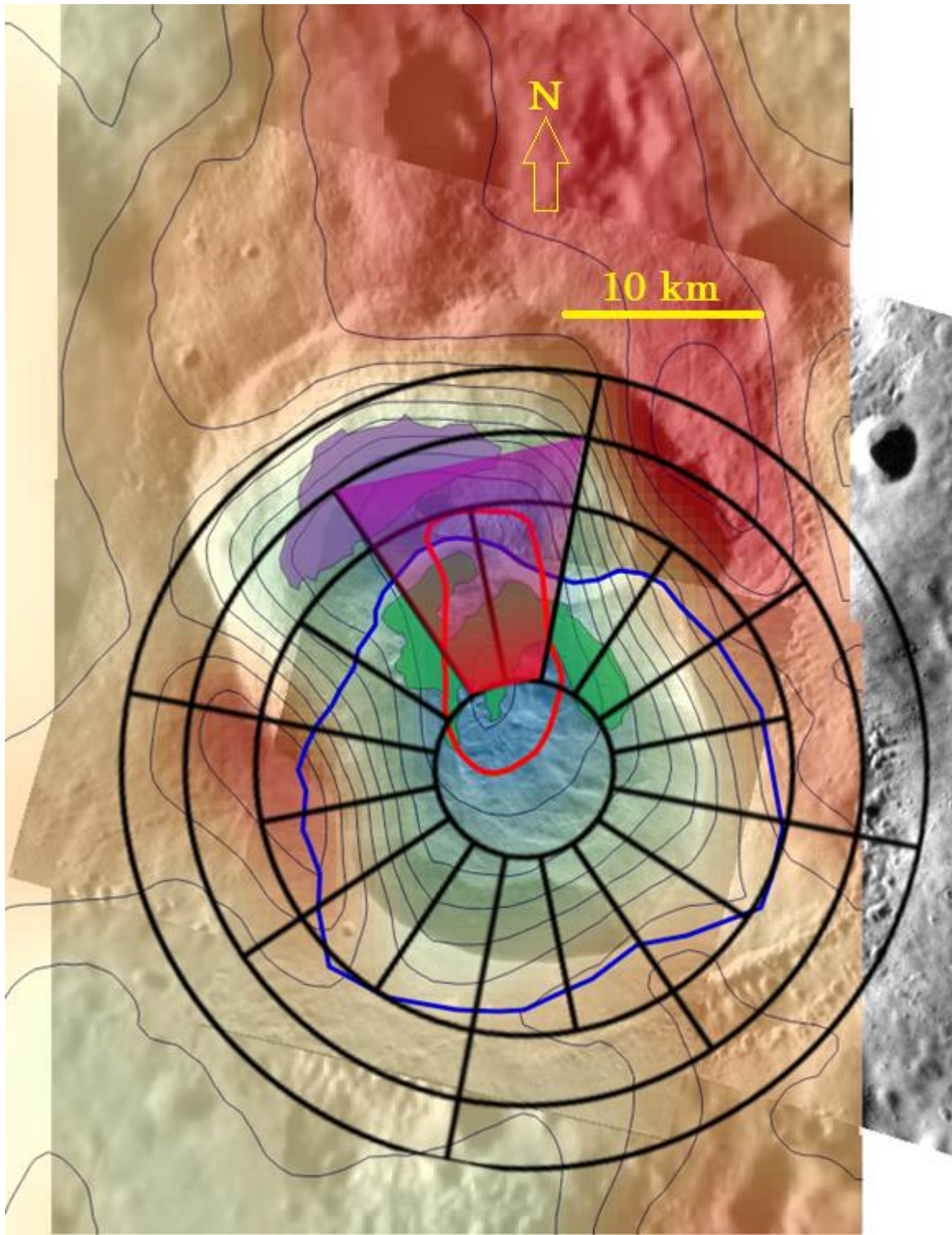
Appendix B lists the EDRNAC images used, all of which were downloaded from the Mercury Orbital Data Explorer.

Appendix A: Individual crater files created for Impact Melt-Bearing Mercurian Complex Craters Catalog.

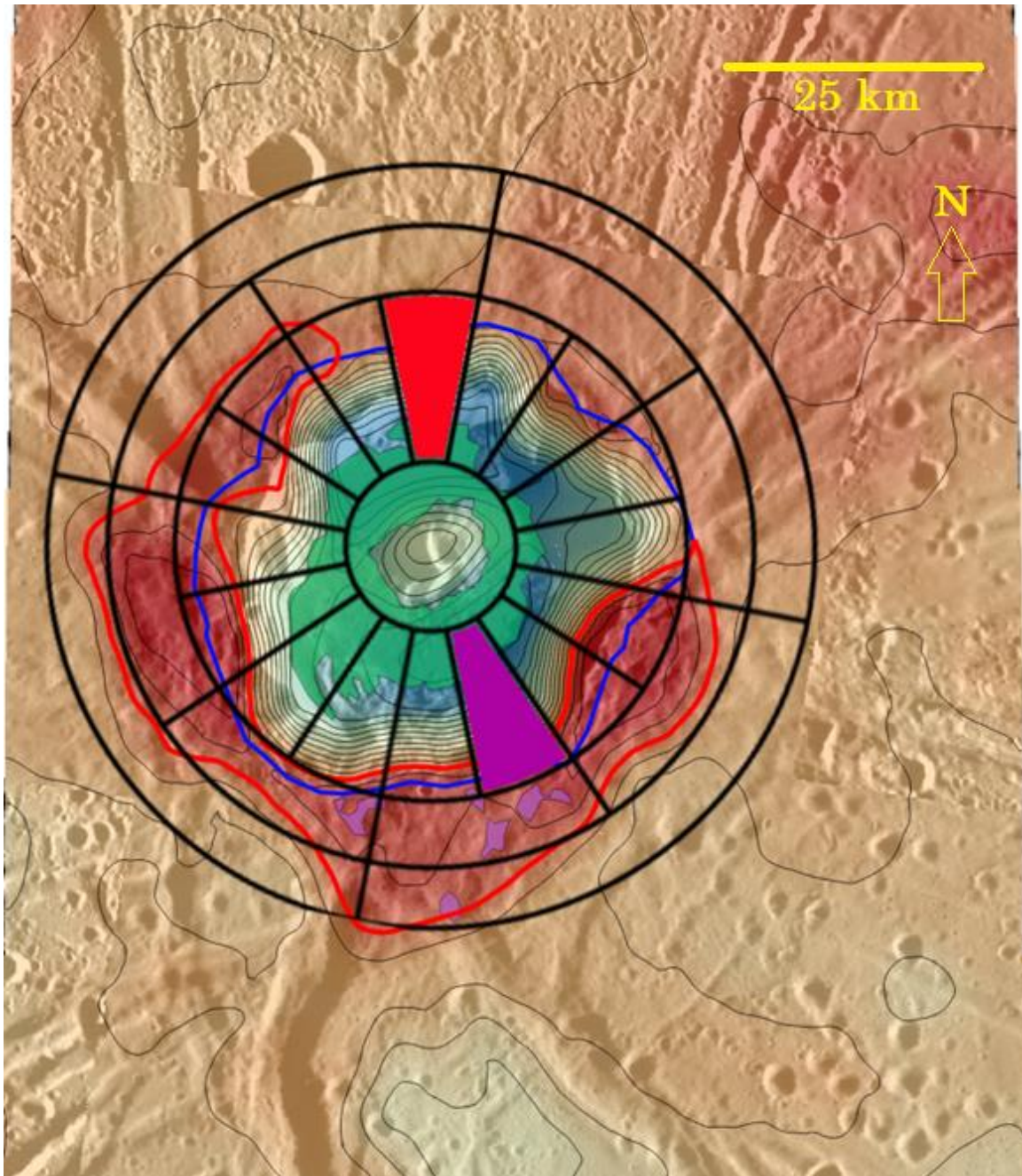
Abedin crater:



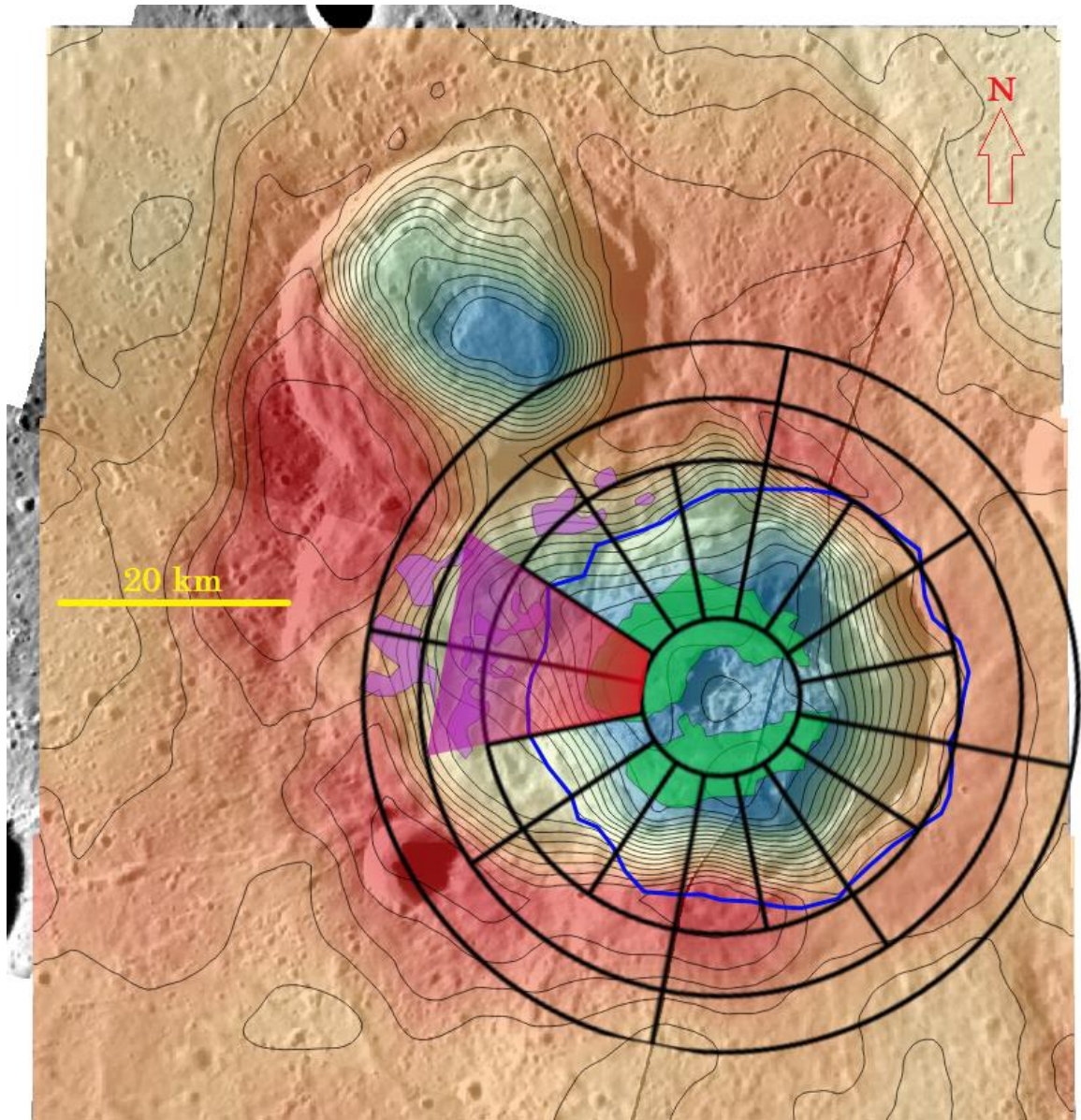
Ailey crater:



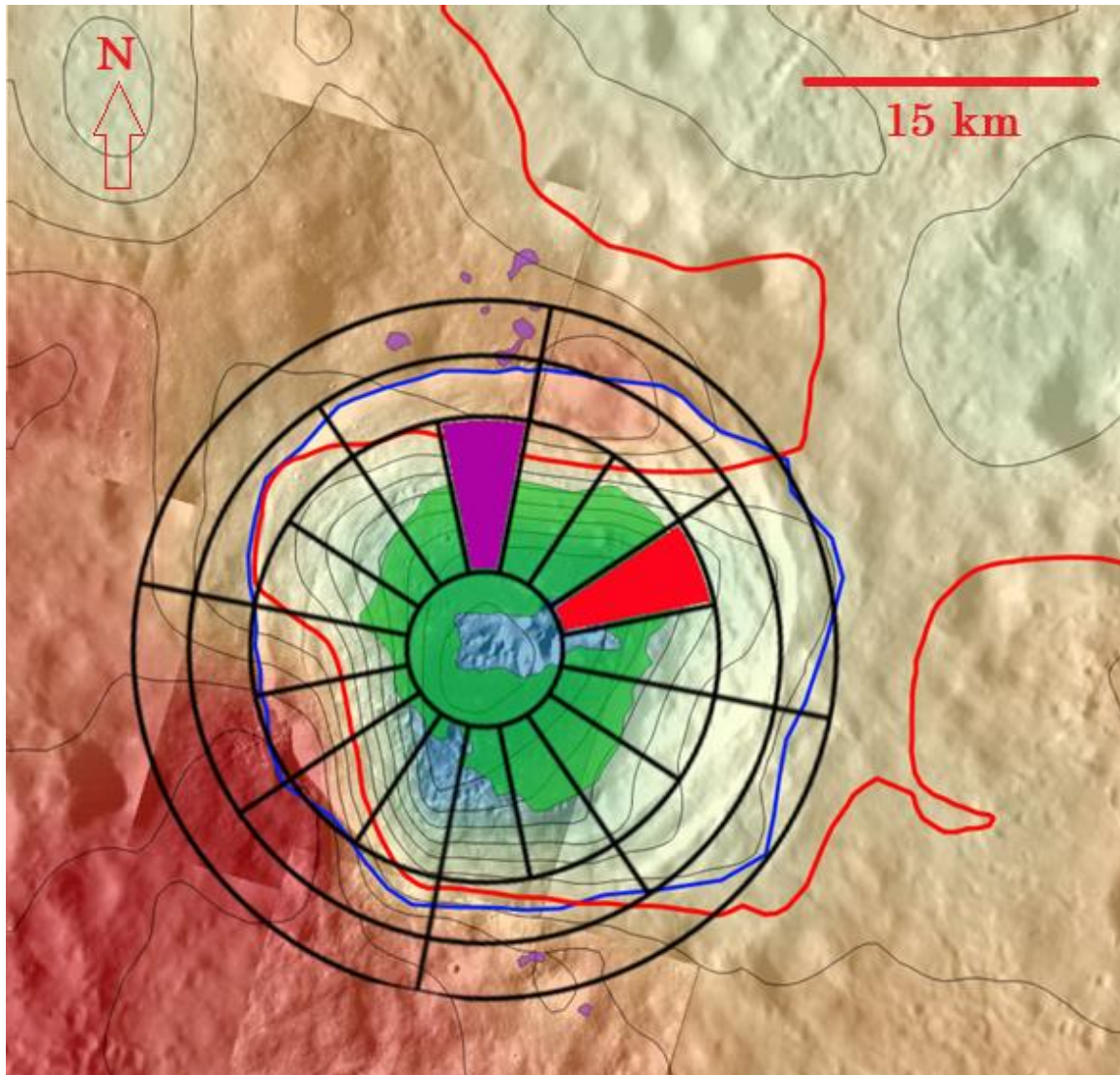
Apollodorus crater:



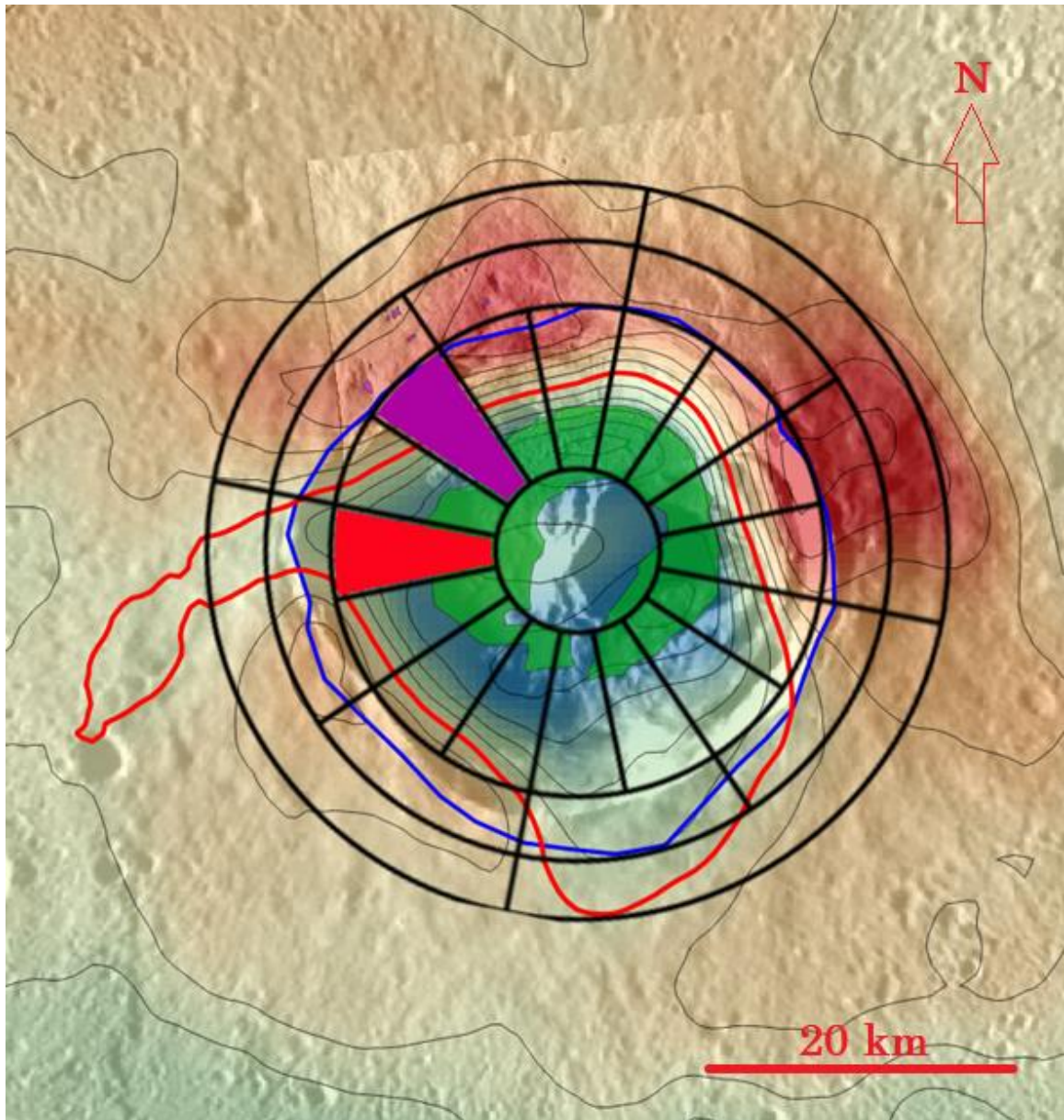
Balanchine crater:



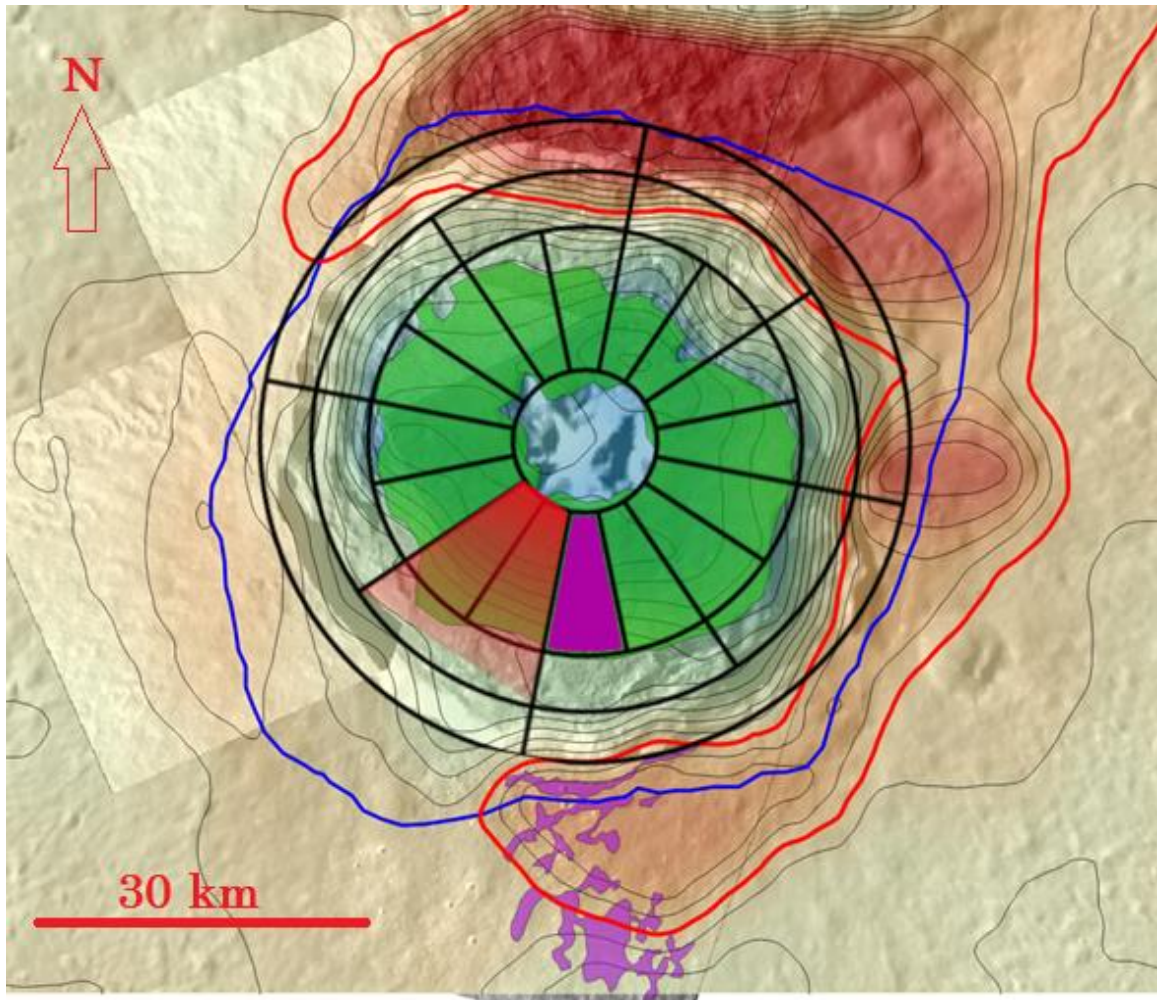
Bek crater:



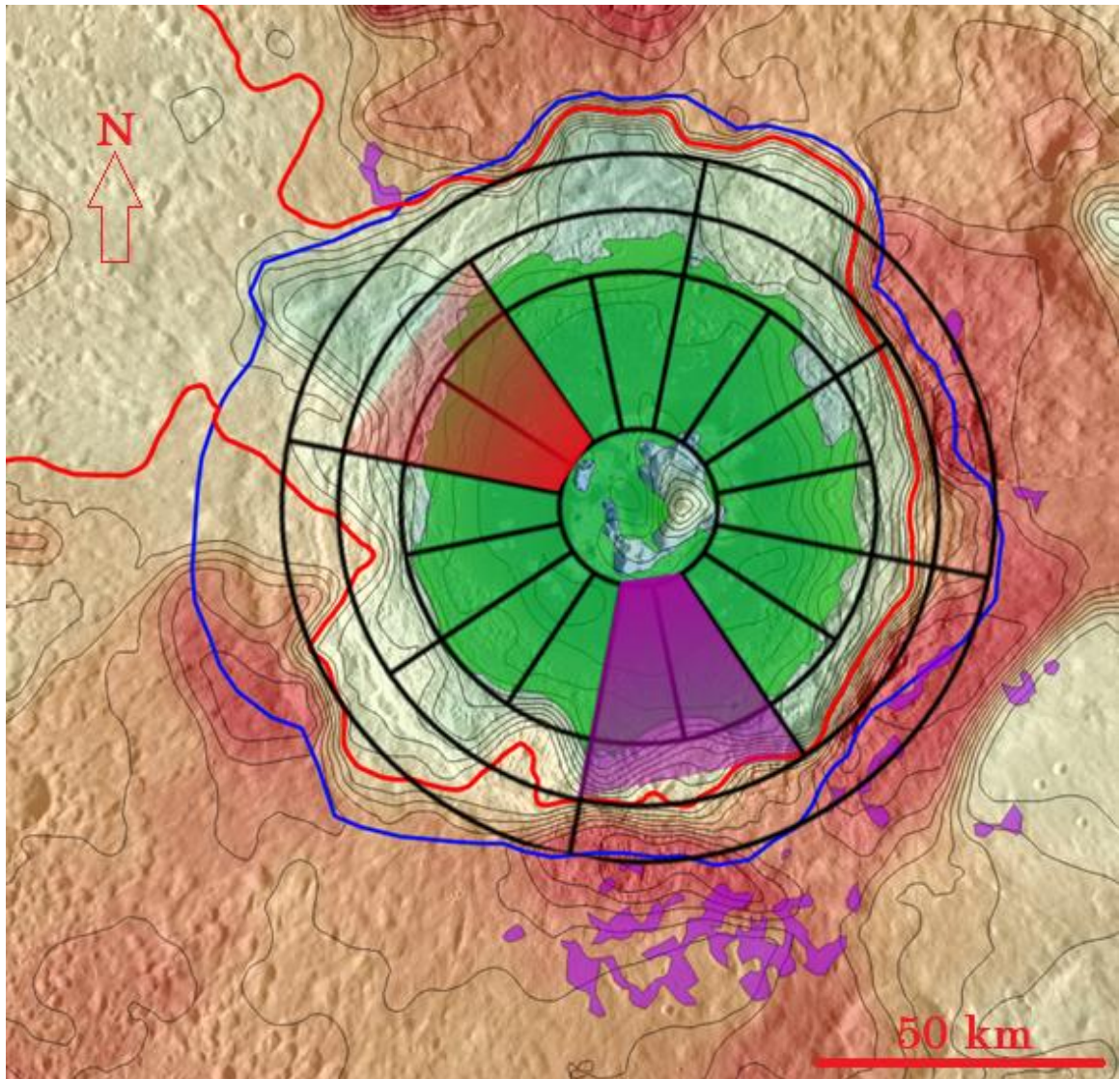
Cunningham crater:



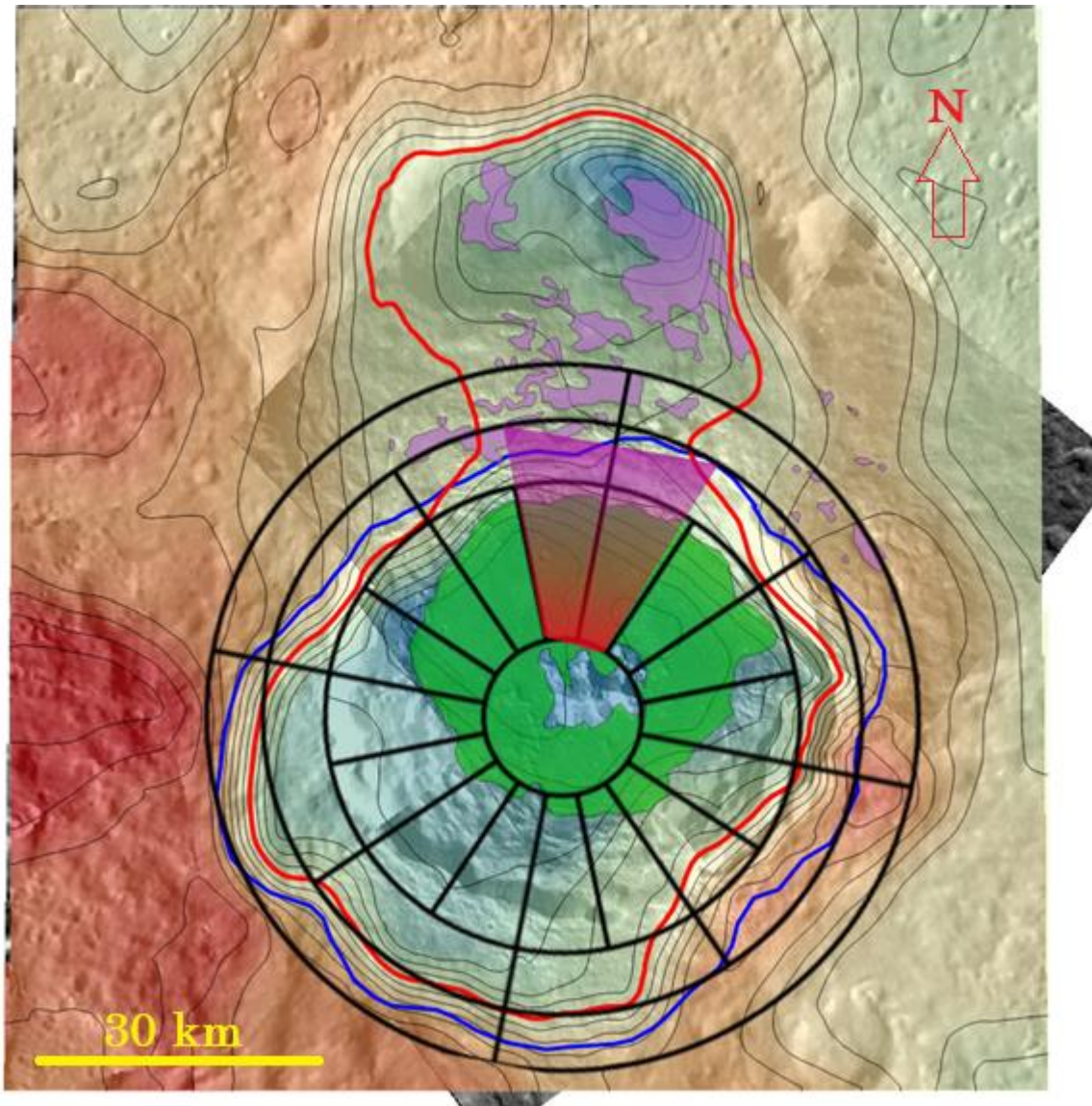
Degas crater:



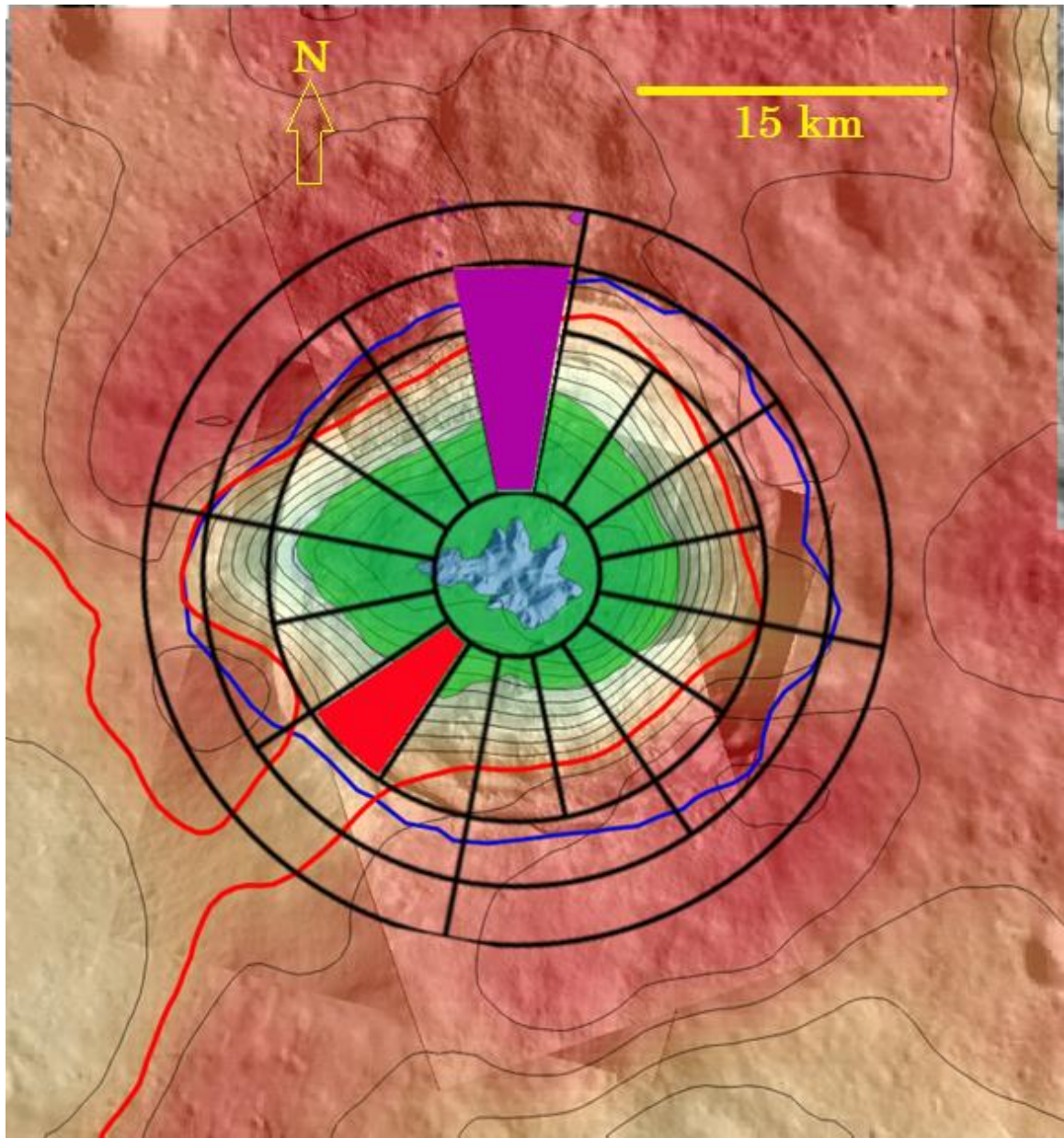
Eminescu crater:



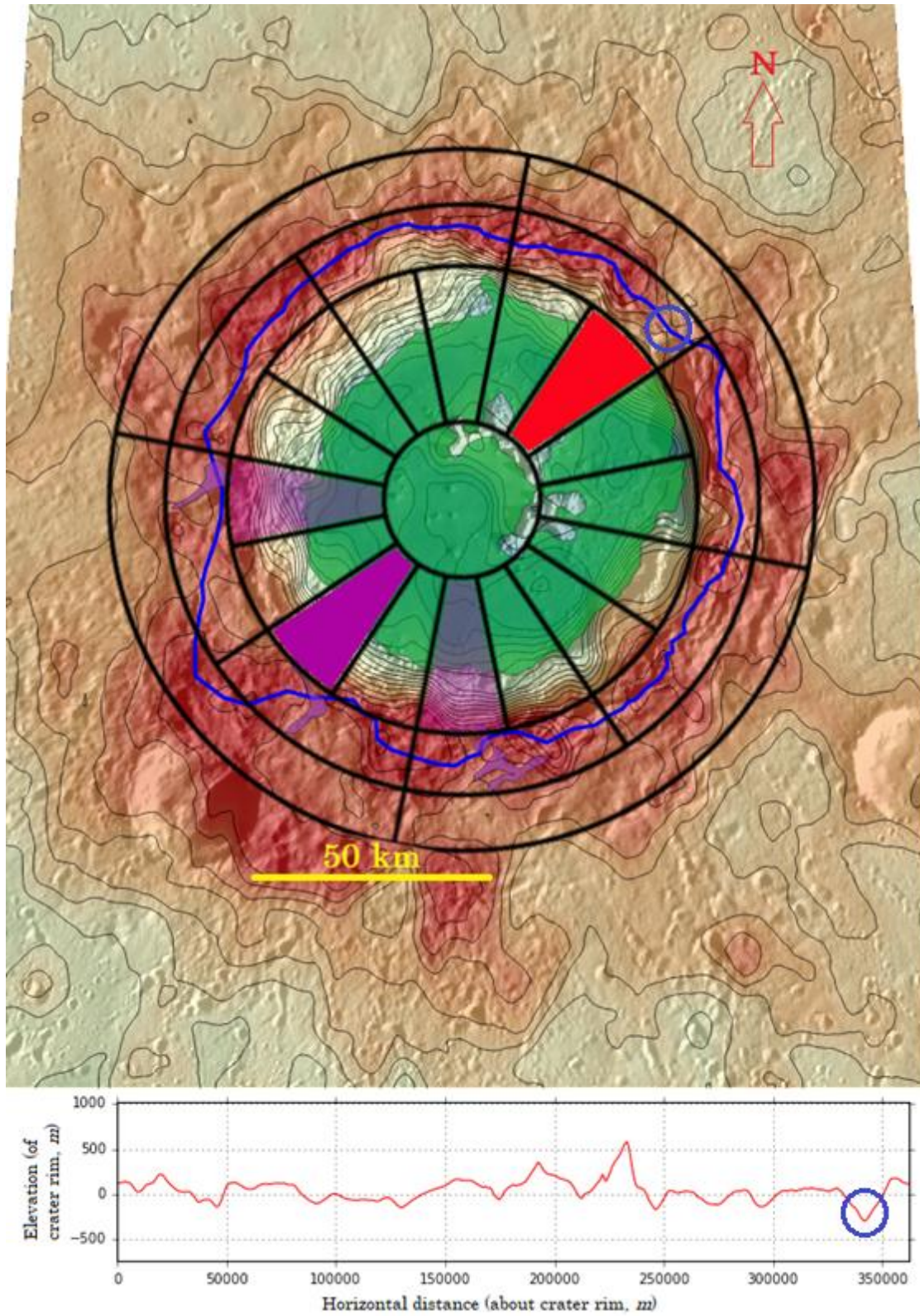
Erte crater:



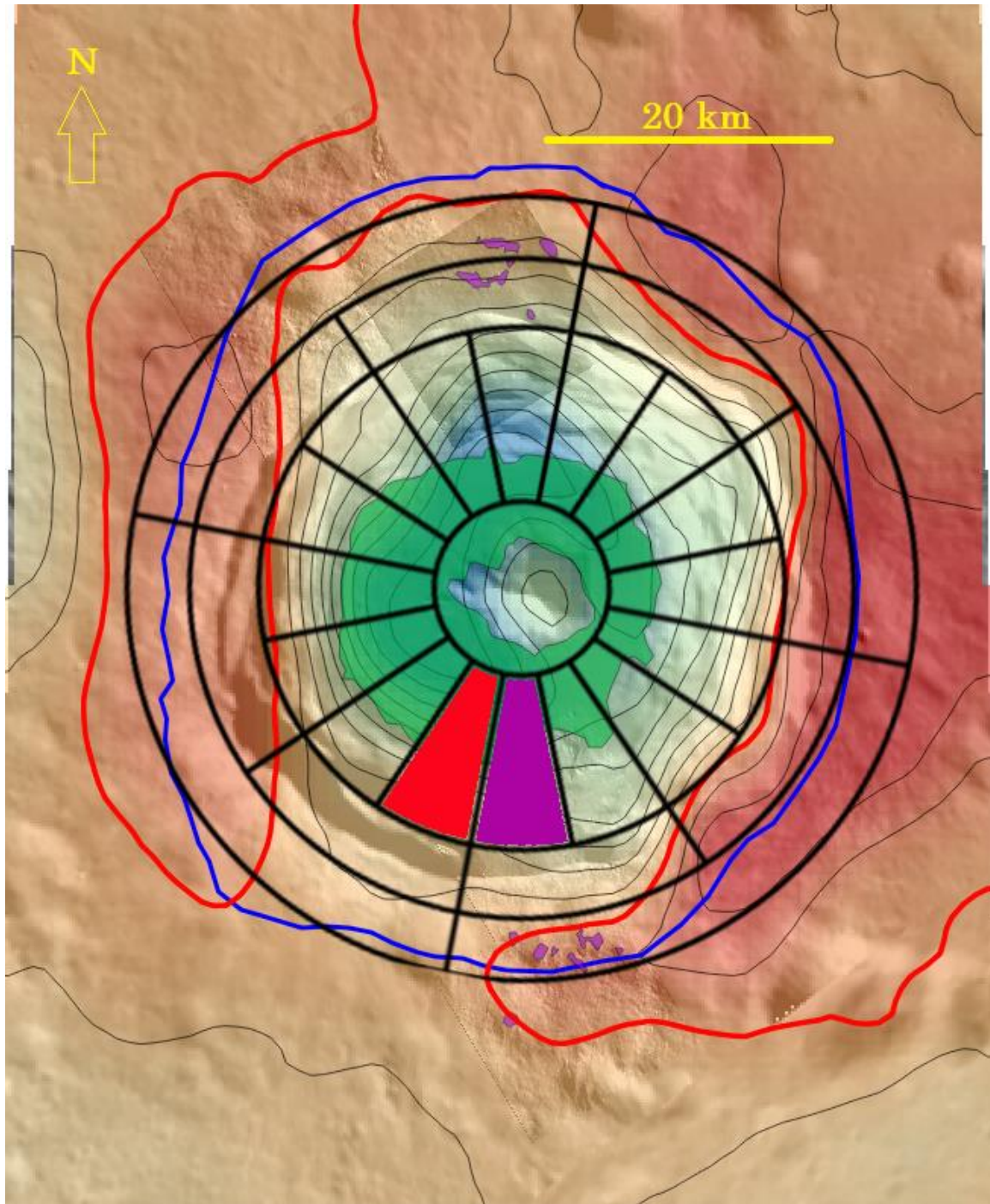
Fonteyn crater:



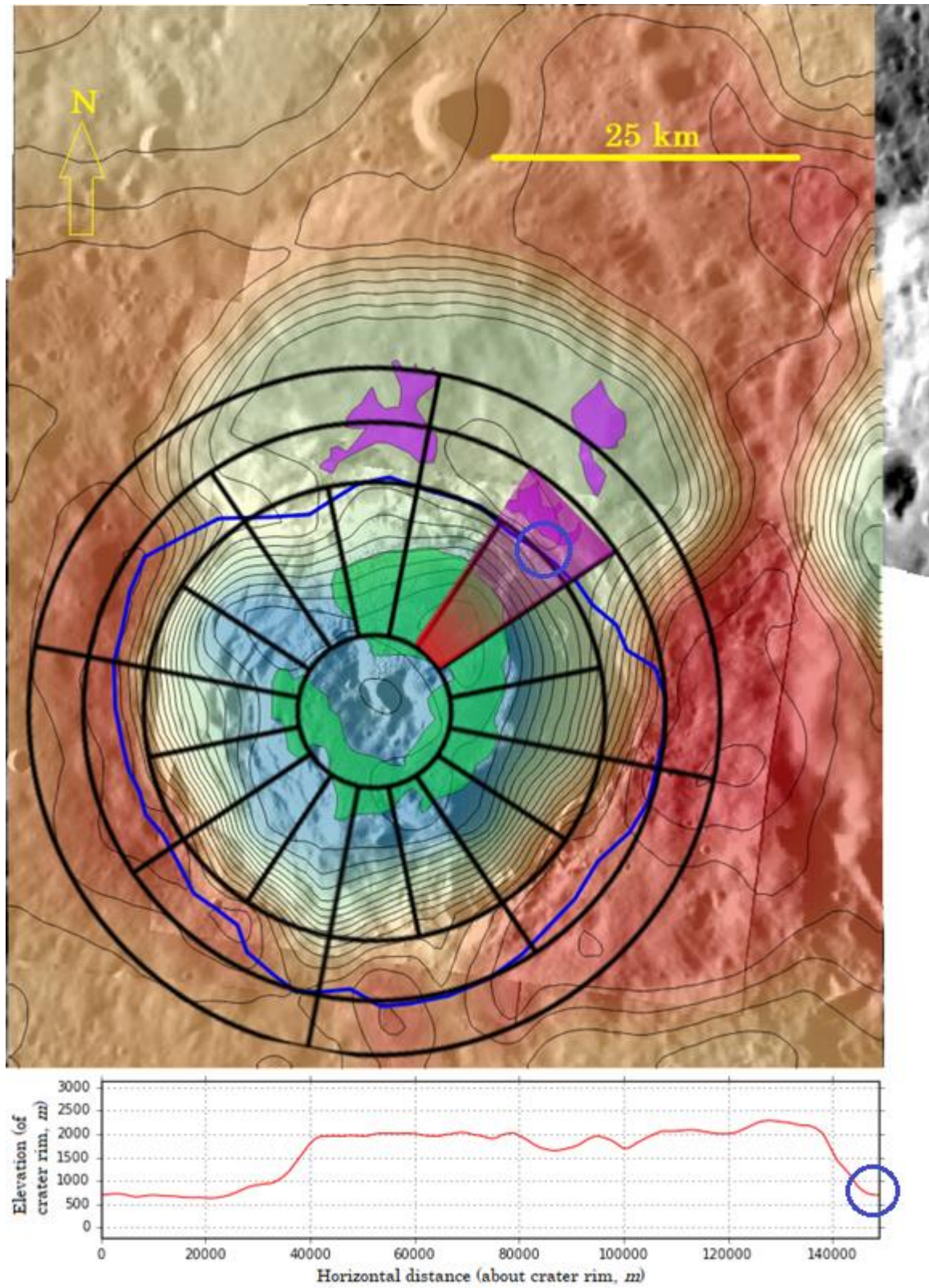
Hokusai crater:



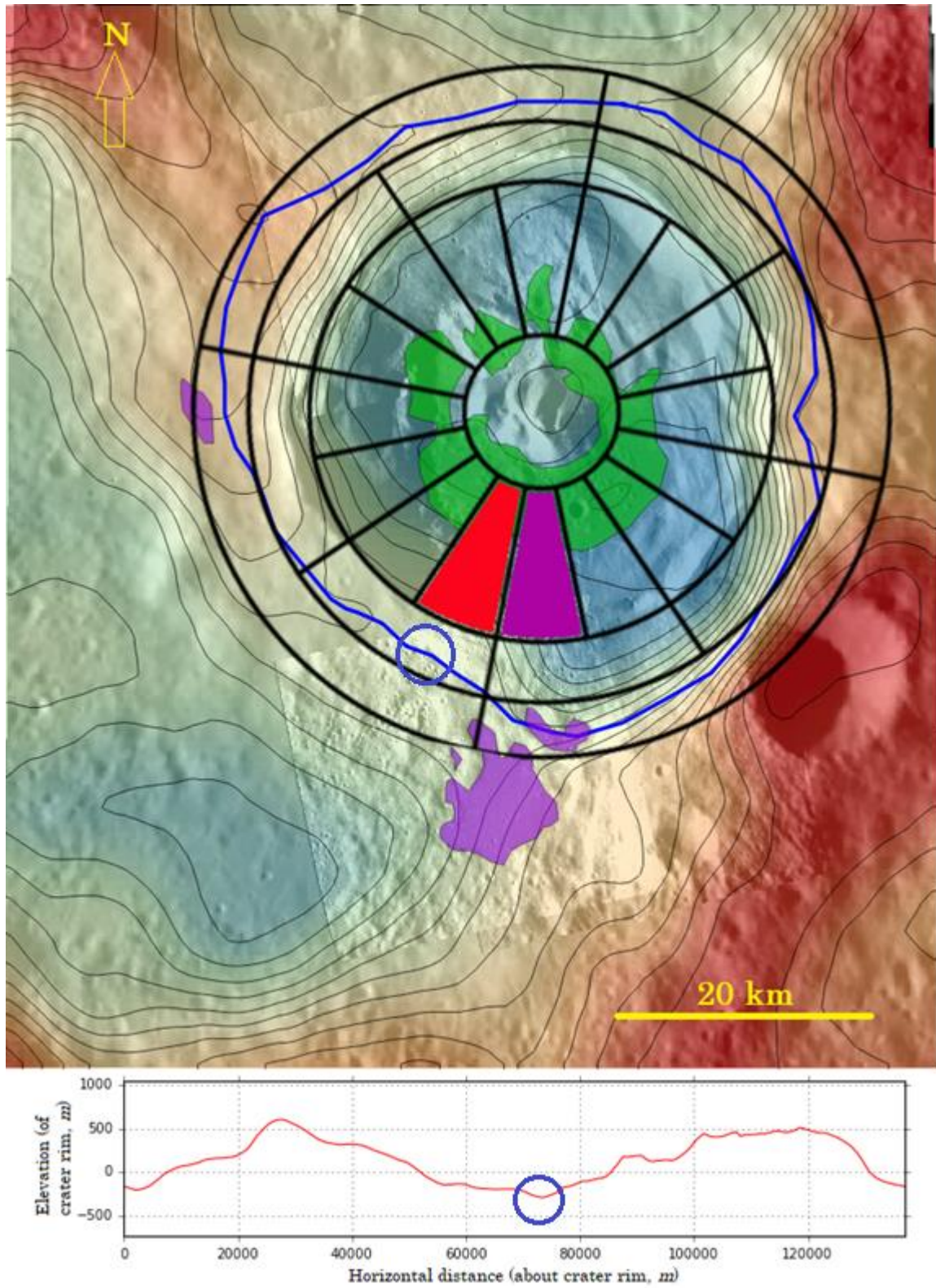
Kulthum crater:



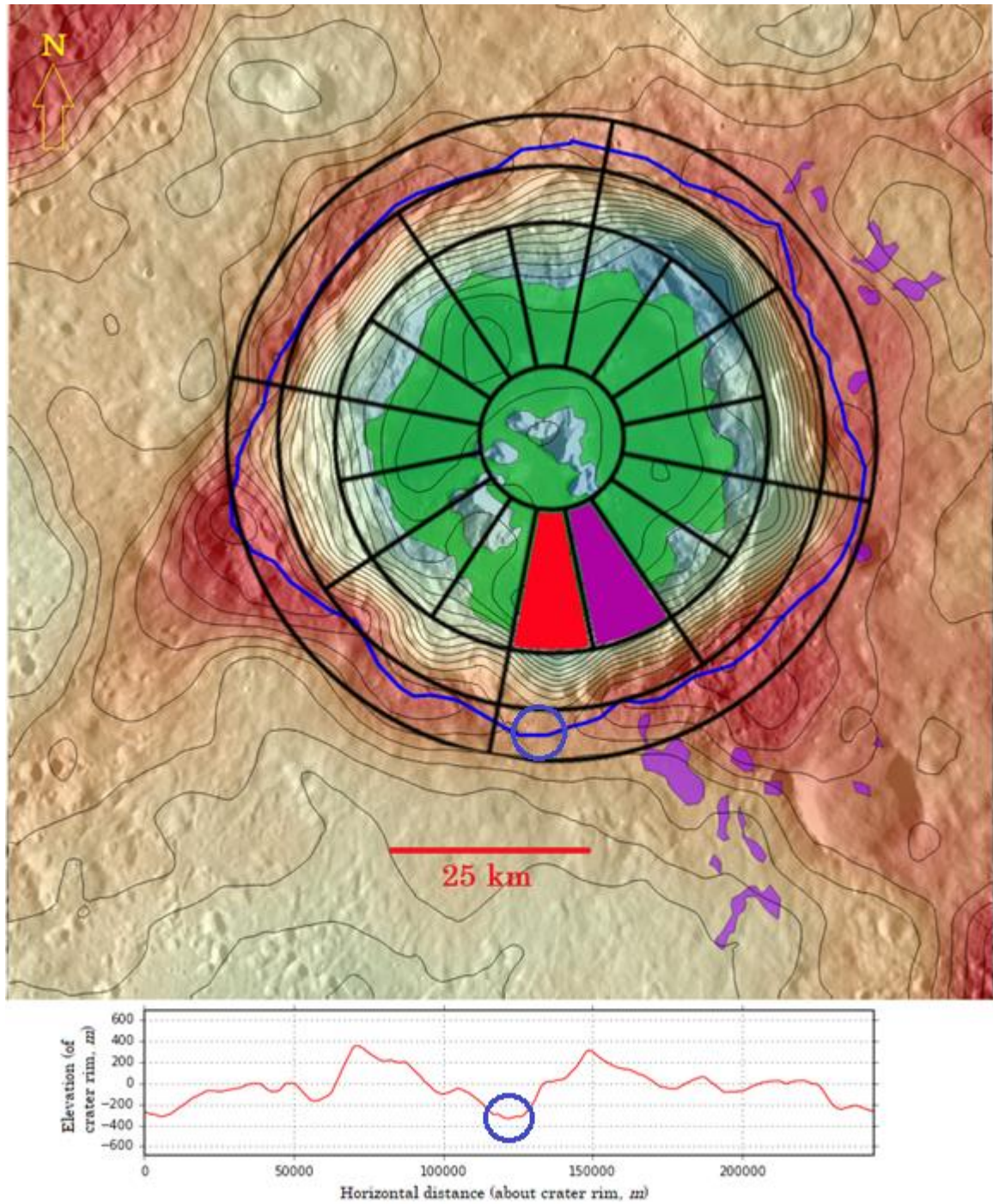
Kyosai crater:



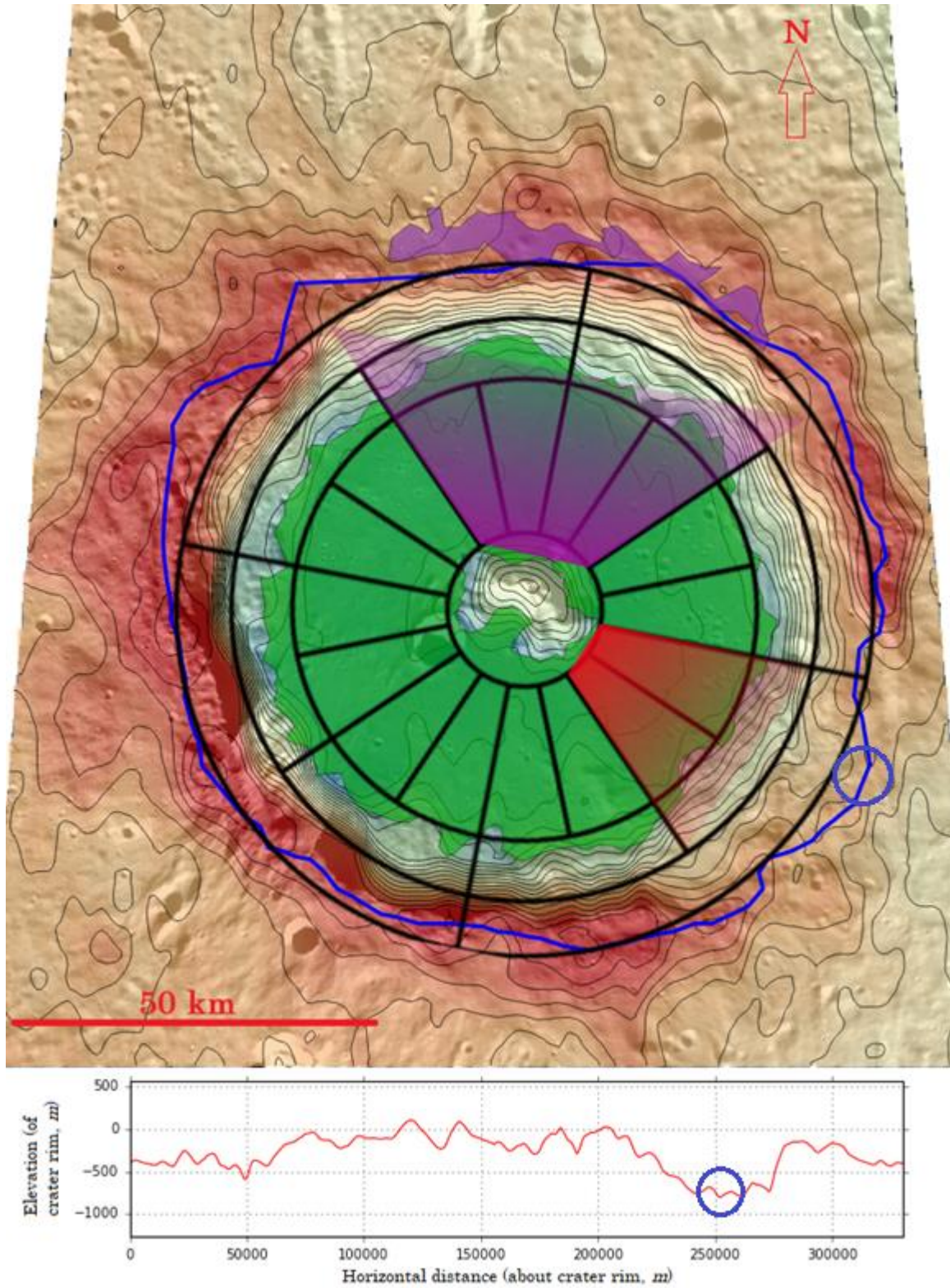
Plath crater:



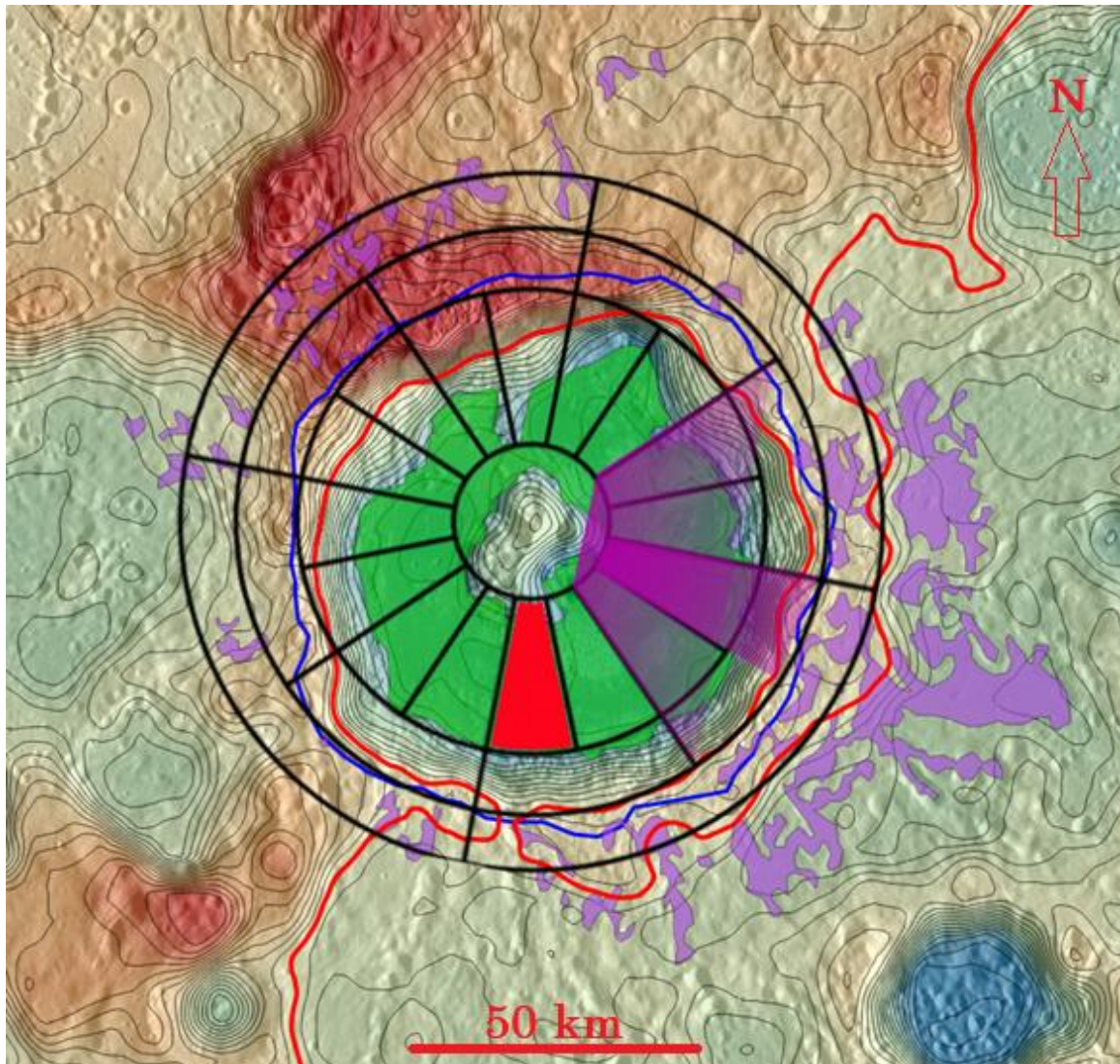
Seuss crater:



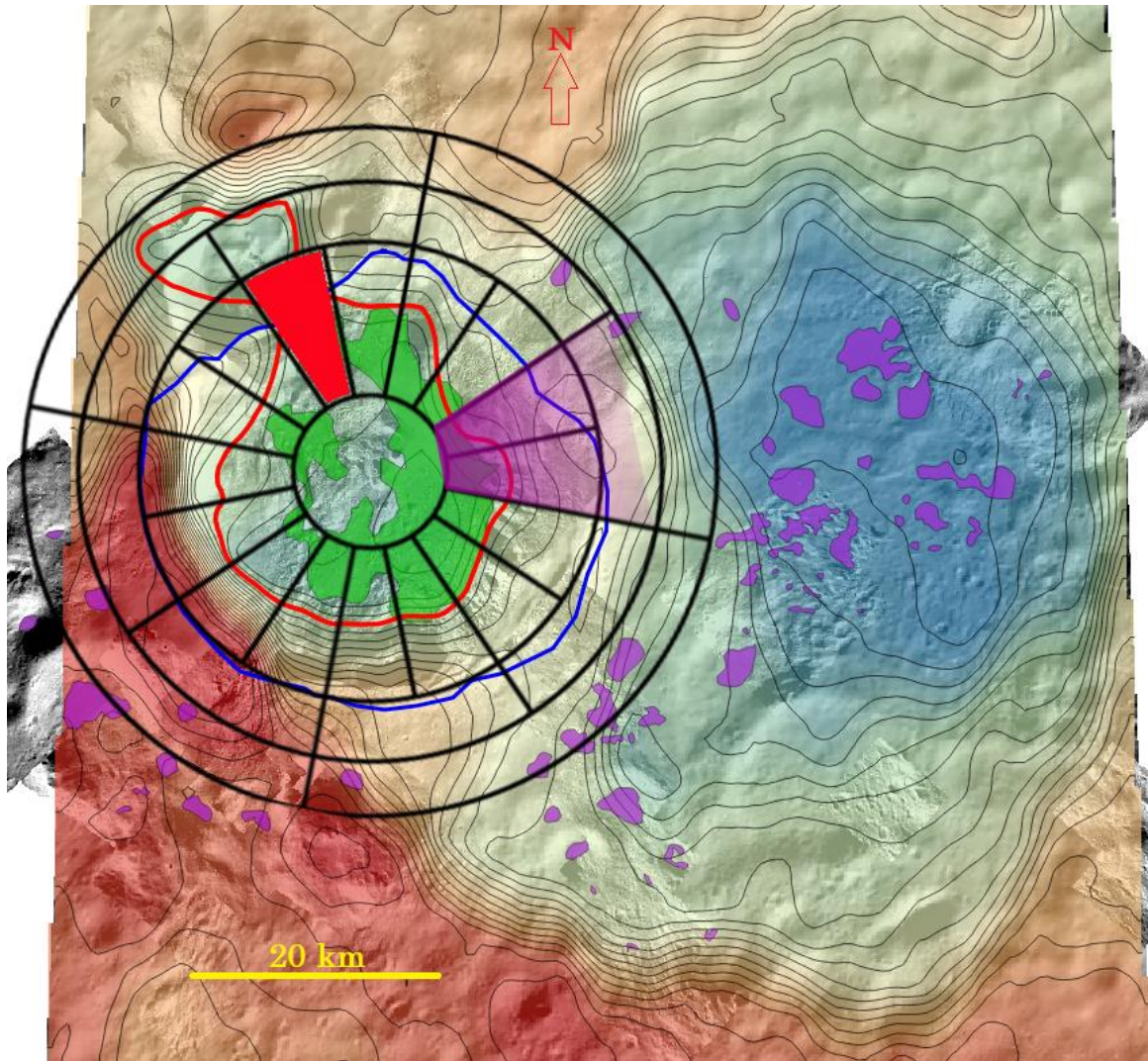
Stieglitz crater:



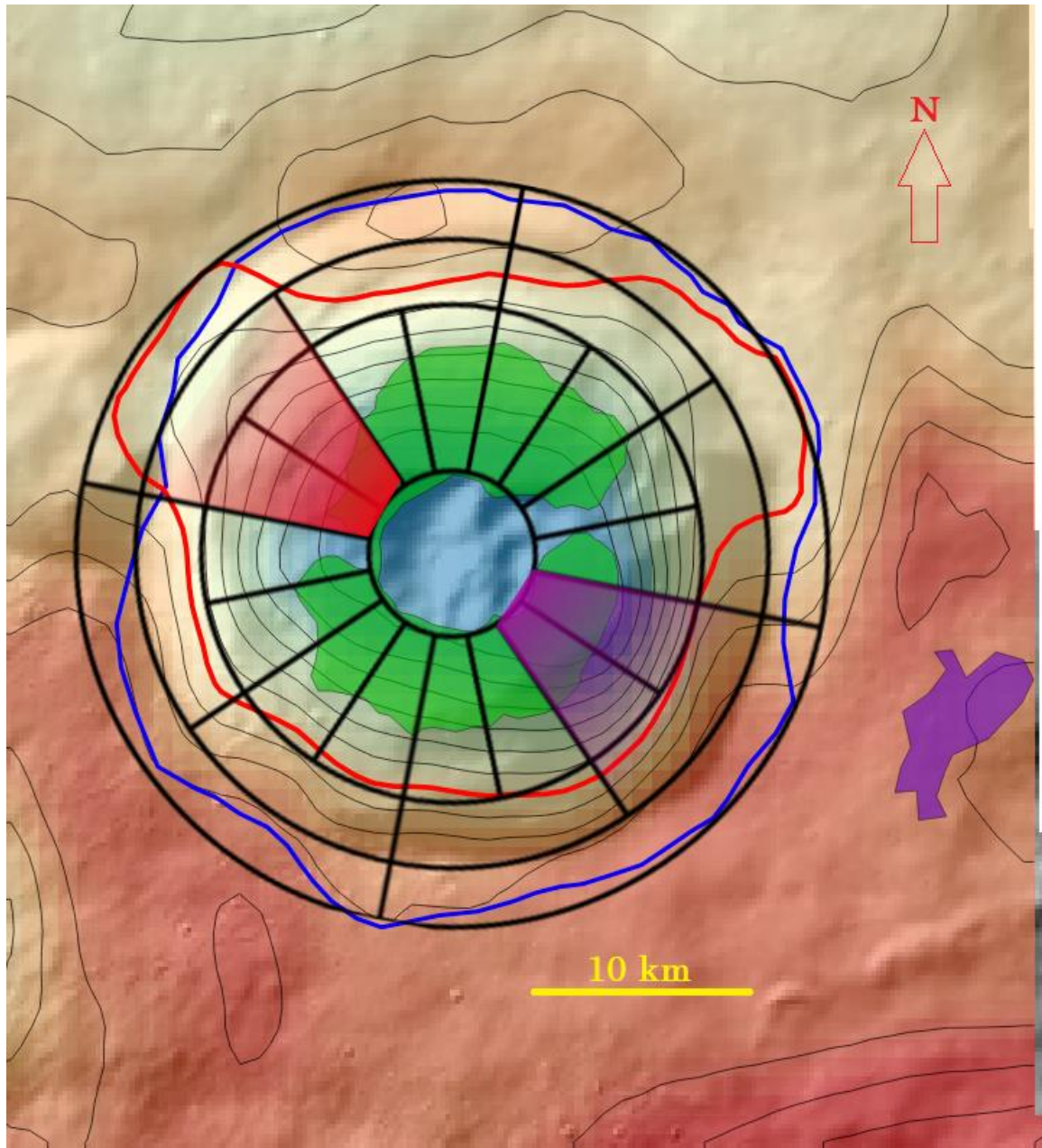
Tyagaraja crater:



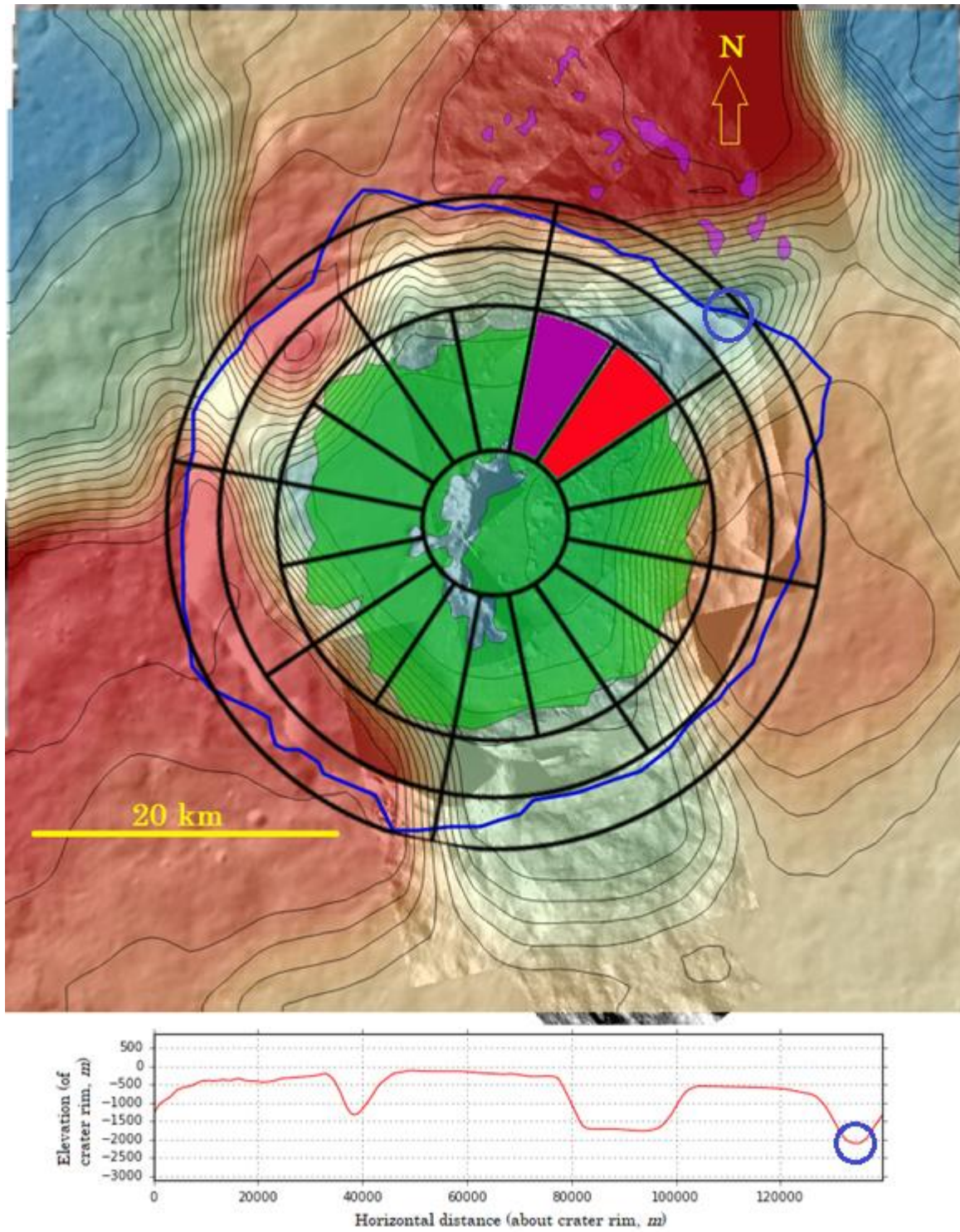
“Thomson” crater:



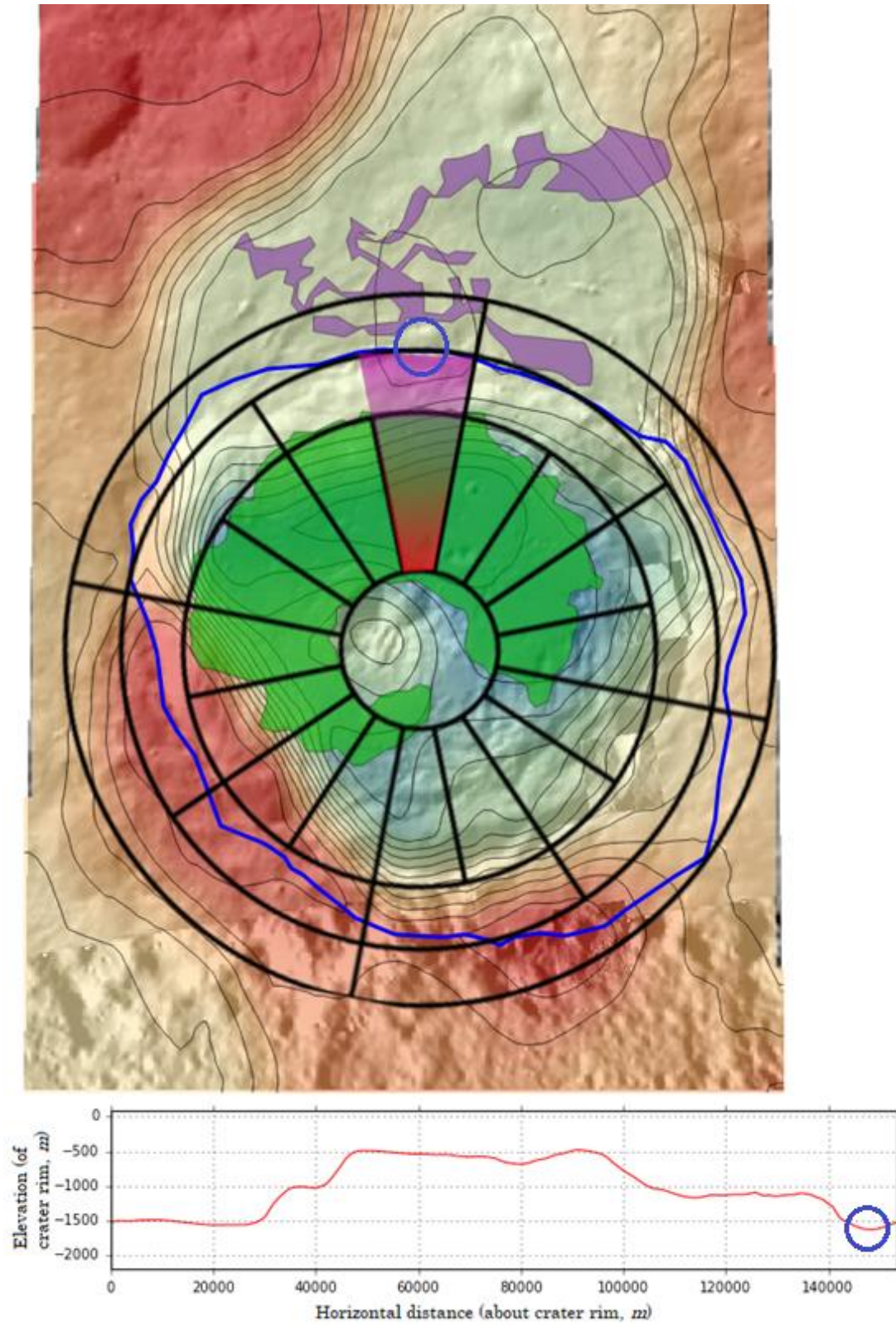
“Carr” crater:



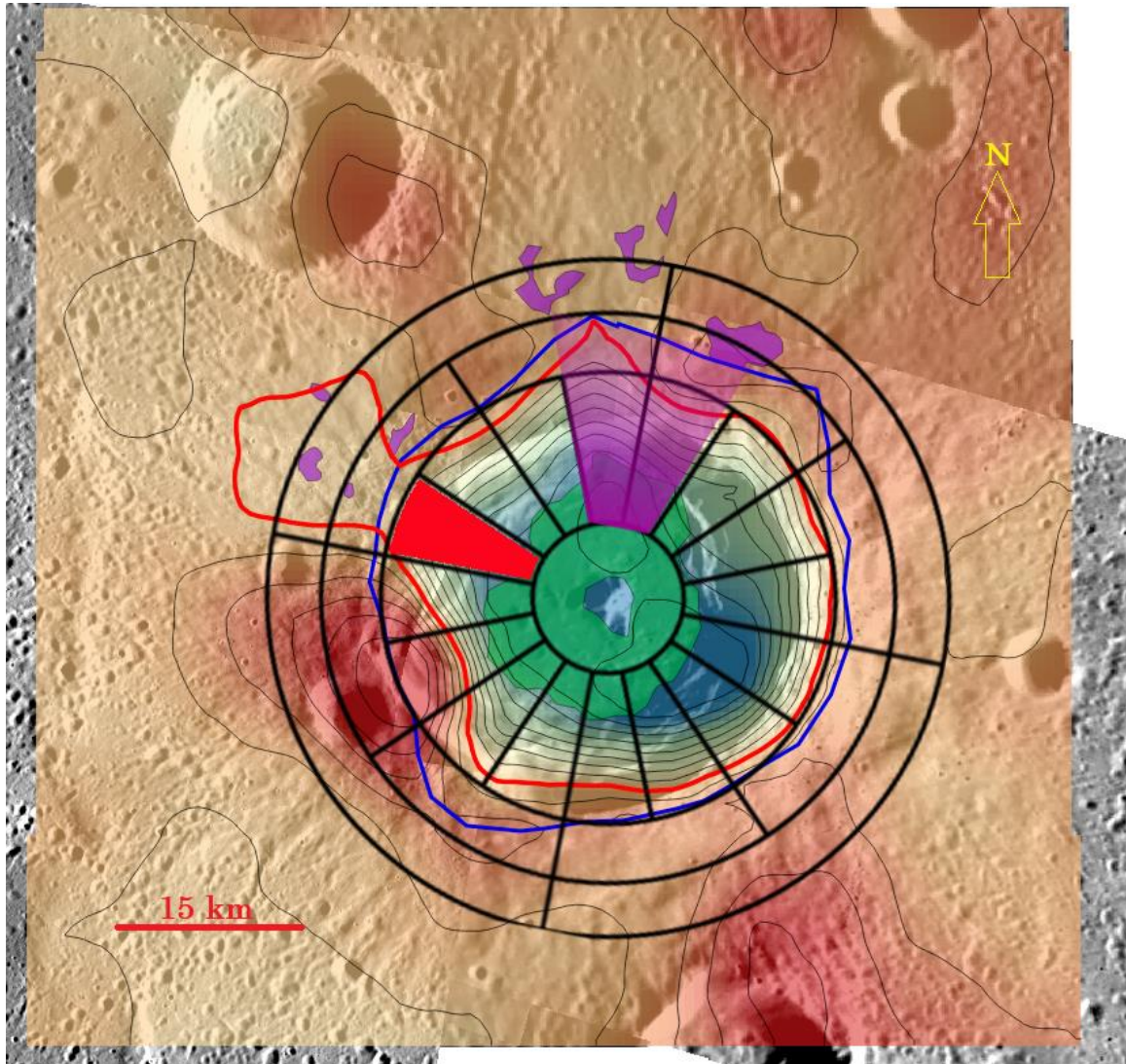
“Lightfoot” crater:



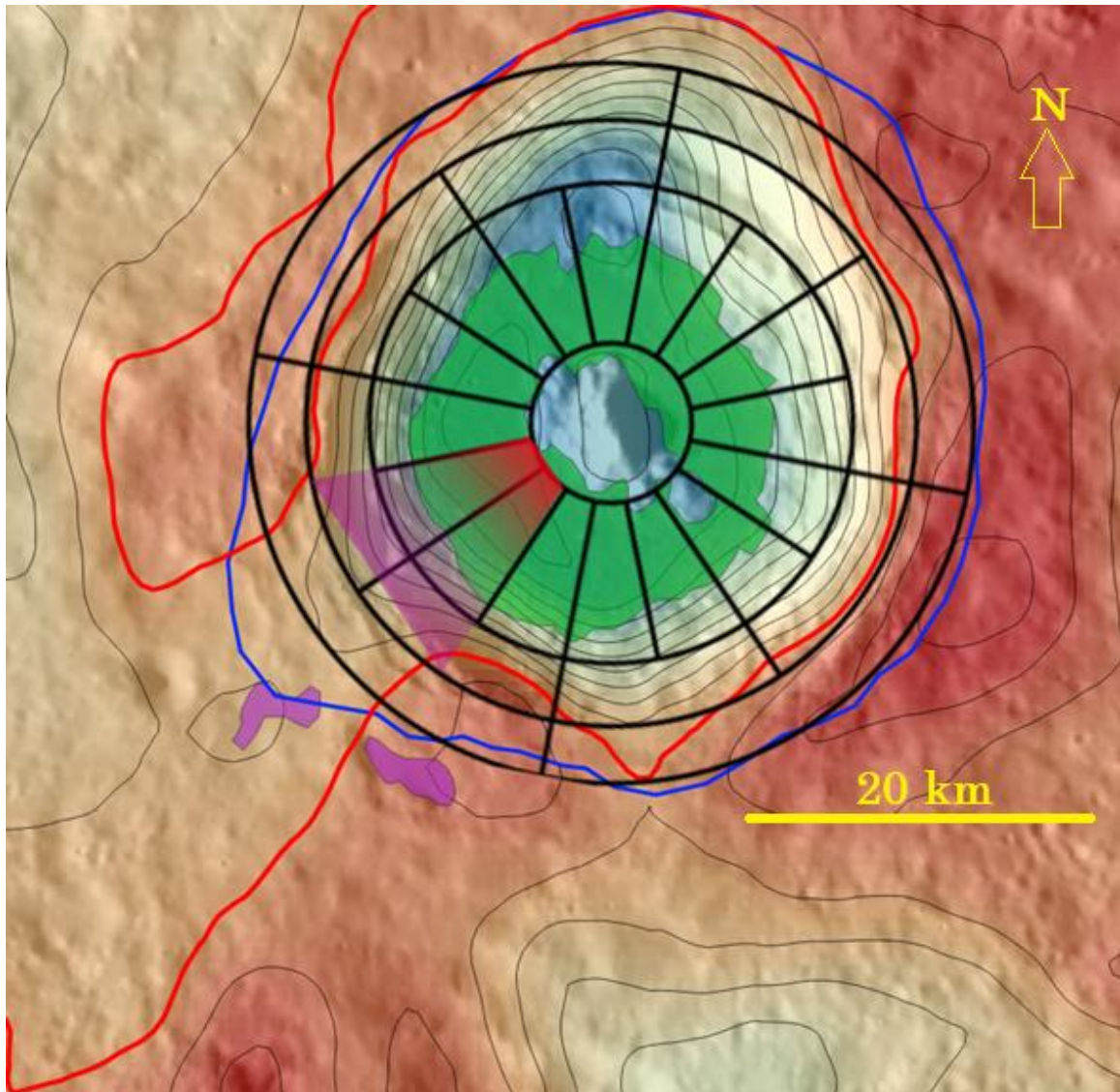
“Dorion” crater:



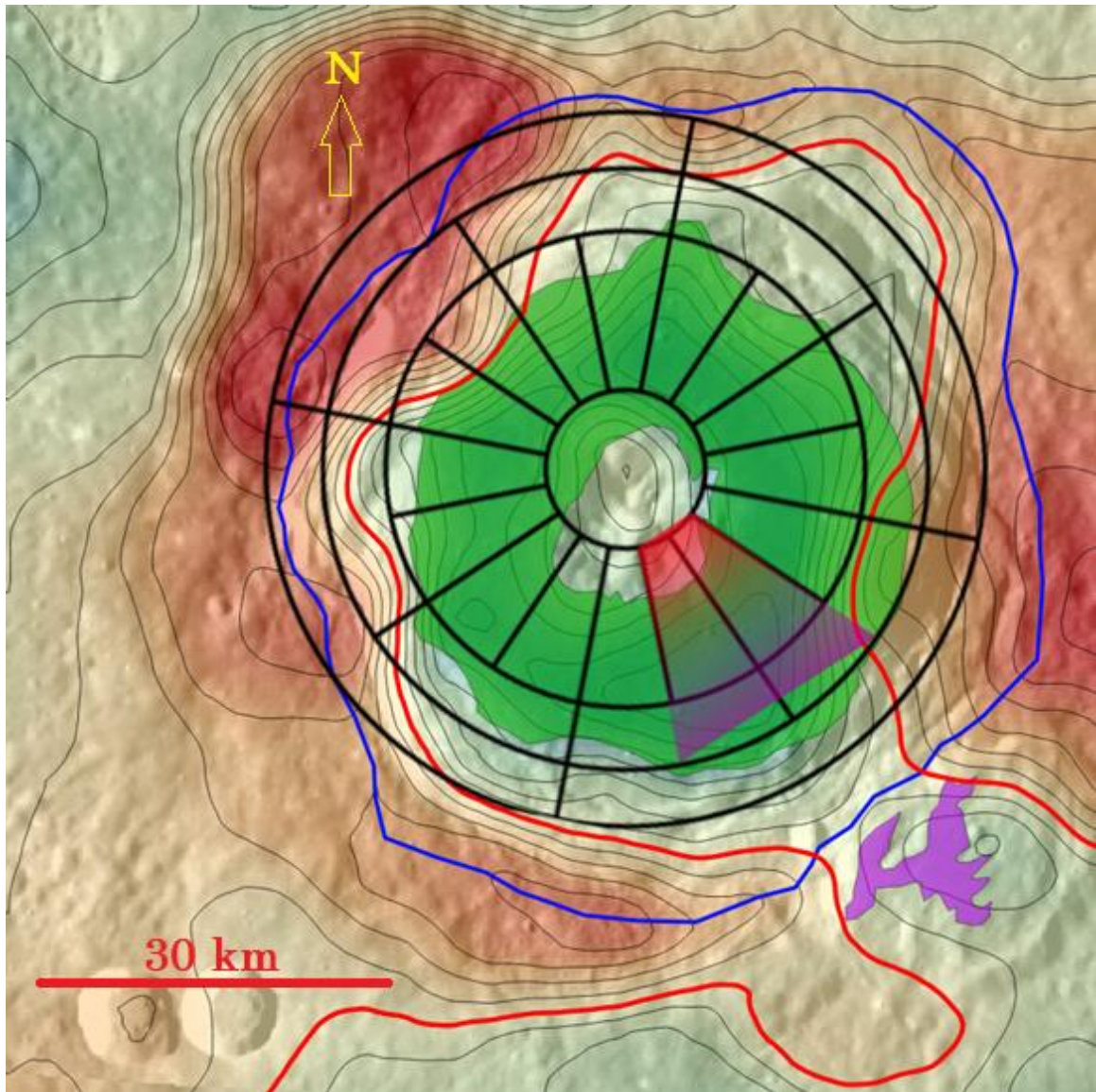
“Phidias” crater:



‘Hemon’ crater:



‘Bennington’ crater:



Appendix B: EDRNAC images used in individual crater files

Ailey crater: EN0213154766M, EN0233052079M, EN0263440024M.

Apollodorus crater: EN0213414972M, EN0213415021M, EN1014849517M, EN1014849525M, EN1014993502M.

Balanchine crater: EN0213284943M, EN0213284979M.

Bek crater: EN0238697065M, EN0238697075M, EN0238697086M.

Cunningham crater: EN0250767656M, EN0250767665M, EN0250767674M.

Degas crater: EN0232203127M, EN0232203140M, EN0232203160M, EN0232203192M, EN0242338160M, EN0242338192M.

Erte crater: EN1008771355M, EN1008771379M, EN1008886680M, EN1024009665M, EN1024067288M.

Fonteyn crater: EN0236702535M, EN0236702547M, EN1013608910M.

Kulthum crater: EN0236617387M, EN0236617396M, EN0236617399M, EN0251833041M.

Kyosai crater: EN0220416139M, EN0220675454M, EN0250852067M.

Plath crater: EN0258602252M, EN0258602260M, EN0258602268M, EN0258631059M, EN0258631075M.

Seuss crater: EN0219901822M, EN0219901943M, EN0234960318M, EN0234960370M, EN0234960372M.

“Thomson” crater: EN0229105028M, EN0229105030M, EN0229105032M, EN0229105034M, EN0229105036M, EN0229105038M, EN0229105040M, EN0229105042M, EN0229105044M, EN0242171623M, EN0242213404M, EN0242213417M, EN0242255180M, EN0242255184M, EN0242255188M, EN0242255196M, EN0242296976M, EN0242296990M, EN0242338770M, EN0244170897M, EN0244170901M, EN0244170905M, EN0244257362M, EN0244257364M, EN0244286143M, EN0244286148M, EN0244286154M, EN0244286162M, EN0244286169M, EN0244430203M, EN0244430205M, EN0244430219M, EN0244430221M, EN0244430223M, EN1036770128M, EN1036770130M, EN1036770132M, EN1036770134M, EN1036770136M, EN1036770138M, EN1036770140M, EN1036770142M, EN1036770144M, EN1036770146M, EN1036770148M, EN1036770150M, EN1036770152M.

“Lightfoot” crater: EN0229364477M, EN0229364480M, EN0229364483M, EN0229364486M, EN0229364489M, EN0229364492M, EN0229364495M, EN0229364498M, EN0232033608M, EN0232033618M, EN0232033628M.

“Dorion” crater: EN1056841099M, EN1056841103M, EN1056841107M, EN1056841111M, EN1056841115M.

“Phidias” crater: EN0220675738M, EN0220675740M, EN1015078101M, EN1015078113M, EN1015078125M.

Curriculum Vitae

Name: Jeffrey Daniels

Post-secondary Education and Degrees: Lakehead University
Thunder Bay, Ontario, Canada
2008-2012 B.Sc.

Lakehead University
Thunder Bay, Ontario, Canada
2012-2016 B.Sc. (Honours)

The University of Western Ontario
London, Ontario, Canada
2016-2018 M.Sc.

Related Work Experience: Teaching Assistant
The University of Western Ontario
2016-2018